Direct Observation of Charge-Carrier Separation in Locally Illuminated Semiconductors

DISSERTATION

for the attainment of the degree

doctor rerum naturalium

(Dr. rer. nat.)

submitted by

Moritz Anton Wehrmeister

Fakultät für Mathematik, Informatik und Naturwissenschaften

Institut für Physikalische Chemie

Universität Hamburg

Hamburg, August 2025

Gutachter der Dissertation: PD Dr. Tobias Kipp
PD Dr. Tobias Vossmeyer

Gutachter der Disputation: PD Dr. Tobias Kipp
Prof. Dr. Carmen Herrmann
Dr. Charlotte Ruhmlieb

Datum der Disputation: 17.10.2025

Datum der Druckfreigabe: 05.11.2025

Abstract

Nanostructured optoelectronic components are integral to many emerging technologies. The functionalities of these components often rely on the separation and transport of optically excited charge carriers within semiconductor materials. Gaining a comprehensive understanding of the internal charge-carrier dynamics and the underlying electric fields is necessary for the ongoing development of these devices. To that end, characterization methods need to be developed that are able to uncover these properties.

In this work, electrical and surface-potential measurements with optical excitation were performed simultaneously, by developing and integrating a scanning photocurrent microscopy setup with a heterodyne Kelvin probe force microscopy system. This approach enabled spatially resolved insights into charge-carrier separation and transport processes in various semiconductor devices. A primary focus was placed on a cadmium sulfide nanowire device with ohmic contacts, investigating the impact the of mobility-induced charge-carrier separation and the resulting internal electric fields on the device's optoelectronic properties. A dynamic equilibrium between the electric fields and the charge-carrier distributions was found, which showed that in order to gain quantitative insights, simulations of the system need to be performed. These simulations provided key parameters such as the charge-carrier mobilities and lifetimes. Additionally, Schottky and diode cadmium sulfide nanowire devices were studied as well, to investigate the effects of different metal-semiconductor contact types on the charge-carrier dynamics.

Besides the investigation of nanowires, experiments on tin chalcogenide nanosheets, were performed as well. Different solutions to mitigate the spontaneous charging of uncontacted nanosheets were tested, involving fast discharging on a conductive substrate and post-processing. This enabled preliminary investigations, through which charge-carrier separation under illumination between tin selenide and gold nanoparticles, and between tin selenide and tin sulfide could be found. Scanning photocurrent microscopy and Kelvin probe force microscopy measurements were performed on a contacted tin selenide nanosheet with a tin sulfide frame, to map the spatially resolved short-circuit current and to determine the material's conductivity.

The investigations highlighted the fundamental differences between devices with different metal-semiconductor contact types and showed the complex interplay between internal and external electric fields as well as the internal structure of nanoscopic semiconductor devices. The results presented here show that the incorporated characterization methods provide a powerful toolset for investigating these devices with regard to charge-carrier dynamics and their underlying driving forces.

Kurzfassung

Nanostrukturierte optoelektronische Bauelemente sind integrale Bestandteile vieler Zukunftstechnologien. Ihre Funktionsweise beruht häufig auf der Trennung und dem Transport angeregter Ladungsträger in Halbleitern. Für die Weiterentwicklung solcher Technologien ist ein umfassendes Verständnis über die internen Ladungsträgerdynamiken und die zugrundeliegenden elektrischen Felder erforderlich. Hierfür werden Charakterisierungstechniken benötigt, die diese Eigenschaften aufklären können.

In dieser Arbeit wurden elektrische Messungen und Oberflächenpotentialmessungen gemeinsam mit optischer Anregung gleichzeitig durchgeführt, indem Rasterphotostrommikroskopie und Rasterkelvinsondenmikroskopie kombiniert wurden. Dadurch konnten Ladungsträgertrennung und Transportprozesse in Halbleiterbauelementen ortsaufgelöst untersucht werden. Ein Schwerpunkt lag dabei auf einem Cadmiumsulfid-Nanodraht mit ohmschen Kontakten. Hier wurde der Einfluss der mobilitätsinduzierten Ladungsträgertrennung und dem daraus resultierenden internen elektrischen Feld auf die optoelektronischen Eigenschaften untersucht. Es wurde ein dynamisches Gleichgewicht zwischen den elektrischen Feldern und der Ladungsträgerverteilung festgestellt. Daraus wurde geschlossen, dass Simulationen des Systems notwendig sind, um die Eigenschaften des Halbleiters quantitativ zu bestimmen. Anhand der Simulationen konnten Schlüsselparameter wie die Ladungsträgermobilität und die Lebenszeit bestimmt werden. Zusätzlich wurden Schottky- und Diodenbauelemente mit Cadmiumsulfid-Nanodrähten untersucht um den Einfluss der unterschiedlichen Kontaktarten auf die Ladungsträgerdynamiken zu bestimmen.

Neben Nanodrähten wurden außerdem Experimente an Zinnchalcogenid-Nanoblättern durchgeführt. Verschiedene Ansätze zur Vermeidung der spontanen Aufladung von unkontaktierten Nanoblättern wurden getestet, darunter das schnelle Entladen auf leitfähigen Substraten und nachträglicher rechnerischer Fehlerkorrektur. Dadurch konnten vorläufige Experimente durchgeführt werden, die die Trennung optisch angeregter Ladungsträger zwischen Zinnselenid und Zinnsulfid, sowie zwischen Zinnselenid und Goldnanopartikeln zeigten. Rasterphotostrommikroskopie und Rasterkelvinsondenmikroskopie wurden an einem kontaktieren Zinnselenid-Nanoblatt mit einem Zinnsulfid-Rahmen durchgeführt. Dadurch konnten der Kurzschluss-Photostrom ortsaufgelöst gemessen werden und die Leitfähigkeit des Materials bestimmt werden.

Die Untersuchungen zeigten die wesentlichen Unterschiede zwischen den verschiedenen Metall-Halbleiter-Kontaktarten sowie die komplexen Wechselwirkungen zwischen internen und externen elektrischen Feldern und der internen Struktur der nanoskopischen Halbleiterbauelemente auf. Die Ergebnisse dieser Arbeit zeigen, dass die eingesetzten Charak-

terisierungsmethoden geeignet sind, nanostrukturierte Bauelemente hinsichtlich ihrer Ladungsträgerdynamiken und der zugrundeliegenden Kräfte detailliert zu untersuchen.

Contents

List of Abbreviations

AC	alternating current
AFM	atomic force microscopy
AFS	atomic force spectroscopy
AM	amplitude-modulation
APD	avalanche photodiode
AuNP	gold nanoparticle
BP	band-pass
CuS	copper sulfide
CdS	cadmium sulfide
CdSe	cadmium selenide
CPD	contact potential difference
DC	direct current
EFM	electrostatic force microscopy
EHC	excess hole concentration
FM	frequency-modulation
H	heterodyne
I_{SC}	short-circuit current
ITO	indium tin oxide
IV	current-voltage
KPFM	Kelvin probe force microscopy
LA	laser-aligned
LCAO	linear combination of atomic orbitals
LED	light-emitting diode

LI locally-illuminated

LL laser-line

LP long-pass

ND neutral-density

ML monolayer

PECVD plasma-enhanced chemical vapor deposition

PID proportional-integral-derivative

PL photoluminescence

PLL phase-locked loop

PM power meter

PtIr platinum iridium

QI quantitative imaging

SCR space-charge region

SiO_2 silicon dioxide

SNOM scanning near-field optical microscopy

SnS tin sulfide

SnSe tin selenide

SPCM scanning photocurrent microscopy

SPM scanning probe microscopy

TAO tip-assisted optics

V_{OC} open-circuit voltage

List of Figures

List of Tables

1 Introduction and Project Aim

A common trend in the development of new electronic technologies is the miniaturization of individual components. Among such components are transistors,[1] solar cells,[2] light-emitting diodes (LEDs)[3] or photodetectors,[4] which benefit from their smaller scale, among other things, by increased efficiency, easier integration and new functionalities. Improvements in the manufacturing processes of these devices have allowed for the fabrication of key semiconductor components on the nanometer scale. At these scales, not only do the properties of the semiconductors begin to deviate from the bulk values, but also different structures like nanosheets,[5] or nanowires,[6] and different semiconductor materials like cadmium sulfide (CdS)[7] or tin selenide (SnSe),[8] can be considered to tune the devices' properties.

This technological evolution necessitates the development of characterization techniques at the nanoscale, like probe or laser scanning methods. Because many mechanisms, by which these nanoscaled devices operate, revolve around the movement of excited charge carriers (electrons and holes), the characterization methods should be sensitive to these as well.

Optical characterization methods often rely on the optical excitation of charge carriers in a semiconductor material. To that end, lasers can be used due to their sharp emission at specific wavelengths and high power densities at high resolutions. Both the absorption of the incident light, and the emitted photoluminescence (PL) can be analyzed to gain insights on the optoelectronic processes inside the respective material.[9]

In addition to optical characterization, in optoelectronic devices, like solar cells or detectors, the impact of incident light on the device's current-voltage (IV) characteristics can be studied by measuring the current under illumination (photocurrent). Some device geometries even allow for local illumination of different parts of the semiconductor, to give spatial information about regions of the device contributing to the photocurrent. To this end, the laser is scanned across the device, while for each position the resulting photocurrent is measured, which is called scanning photocurrent microscopy (SPCM).[5, 10]

While laser based methods rely on the interaction of the device or sample with electromagnetic radiation, scanning probe microscopy (SPM) methods use the interaction of the device with a sharp scanning tip (or probe) as the basis for measurements. A common technique is atomic force microscopy (AFM), where attractive and repulsive forces between the tip and the sample are measured, whereby this method can be used to measure the topography of the sample.[11]

AFM measurements are not limited to mechanical interactions, but can also be expanded to electrostatic forces arising between the tip and a sample, which is then called electrostatic force microscopy (EFM). The electrostatic forces between the tip and the sample are

measured only qualitatively by EFM. To improve upon this, Kelvin probe force microscopy (KPFM) was developed, where by continuously compensating the electrostatic forces, quantitative measurements were made possible.[12–14]
KPFM is able to show charge imbalances, which is especially useful, when analyzing semiconductors or optoelectronic devices under illumination. In doing so, inefficiencies of these devices can be uncovered *in operando*. In the past, this has usually been done, using global instead of local illumination, due to the experimental challenges associated with locally illuminating a sample while analyzing it with a scanning probe.[15–17]

Based on these techniques, this work aims to combine local illumination, and current measuring methods such as SPCM with KPFM in order to characterize optoelectronic semiconductor devices *in operando*. Thereby, new insights into the charge-carrier separation occurring in these locally illuminated devices are set to be gained, while also accessing key parameters of the involved semiconductor materials such as the charge-carrier mobilities and conductivities. Beyond this, the charge-carrier separation in metal-semiconductor hybrid structures and at semiconductor heterojunctions will be studied using KPFM under illumination.

2 Theory

This chapter will discuss the theory of charge-carrier separation in contacted semiconductors. The focus will be on the theoretical concepts necessary for the interpretation of SPCM and different types of KPFM measurements under illumination in terms of the separation of locally excited charge carriers.

2.1 Band Structure of Semiconductors

Semiconductors are solid, crystalline structures, as are metals and insulators. The atoms in these crystalline structures are arranged regularly across long distances. This influences their electronic structure. While for molecules the linear combination of atomic orbitals (LCAO) leads to molecular orbitals with discrete energy levels, in crystals with a theoretically infinite amount of atoms, the energy levels of these orbitals are so close to each other that they can be described as continuous bands. Diagrams of these bands are shown in figure 2.1.
In energy band diagrams, a few important variables are regularly pointed out. Among these are the Fermi level E_F and the vacuum level E_{Vac}. The energetic distance between the two is called the work function Φ. The highest band occupied by electrons at 0 K is called the valence band and the lowest unoccupied band is called the conduction band. The energy difference of their respective edges E_V and E_C is denoted as the band gap E_g.[18]

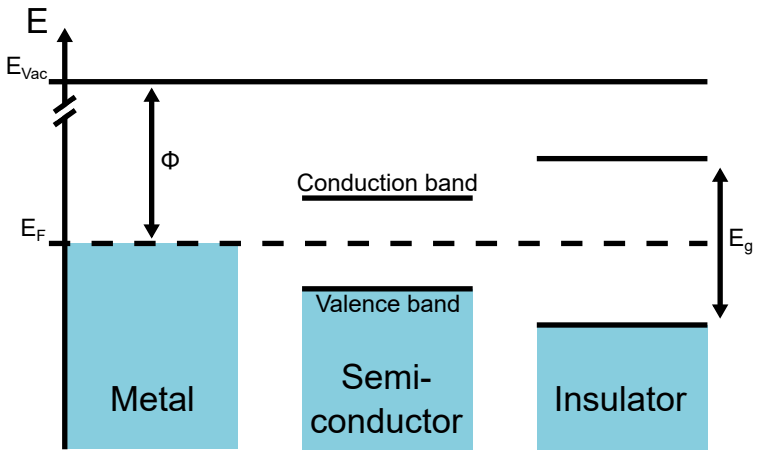

Figure 2.1: Exemplary band structures of metals, semiconductors and insulators. The valence band edges E_V and conduction band edges E_C are indicated by the solid lines for the semiconductor and the insulator.

The energetic distribution of the electrons in these band structures in equilibrium can be approximated by the Fermi-Dirac distribution

$$f(E) = \frac{1}{e^{(E-E_F)/k_B T} + 1}. \tag{2.1}$$

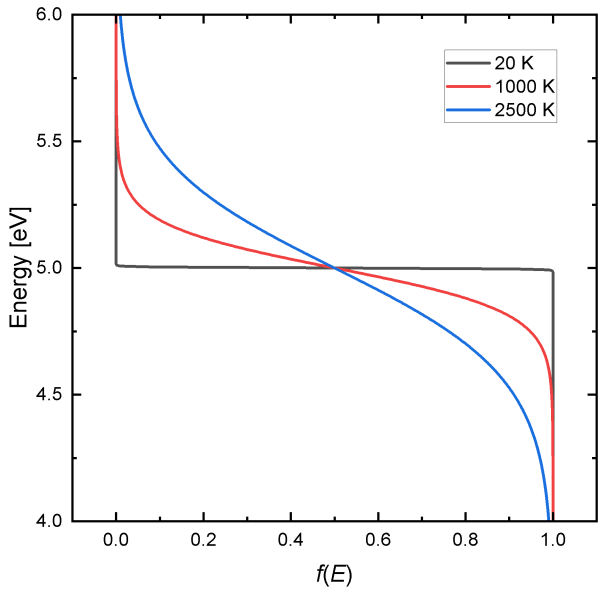

Figure 2.2: Fermi-Dirac distributions for 20 K, 1000 K and 2500 K. The Fermi level is at 5 eV.

Here, E is the energy of an electronic state, and f is the probability of an electron occupying this state, with k_B as the Boltzmann constant and the temperature T. In thermodynamic equilibrium, the Fermi level E_F is defined as the energy level, where the probability of occupation is 0.5. At 0 K, E_F is equal to the Fermi energy, which for metals denotes the highest occupied level at 0 K.[18]

From the Fermi-Dirac distributions in figure 2.2 it can be seen how with increasing temperatures, the occupation probability of energy levels above the Fermi level increases, while the occupation probability of lower energy levels decreases.

As shown in figure 2.1, for metals, the Fermi level is located energetically inside a band of molecular orbitals. In undoped semiconductors and insulators, it is located in the middle between the valence and conduction band. In accordance with the Fermi-Dirac distribution, thermally excited electrons can occupy states in the conduction band. Here, they can move through the material and contribute to the conductivity of the semiconductor. If the band gap E_g is larger than 5 eV, the material is considered an insulator.[18]

2.1.1 Doping

The absence, replacement or addition of atoms to the semiconductor crystal lattice can result in additional energy levels in the band gap, which is called doping. For example, when an atom is replaced by an acceptor atom, which has less valence electrons than the original atom, an acceptor level is created just above the valence band edge which can be filled with an electron from the valence band. This creates a hole in the valence band, which can move through the crystal, contributing to the conductivity, whereby the semiconductor is called p-type. If the material is doped with atoms which have more valence electrons, donor levels

are created below the conduction band edge. The additional electrons can occupy the conduction band and it is called an n-type semiconductor.[18]
The doping of semiconductors changes the position of the Fermi level inside the band gap, as the occupation probability changes with the amount and position of additional acceptor and donor levels. The Fermi level decreases towards the valence band edge for p-type doping, and increases towards the conduction band edge for n-type doping.
Intrinsic defects in semiconductor compound materials can also lead to doping, like in the II-VI semiconductor CdS. The valence band is formed by the 3p-orbitals of sulfur, while the conduction band is formed by the 5s-orbitals of cadmium. Therefore, if sulfur vacancies occur, less energy levels are available in the valence band to be occupied by electrons donated by the cadmium. These are now in the conduction band, thereby increasing the conductivity.[19]

2.2 Interfaces

When two different materials, like an n-type and p-type semiconductor, come into contact, an interface forms between the two, which exhibits distinct physical properties. This is especially relevant when charge-carrier transport is to be facilitated across the interface, whose properties may be exploited in practical device applications. In such semiconductor devices, not only the interface between the two semiconductors is important, but also the interfaces between the semiconductors and the metal electrodes through which biases are applied. These affect the device's physical properties as well and therefore need to be taken into account when such devices are designed.[20]

2.2.1 pn-Junctions

In equilibrium, the Fermi level must be constant in the entire device, even in a heterogeneous system. A driving force of the equilibration is the tendency of electrons to occupy states of the lowest possible energy. Therefore, when two different materials with different energy levels come into contact, electrons flow from one to the other in order to reach the lowest possible energy.[21] Figure 2.3 shows an exemplary energy diagram of the contact region between an n-type and p-type semiconductor in equilibrium.
The transfer of electrons from the n-type to the p-type material not only equalizes the Fermi levels, but also creates an internal electric field due to the formation of a space-charge region (SCR). This electric field is opposed to the flow of electrons, thereby preventing further exchange of charge carriers across the energy barrier in the SCR, which needs to be overcome for further charge-carrier transfer.[21]
Figure 2.4 shows the space charge, electric field, potential and energy of a pn-junction. Integration of the space charge yields the electric field, and integration of the electric field yields

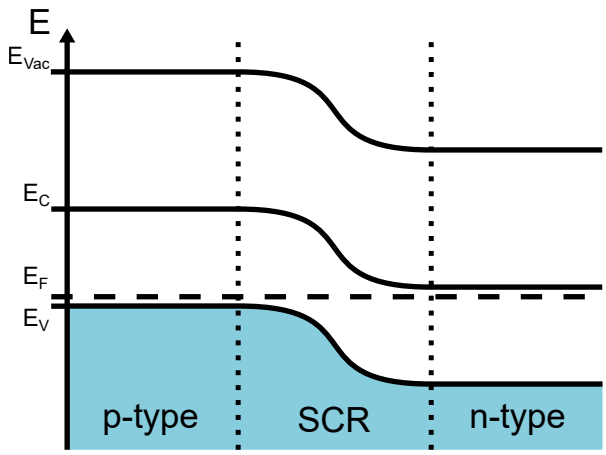

Figure 2.3: Band diagram of the interface between a p-type and n-type semiconductor with a space-charge region (SCR) in the middle.

the energy, which is the negative of the potential. By applying an external electric field to the system, the energy barrier can either be increased or decreased. For example, applying a positive bias to the p-type semiconductor increases its potential and lowers the energy barrier and is called a forward bias. As the space charges are reduced, the electric field in the SCR and the potential difference between the two materials are reduced as well. Conversely,

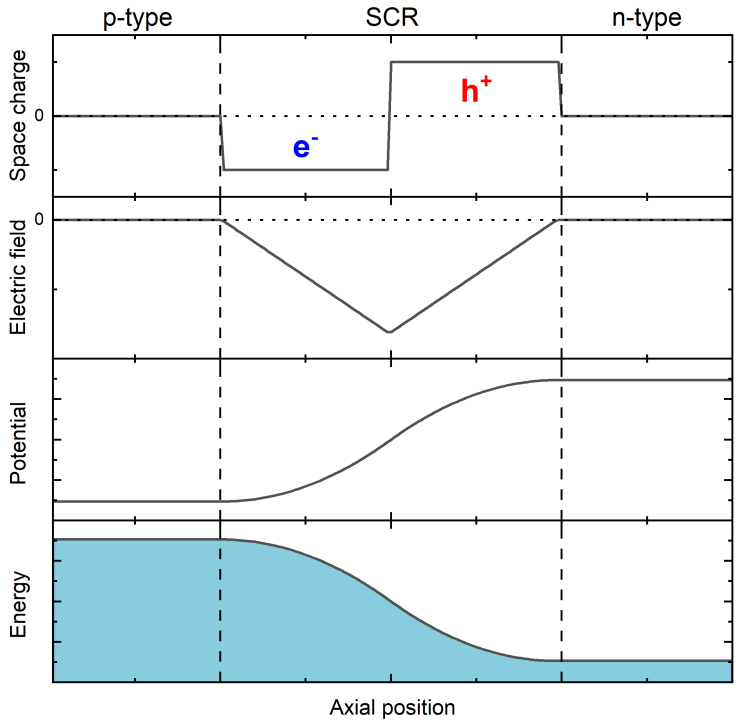

Figure 2.4: Space charge, electric field, potential and energy of a pn-junction. The SCR is bordered by the dashed lines. The p-type material is to the left and the n-type material is to the right of the SCR.

the application of a negative bias to the p-type semiconductor decreases its potential and increases the energy barrier and is called a reverse bias.[21]

2.2.2 Metal-Semiconductor Interfaces

Similar to pn-junctions, metal-semiconductor interfaces also experience Fermi-level equilibration upon contact. The nature of these contacts highly depends on the work functions of the metal and the semiconductor, so their respective differences between the Fermi level and the vacuum level. The work function of the semiconductor can be affected by its doping. For n-type semiconductors, the Fermi level is increased and thereby its work function is decreased, relative to the undoped material, while for p-type semiconductors the opposite is the case.[21] An exemplary band structure of n-type cadmium sulfide contacted on both sides by indium is shown in figure 2.5.

If the work function of the metal is lower than that of the semiconductor, as in figure 2.5, electrons in the conduction band do not exhibit a significant energy barrier when moving across the interface. This contact type is called an ohmic contact, where the charge transfer is largely dependent on the ohmic resistance of the components in the system, which leads to linear IV-curves described by Ohm's law, as shown in figure 2.6a.[21]

If the work function of the metal is higher than that of the semiconductor, as in figure 2.7, electrons are transferred from the semiconductor to the metal. This leads to an energy barrier, called a Schottky barrier, and a SCR similar to the pn-junction. In the case of an n-type semiconductor, contacted by a metal with a greater work function, the semiconductor is charged positively in the SCR, while electrons accumulate in a narrow region in the metal on the other side of the barrier. In p-type semiconductors, the majority charge-carriers are holes in the valence band, for which a Schottky barrier is formed with a metal with a lower work function.[21]

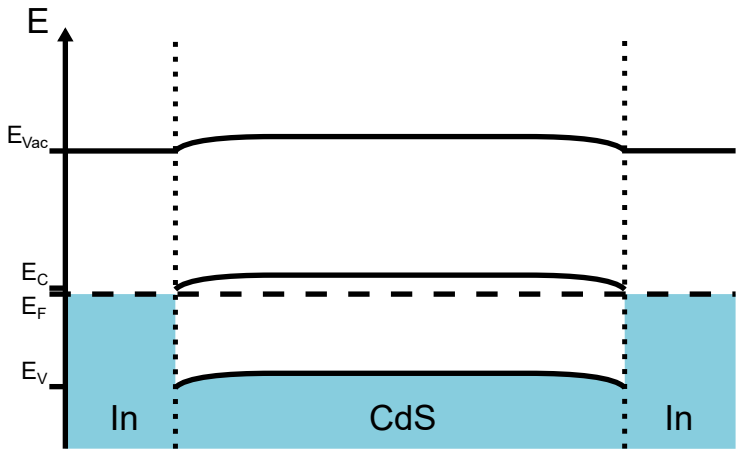

Figure 2.5: Band diagram of n-type cadmium sulfide contacted on two sides by indium.

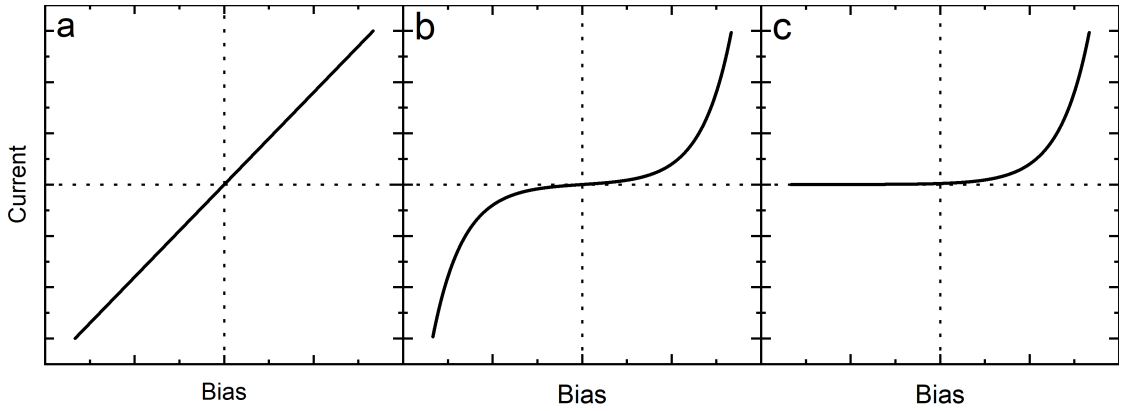

Figure 2.6: IV-curves of a) an ohmic device, b) a Schottky device and c) a diode device. The dashed lines represent the zero values of the respective axis.

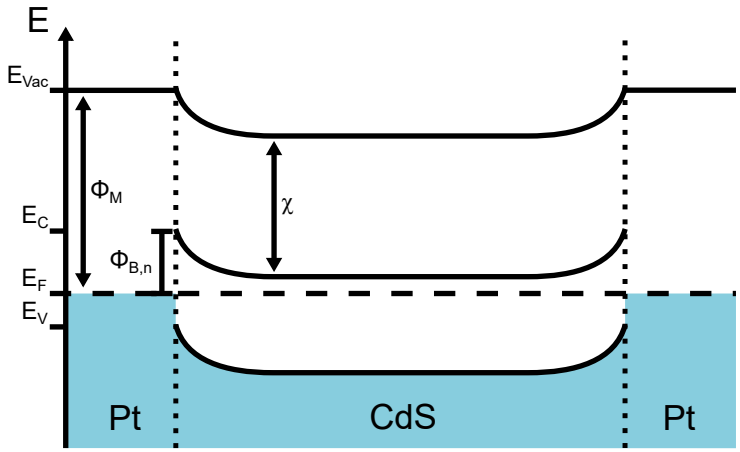

Figure 2.7: Band diagram of n-type cadmium sulfide contacted on two sides by platinum with the metal work function Φ_M, the semiconductor electron affinity χ and the resulting Schottky barrier height $\Phi_{B,n}$.

The height of the Schottky barrier $\Phi_{B,n}$ for an n-type semiconductor is given by

$$\Phi_{B,n} = \Phi_M - \chi, \tag{2.2}$$

where Φ_M is the metal work function and χ is the electron affinity of the semiconductor, which is defined as the difference between the vacuum level an the conduction band edge.[22]

A band diagram of a Schottky device is shown in figure 2.7. Here, the Schottky barriers impede the flow of electrons dependent on their direction. When one metal contact is biased negatively, electrons would have to overcome the barrier, in order to contribute to a current. In this case the barrier is considered to be biased in reverse, resulting in a low current. Larger currents are obtained, if the barrier is biased forward, with the electrons flowing from the semiconductor to the metal. When both the source and drain metal contacts induce a Schottky barrier, one of the two is always biased forward, leading to typical Schottky IV-curves for

both positive and negative applied biases, as shown in figure 2.6b. Since at the same time the other contact is always biased in reverse, the absolute current remains very low.[21]
Lastly, if a semiconductor has an ohmic contact to the source and a Schottky contact to the drain, or *vice versa*, diode like IV-curves can be measured, as shown in figure 2.6c. As the device is only biased in reverse for one current direction (here, negative biases) and forward biased for the other, the IV-curve shows asymmetric behavior, with much larger currents flowing for forward biases.[21] The accurate description of the current flow through and over the Schottky barrier is complicated. In general, two charge-carrier transport mechanisms can be discerned. These are the tunneling of electrons through the barrier (field emission), and the overcoming of the barrier by electrons with sufficient kinetic energy (thermionic emission). As a vast simplification, the relation of the current I and an applied bias V can be described by

$$I \propto \mathrm{e}^{\frac{qV}{k_\mathrm{B}T}}. \tag{2.3}$$

Here, q is the elemental charge, k_B is the Boltzmann constant and T is the temperature. This holds true, until the applied bias surpasses the barrier height, whereby the observed current becomes linear, and largely governed by the semiconductors properties.[23]

2.2.3 Charge-Carrier Separation

Charge carriers in semiconductors can be excited by the absorption of light. Upon absorption of a photon of sufficient energy, an electron is excited from the valence band into the conduction band, leaving behind a hole. This charge-carrier pair can contribute to a current if the charge-carriers are separated. In many devices this excitation and the subsequent separation of charge carriers are used to detect light or to transform radiation energy into electric energy in solar cells.[4, 6, 24]

Different processes can induce the separation of excited charge carriers, for example in the contact region of a pn-junction, which is shown in figure 2.8. When the charges are excited in the SCR of a pn-junction or a Schottky contact, they can be separated by the built-in electric field. In the band diagram of a junction this field is expressed by the slopes of the bands. Excited electrons follow the slope of the conduction band downwards to lower energies, as holes tend to higher energies in the valence band.[23]
In a device that is in integrated into an electric circuit, the excited and separated charge carriers can be collected by electrodes, and a current can be measured. This current is denoted as the short-circuit current (I_SC), as both electrodes are at the same bias. Charge-carrier separation can be improved by additionally applying a bias in the reverse direction of the pn-junction, as the electric field in the SCR is increased.[24] A resulting IV-curve is illustrated in figure 2.9.

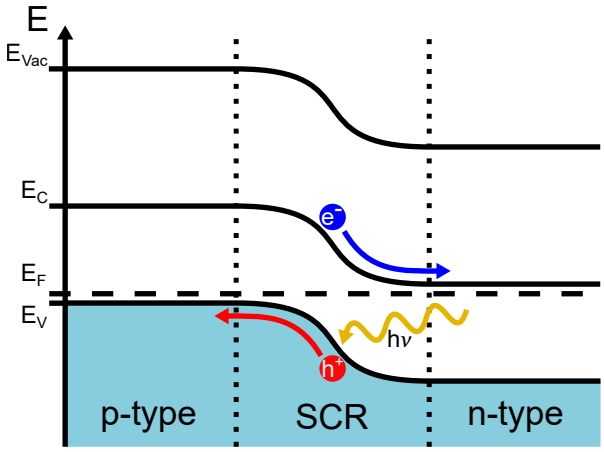

Figure 2.8: Band diagram of an illuminated pn-junction. The dashed lines represent the limits of the SCR, while the yellow waved arrow represents the incident light, and the blue and red arrows show the movement of the excited electrons and holes respectively.

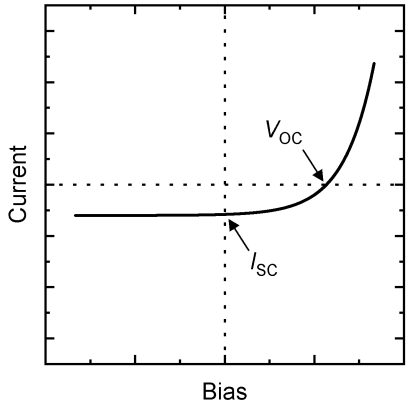

Figure 2.9: IV-curve of a diode device under illumination. The dashed lines represent the zero values of the respective axis.

The shape of the curve is comparable to that of the diode in figure 2.6c, though its shifted by the illumination. The y-intercept is no longer at zero, due to the aforementioned I_{SC}. Instead, in this case, a negative current is observed. For positive biases, the absolute current decreases as the electric field in the SCR is diminished. The bias at which no current is measured is called the open-circuit voltage (V_{OC}). At this point, the potentials of the p-type and n-type semiconductors are equalized, and the total electric field is zero, whereby no charge-carrier separation takes place. In solar cells, this charge-carrier separation at junctions is used to convert solar energy into electrical energy.[24]

Charge-carrier separation is not limited to electric field induced drift, but can also occur due to the diffusion of charge carriers, when they have different mobilities. According to Fick's first law, the diffusion flux J depends on the concentration gradient $\frac{\partial c}{\partial x}$ as

$$J = -D\frac{\partial c}{\partial x}. \tag{2.4}$$

Here, D is the diffusion coefficient. This coefficient is related to the mobility by the Einstein-Smoluchowski relation:

$$\mu = \frac{qD}{k_B T}, \tag{2.5}$$

where μ is the mobility, q is the elemental charge, k_B is the Boltzmann constant and T is the temperature.[18]

This shows that differing mobilities express themselves in a charge-carrier flux. Therefore, when charges are continuously excited and recombining, a dynamic equilibrium develops with uneven charge-carrier distributions. This was observed by Schäfer *et al.* in n-type cadmium selenide (CdSe) nanowires. Local illumination of the nanowire created an electric field inside the wire, which was observed using EFM. The charge-carrier distribution was modeled as shown in figure 2.10.[25]

The nanowire was charged positively at the point of illumination and negatively everywhere else. This was attributed to the different charge-carrier distributions which resulted from the different mobilities. Upon illumination, excited electrons distributed themselves across the whole nanowire, while the holes largely remained at the spot of illumination. This charge-carrier separation created a charge imbalance and therefore an electric field.[25]

2.3 Surfaces

When considering the surface of semiconductors, a lot of factors have to be taken into account. Not only intrinsic properties of the semiconductor crystal at the surface, such as dangling bonds, but also surface ligands, oxidation and the adsorption of molecules such as water or oxygen affect the properties of the semiconductor.[26–28]

The band structure at the surface can be considered in a similar way, as a metal-

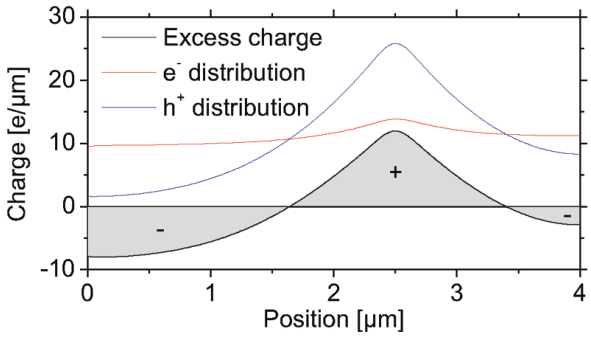

Figure 2.10: Modeled charge-carrier and excess charge distribution of a CdSe nanowire locally illuminated at 2.5 µm. For the electrons a higher mobility was assumed than for the holes. Adapted from Schäfer et al., with permission from the Authors, published in Nano Letters 2011.[25]

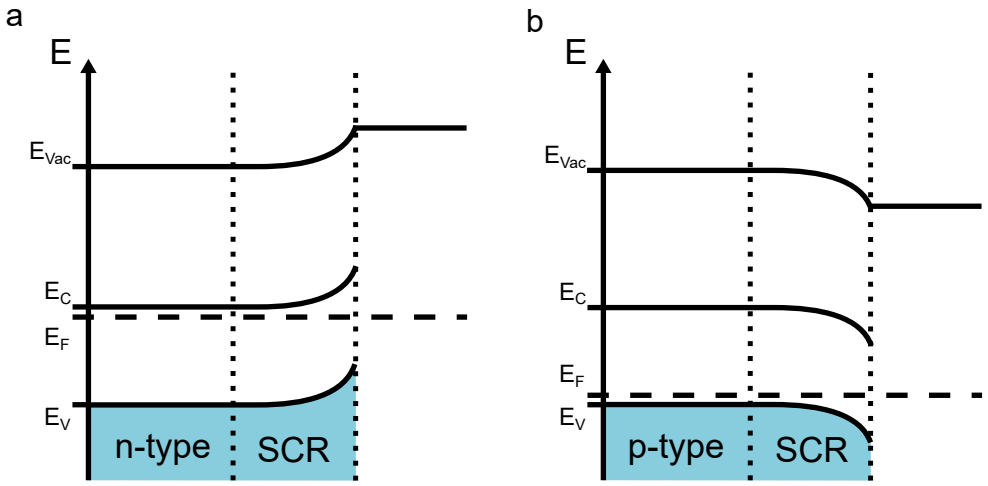

Figure 2.11: Band diagrams of a) an n-type and b) a p-type semiconductors SCR to the surface to the right.

semiconductor interface. Here, band bending in the semiconductor can take place as is shown in figure 2.11.

Depending on the doping of the semiconductor and the chemical potential of a surface layer, a SCR is formed. As a simplification, only the doping of the semiconductor is considered here, as the chemical potential of the surface layer is usually unknown. Thereby, n-type semiconductors can be expected to experience upward band bending at the surface, while p-type semiconductors experience downward band bending. This surface band bending not only affects any surface potential measurements, but also the movement of excited charge-carrier to and from the surface in the material.[29,30]

As mentioned before, the adsorption of molecules can have a profound impact on the effective work function at the surface. Caglar *et al.* studied the effect of different adsorbents on a Rhodium (100) surface. Their impact on the surface work function is shown in figure 2.12.[31]

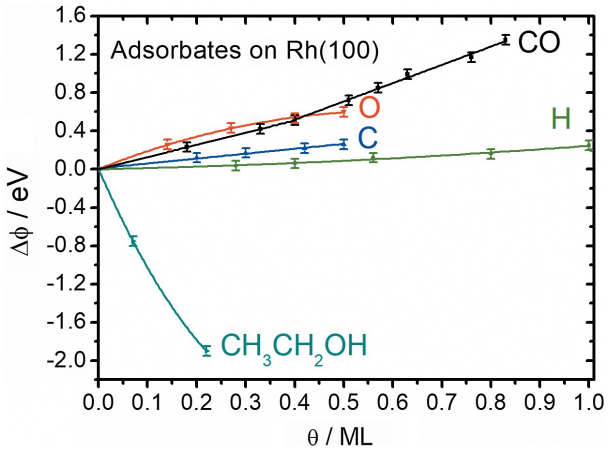

Figure 2.12: Deviation of the measured work function for different adsorbents at different occupancies. Reprinted from Caglar et al., licensed under CC BY 4.0.[31]

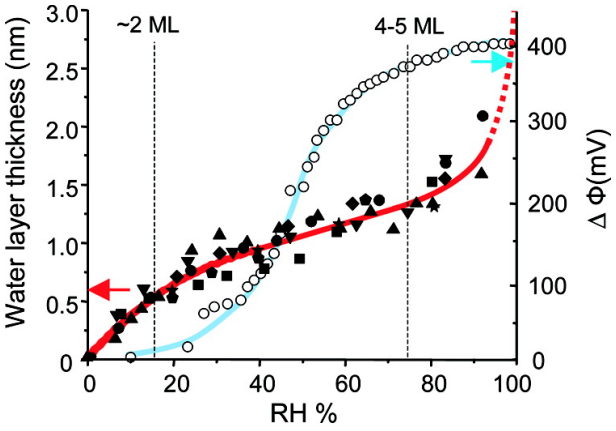

Figure 2.13: Water layer thickness on and measured work function deviation of a silicon dioxide (SiO_2) surface at different relative humidities. The relative humidities, where approximately 2 and 4-5 MLs of water molecules are adsorbed are indicated by dashed lines. Reprinted with permission from Verdaguer et al., Copyright 2007 American Chemical Society.[32]

In figure 2.12, the measured work function difference is correlated to the amount of monolayers (MLs) of five different molecules. Negative values indicate a decreased work function that correlates to an increased surface potential, and *vice versa* for positive values. It was found that when considering the relative surface work function, not only the chemical potential of the adsorbents is to be taken into account, but also their polarizability. Monoatomic adsorbents that extract electron density from the surface, such as oxygen, will skew surface-potential measurements to yield values for a more negative surface. This effect is stronger for more electronegative adsorbents. For larger molecules however, the polarity of the molecule itself has to be taken into account. For ethanol for example, the hydroxyl group will still extract electron density from the surface, like oxygen does. The outward facing alkyl chain however possesses a partial positive charge, which will mainly affect surface potential measurements.[31]

For surface-potential measurements in ambient conditions, water is a special adsorbent, which must be taken into account. Figure 2.13 shows results of experiments from Verdaguer *et al.*, where the thickness of a humidity-induced water film on a SiO_2 surface and the measured surface potential was correlated to the relative humidity. A decreasing number of MLs coincides with a decreasing change of the surface potential $\Delta\Phi$, which experiences a profound increase around 45 %RH. The effect of the humidity on the work function was attributed to the water dipoles orientation for different numbers of MLs. The impact of the first two MLs of water appears to be negligible, since on SiO_2 these are aligned to the surface dipoles. Starting with the 3rd ML, the water dipoles can rotate more freely, shielding the potential, or aligning themselves to external potentials, such as charged electrodes.[32,33] According to these findings, to ensure accurate surface potential measurements with $\Delta\Phi$ in the noise range of roughly 50 mV, the relative humidity should not surpass 30 %.

3 Methods

3.1 Atomic Force Microscopy

For the investigation of nanoscopic surfaces, a number of SPM techniques have been developed. One of these is AFM, where a sharp probe is used to measure forces, which arise from atomic interactions below 1 nN.

Figure 3.1 illustrates a typical setup of the detection scheme. Here, a sharp tip (diameter $\approx 5-25\,\text{nm}$) is located on a cantilever, which is able to bend, when the tip touches a surface. A laser beam is directed on the back of the cantilever and its reflection is directed onto a quadrant photodetector. When the cantilever is lowered onto a surface, the bending is transferred by the laser beam onto the detector, which measures the vertical and lateral deflection. In AFM, this vertical deflection can be used in a feedback loop with the z-axis of the cantilever, to maintain a constant height above the surface. In tapping mode, the cantilever is vibrated at its first eigenmode at a constant amplitude, which is used as the control parameter. When the cantilever is lowered onto the substrate, the repulsive forces between the tip and the sample decrease the vibration amplitude. By using a feedback loop a constant amplitude is maintained, which is often around 50-70 % of the free amplitude in air. Thereby the tip-sample distance is kept constant.[11]

When the tip is scanned across the sample the feedback loop can react to changes in the topography. When higher structures are encountered, the vibration amplitude decreases, and the tip height is automatically adjusted upwards, to ensure a constant distance. When these height differences are mapped out, a topography map of the sample is obtained. The lateral resolution is determined by the tip geometry. The height resolution depends on many factors, but can be in the range of a few Ångström.[11]

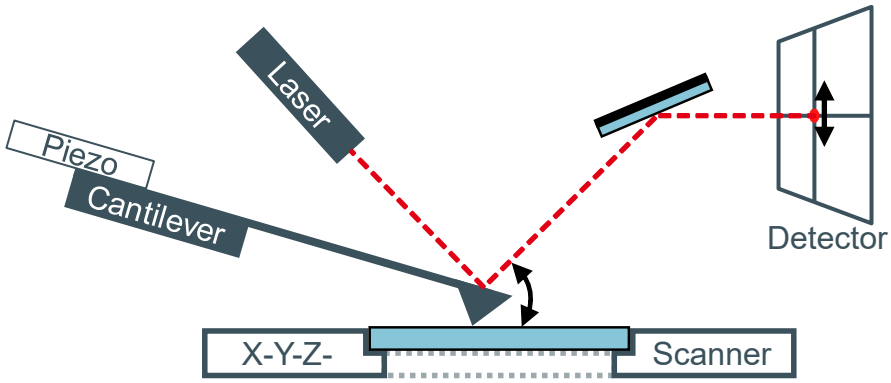

Figure 3.1: Sketch of an AFM setup. In this illustration the sample holder has an opening below the sample, to allow for additional measurements from below.

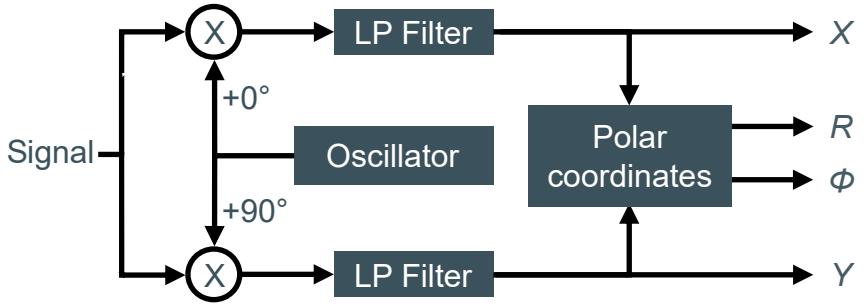

Figure 3.2: Signal path of a lock-in amplifier. The incoming signal is multiplied by a reference frequency twice at 90° phase difference. The results are passed through low-pass filters to obtain the X and Y components of the original signal at the reference frequency. These can be also converted to the amplitude R with the phase Φ.[34]

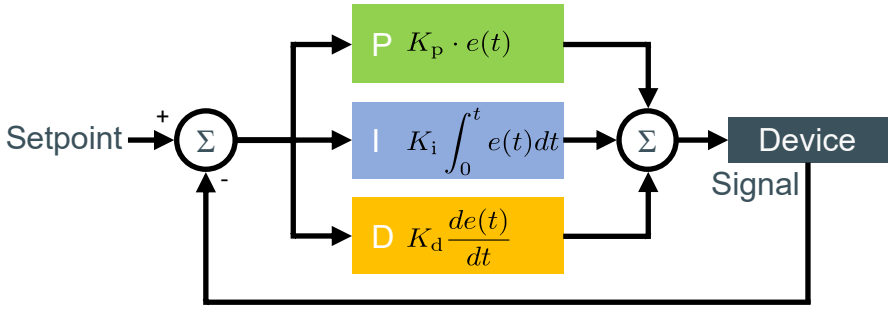

Figure 3.3: Signal path of a PID controller. The signal coming from a measuring device is subtracted from a setpoint, which is the desired signal value. The result is used in three equations. The Proportional (P), Integral (I) and Derivative (D) equation each have separate parameters K. The results from these equations are summed up, and used as an input parameter of the device.[34]

The feedback loop facilitating AFM measurements consists of two essential signal processing components, a lock-in amplifier, and a proportional-integral-derivative (PID) controller. The signal path by which the lock-in amplifier measures the amplitude and phase of the input signal at a specific frequency is illustrated in figure 3.2. In a lock-in amplifier, the input signal is multiplied with a reference frequency. In AFM this is the frequency of the first eigenmode. The multiplication shifts the frequency spectrum of the signal by the reference frequency, whereby the part of the signal at the reference frequency is at 0 Hz. Afterwards, a low-pass filter is applied, attenuating all parts of the signal around 0 Hz above a certain frequency. This leaves a direct current (DC) signal with the amplitude of the original signal at the reference frequency. To account for the phase of the input signal, in dual-phase demodulation, the demodulation is done twice, with the reference signal shifted by 90°. The real (X) and imaginary (Y) components of the oscillation can then be converted into polar coordinates to obtain the amplitude R and phase Φ of the Signal.[35]

The signal path of the PID controller is shown in figure 3.3. The PID controller uses a signal from a device as an input variable. In AFM this would be the oscillation amplitude. This

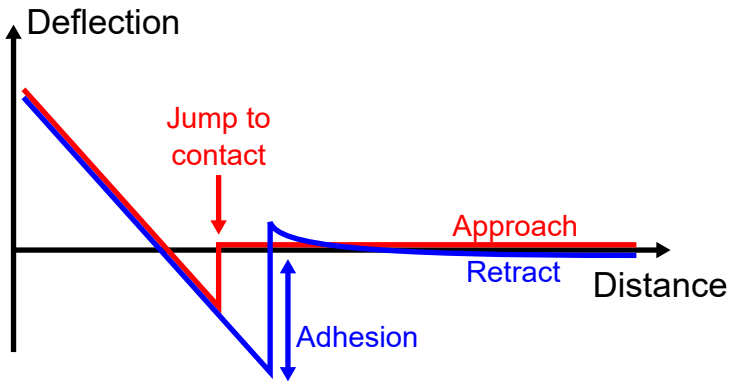

Figure 3.4: Illustration of an atomic force spectroscopy (AFS) curve. The red curve represents the approach of the cantilever from right to left. Negative deflection values indicate downward bending of the cantilever, as is the case at the jump to contact. As the cantilever presses on the sample, positive deflection values indicate the upward bending of the cantilever. Similarly, the blue curve shows the retraction from left to right.

signal is subtracted from a given setpoint, which in AFM is the desired amplitude of the oscillation, giving the error parameter $e(t)$. As the name suggests, proportional, integral and differential equations are solved, using this parameter. The respective results are multiplied with the parameters K_p, K_i and K_d, often just called P, I and D. The results of this are summed up, and the sum is used as an input parameter of the device, closing the loop. In AFM, this would for example control the tip height. If the PID parameters are set correctly, then the loop automatically adjusts the tip height to maintain a constant oscillation amplitude. Based on these general mechanism, many different AFM methods have been developed, expanding the applications and tackling practical challenges in AFM imaging.[11]

An early method, is AFS, where the tip is approached to and retracted from the sample, while the vertical deflection is recorded. Such an AFS curve is shown in figure 3.4. As the cantilever is approached to the sample, its deflection remains constant. Just above the sample surface, attractive forces between the tip and the sample lead to a jump to contact. The downward bending of the cantilever is measured as a negative deflection. As the cantilever is approached further, the bending reverses, until the cantilever is straight again. At this point the recorded distance indicates the actual height of the sample. Further approaching leads to bending of the cantilever with a positive deflection until a set force is reached.[11]

As the cantilever is retracted, the bending reverses. Attractive (adhesion) forces keep the tip in contact. When these forces are overcome by further retraction, the tip snaps out of contact. The cantilever is retracted further until the oscillations, caused by the snap, stop. Afterwards this process can be repeated. This kind of spectroscopy can be used to determine local mechanical properties of samples.[11]

In scanning AFM methods, the sharpness of the AFM tip, makes damages to it by large and hard structures on the sample one of the most common problems. Especially for samples with an unknown topography due to difficulties in fabrication or contamination, imaging

large areas can be challenging. To account for this, the proprietary quantitative imaging (QI) mode of the company Bruker can be used.
In QI mode, the tip is scanned across the sample. But instead of continuous imaging as in tapping mode, each pixel is imaged independently. At every pixel, an AFS curve is measured, and the height of the sample is recorded. Thereby, the retracting distance can be set to be larger than the largest possible structures, averting damage to the tip. Even though this is slower than conventional imaging, this mode is especially useful, to roughly map out a sample before more accurate measurements, allowing for larger structures to be located and avoided.[36]

3.2 Kelvin Probe Force Microscopy

3.2.1 Basic Principles

The general concept of a Kelvin probe is based on an experiment by Lord Kelvin at the end of the 19$^{\text{th}}$ century. He used a parallel-plate capacitor, made from copper and zinc, to show that upon contact, electrons flow from the zinc to the copper plate. After this charge transfer, the capacitor was charged.[37]
The capacitance C of such a capacitor is given by

$$C = \epsilon\epsilon_0 \frac{A}{z}, \tag{3.1}$$

where ϵ is the permittivity of the medium between the plates, ϵ_0 is the vacuum permittivity, A is the area of the plates and z is their distance. The amount of charge a capacitor holds depends on its capacitance and the total potential difference of the plates, with $Q = CV$.[38]
When the plates in Lord Kelvin's experiment were vibrated along the z axis, an alternating current (AC) was observed flowing through the cable connecting the two, with the current's frequency being equal to the vibration's frequency. The total potential difference between the probe and the sample was varied by an external potential, until the observed current became zero. No charges flowed between the plates since the external potential was equal to the negative internal potential difference, nullifying the total potential difference.[37]
The initial charge transfer in Lord Kelvins experiment resulted from the work function difference of the two plates. As shown in section 2.2, upon contact of the plates their Fermi levels are equalized, by the flow of electrons from the plate with the lower work function to the plate with the higher work function.
As the resulting internal potential difference can be determined by the experiment described above, this means that if the work function of one plate is known, the work function of the other can be determined as well. Thereby, samples of unknown work function can be characterized by a probe with a known work function, which is then called a Kelvin probe and

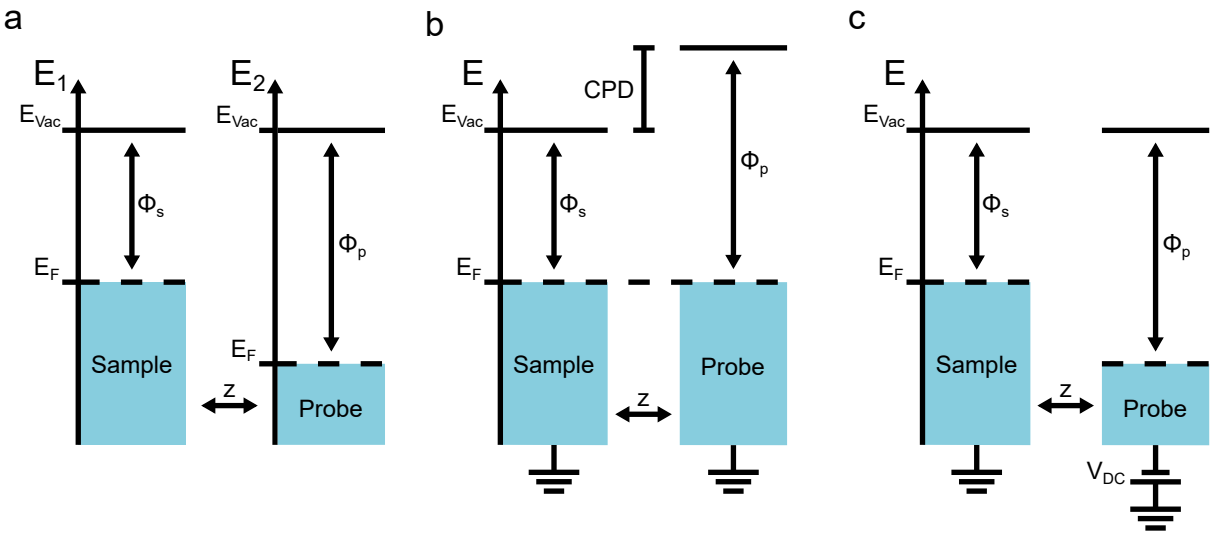

Figure 3.5: Illustration of the energy levels during a Kelvin probe measurement. a) Before making a connection, the energies of the sample and the probe are independent from each other. b) Being connected to the same reference ground, the Fermi levels equalize, by charging the capacitor system. c) The capacitor is discharged and the CPD nullified, by the application of a constant bias V_{DC}.

the internal potential difference is called the contact potential difference (CPD).[39]
Ideally the CPD is the difference of the work functions of the probe Φ_{p} and the sample Φ_{s}, as given by

$$V_{\mathrm{CPD}} = \frac{\Phi_{\mathrm{p}} - \Phi_{\mathrm{s}}}{e}, \tag{3.2}$$

where e is the elemental charge.[34]
An illustration of the energy levels during the process of using a Kelvin probe is shown in figure 3.5. The energy levels of the sample and the probe are independent from each other as long as they are not connected, as is shown in figure 3.5a. Figure 3.5b shows the equalized Fermi levels upon connection of the sample and the probe to a common ground. This is often depicted by a direct connection of the probe to the sample, which however does not reflect the practical experiment where the connection is indirect through the ground. Referencing both the sample and the probe to the same ground equalizes the Fermi levels, as it creates one system in thermodynamic equilibrium. In figure 3.5c the energies of the sample and the probe are still referenced to the same ground, but the potential of the probe is adjusted by a constant bias V_{DC} which is equal to $-V_{\mathrm{CPD}}$. This variation might as well take place at the sample though.[34]
The energy of such a capacitor system depends on its capacitance C and the sum of all potentials V_{tot} between the plates, with

$$E = \frac{1}{2} C V_{\mathrm{tot}}^2. \tag{3.3}$$

The force F acting on the plates is given by

$$|F| = \frac{\partial E}{\partial z}. \tag{3.4}$$

This potential-dependent force gives rise to the idea of combining such a Kelvin probe with a force sensitive experiment such as AFM, to determine potential differences at a nanoscopic resolution.[40]
In KPFM, a metallized AFM tip is used as the probe. Instead of a force being applied to the cantilever via the vibration, and the resulting current being measured, an alternating voltage V_{AC} is applied to the tip, and the resulting alternating force is measured at the same frequency ω_{E}. The reason for this is the high force sensitivity of the AFM setup. The sum of all potentials V_{tot} is given by the CPD with V_{CPD}, the nullifying potential V_{DC} and the alternating voltage V_{AC}. The insertion of V_{tot} along with equation 3.3 into equation 3.4 gives the electrical force

$$F_{\mathrm{E}} = \frac{1}{2}\frac{\partial C}{\partial z}\left(V_{\mathrm{DC}} + V_{\mathrm{AC}} \cdot \sin(\omega_{\mathrm{E}} t) - V_{\mathrm{CPD}}\right)^2, \tag{3.5}$$

with t being the time. As with AFM, there are a number of different operation modes for KPFM.[34,41]

3.2.2 Amplitude-Modulation Mode

A commonly used KPFM mode is the amplitude-modulation (AM) mode, which is the foundation of many other modes. The electrical excitation and detection is regarded independently from any mechanical motion. In AFM, each line is scanned twice in a trace and a retrace. One option for AM KPFM is to use the retrace at a constant distance from the sample, the topography of which is measured in the trace. In the retrace, no mechanical excitation takes place so the first eigenmode of the cantilever can be used for electrical excitation. The resulting force is measured by a lock-in amplifier and nullified by V_{DC}, which is adjusted by a PID controller. Due to the distance to the sample (5-10 nm), the spatial resolution of this mode is lower than that of other modes, which work closer to the surface.
To show that the amplitude of the force at the frequency of the electrical excitation can be nullified by adjusting V_{DC} to be equal to V_{CPD}, the quadratic expression in equation 3.5 can be expanded to give

$$F_{\mathrm{E}} = \frac{1}{2}\frac{\partial C}{\partial z} \cdot \Bigg[\Big(2(V_{\mathrm{DC}} - V_{\mathrm{CPD}}) \cdot V_{\mathrm{AC}} \cdot \sin(\omega_{\mathrm{E}} t) \Big) - \left(\frac{1}{2} V_{\mathrm{AC}}^2 \cdot \cos(2\omega_{\mathrm{E}} t) \right) + \left((V_{\mathrm{DC}} - V_{\mathrm{CPD}})^2 + \frac{1}{2} V_{\mathrm{AC}}^2 \right) \Bigg]. \tag{3.6}$$

This shows that three different terms make up the electrical force, with

$$F_{\mathrm{E}} = F_{\omega_{\mathrm{E}}} + F_{2\omega_{\mathrm{E}}} + F_{\mathrm{stat}}. \tag{3.7}$$

The forces acting on the cantilever at the frequencies ω_{E}, $2\omega_{\mathrm{E}}$ and the static forces are:

$$F_{\omega_{\mathrm{E}}} = \frac{\partial C}{\partial z} \cdot (V_{\mathrm{DC}} - V_{\mathrm{CPD}}) \cdot V_{\mathrm{AC}} \cdot \sin(\omega_{\mathrm{E}} t), \tag{3.8}$$

$$F_{2\omega_{\mathrm{E}}} = -\frac{1}{4}\frac{\partial C}{\partial z} \cdot V_{\mathrm{AC}}^2 \cdot \cos(2\omega_{\mathrm{E}} t) \tag{3.9}$$

and

$$F_{\mathrm{stat}} = \frac{1}{2}\frac{\partial C}{\partial z} \cdot \left((V_{\mathrm{DC}} - V_{\mathrm{CPD}})^2 + \frac{1}{2} V_{\mathrm{AC}}^2 \right). \tag{3.10}$$

Equation 3.8 shows that when a DC voltage equal to the CPD between the tip and the sample is applied to the tip, the force with the frequency of the AC voltage becomes zero.
If the maximum demodulation bandwidths of the AFM detector and the KPFM lock-in amplifier are high enough, the second eigenmode of the cantilever can be used for electrical excitation and detection. Multiple lock-in amplifiers are able to each detect signals at different frequencies independently from each other, even if the input consists of mixed signals. Therefore, the first and second eigenmodes are demodulated independently from each other, and AFM and KPFM can be measured simultaneously, during both trace and retrace. This concept, represented by the signals over a frequency range is shown in figure 3.6.[34]
It is important to keep in mind, that KPFM probes are usually not only metallized at the tip, but over the whole cantilever. Therefore, the whole cantilever acts as a KPFM probe. The Signal in AM KPFM is proportional to the capacitance gradient. The large surface area of the cantilever, compared to the tip, compensates in part for its larger distance to the sample. This leads to a significant part of the KPFM signal originating from the cantilever and the tip's cone. This not only reduces the lateral resolution, but also enables crosstalk between the cantilever and far off electrodes beneath it.[34]
Along with the forces already discussed, amplitude modulation in general leads to frequency mixing between a carrier F_{ω} and a modulation F_{μ} signal. This creates sidebands at the frequencies $\omega - \mu$ and $\omega + \mu$. For these, the sideband equation

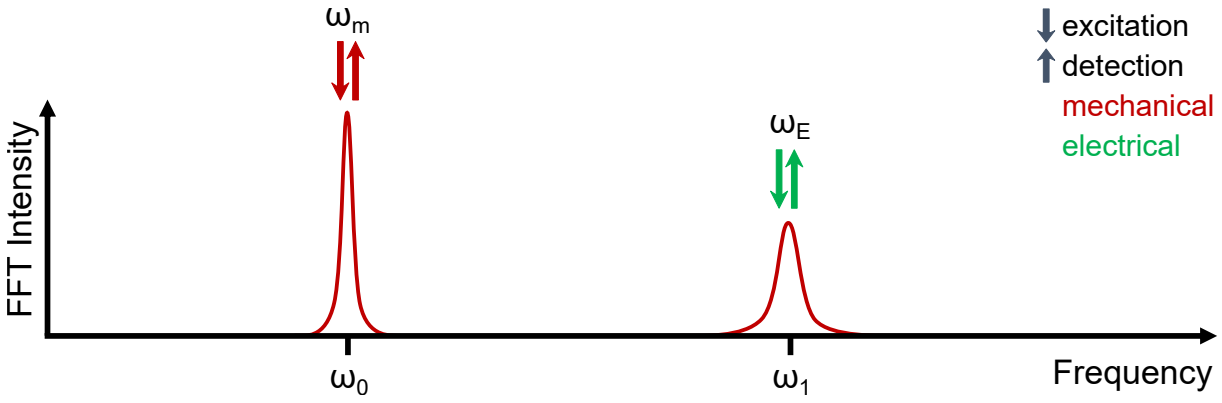

Figure 3.6: Frequency spectrum of the signals arising in AM KPFM. The mechanical signal ω_m is excited and detected at the first eigenmode ω_0 and the electrical signal ω_E is excited and detected at the second eigenmode ω_1.[34]

$$f_{AM} = A_0 \left(\sin(\omega t) + \frac{1}{2} k_a \cdot \cos\left((\omega - \mu) t\right) - \frac{1}{2} k_a \cdot \cos\left((\omega + \mu) t\right) \right), \tag{3.11}$$

can be derived, where A_0 is the mean amplitude and $A_0 k_a$ is the modulation amplitude. For AM KPFM, the carrier frequency ω and the modulation frequency μ would be given by the mechanical and the electrical excitation respectively. Even though the sidebands of the mechanical and electrical excitation do occur in AM KPFM, they are generally not considered. The creation of sidebands does however play an important role in frequency-modulation (FM) KPFM.[34, 41]

3.2.3 Frequency-Modulation Mode

When an AC voltage is applied to the cantilever during mechanical motion, not only its amplitude is modulated, but also its resonance frequency. Caused by the periodical potential difference, a periodical force F_{ts} between the tip and the sample arises. It can be shown that this periodical force results in an effective spring constant

$$k_{eff} = k - \left(\frac{\partial F_{ts}}{\partial z} \right) \Big|_{z=z_0}. \tag{3.12}$$

Here, k is the spring constant for no force field and z is the tip-sample distance.[34]
Based on Hooke's law, this, along with the cantilevers mass m, gives an effective resonance frequency

$$\omega_{0,eff} \approx \sqrt{\frac{1}{m} \left(k - \frac{\partial F_{ts}}{\partial z} \right) \Big|_{z=z_0}}. \tag{3.13}$$

The cantilever is mechanically excited at a constant frequency ω_m, close to its first resonance frequency. With the resonance frequency changing however, the phase of the mechanical

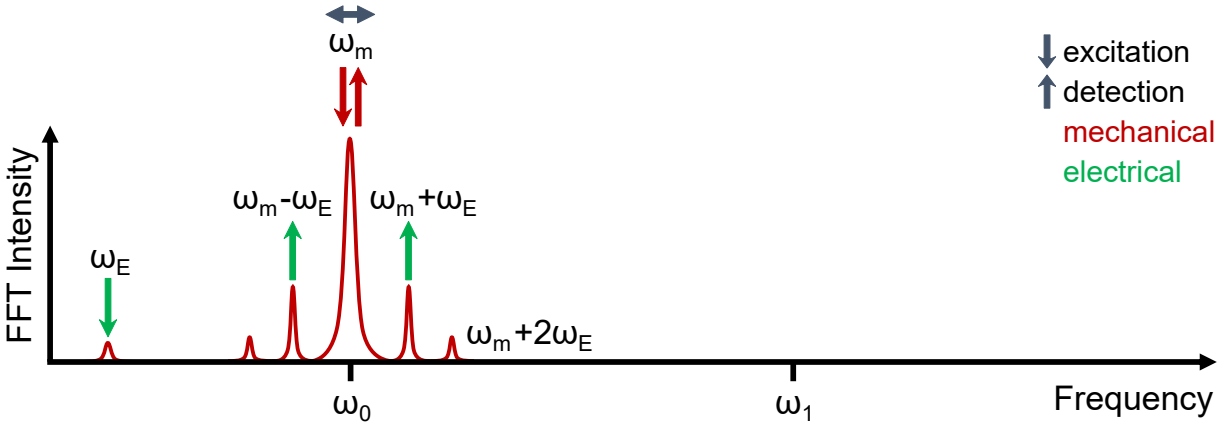

Figure 3.7: Frequency spectrum of the signals arising in FM KPFM. The mechanical signal ω_m is excited and detected at the first eigenmode ω_0. The electrical signal ω_E is excited in the low-kilohertz range. The detection of the electrical signal takes place at one of the sidebands $\omega_\mathrm{m}-\omega_\mathrm{E}$ or $\omega_\mathrm{m}+\omega_\mathrm{E}$.[34]

oscillation relative to its excitation changes as well. Lastly, this oscillating phase shift corresponds to an oscillation of the frequency of the cantilevers physical movement. Therefore, the mechanical oscillation of the cantilever is frequency modulated by the electrical excitation.[34]

It can be shown that the general sideband equation for FM is

$$f_\mathrm{FM} = A\cdot\Big[\sin(\omega_0 t)\cdot J_0(m_\omega) + \sum_{n=1}^{\infty} J_\mathrm{n}(m_\omega)\cdot(-1)^{n+1}\Big(\sin\Big((\omega_0+n\mu)t\Big)-\sin\Big((\omega_0-n\mu)t\Big)\Big)\Big]. \tag{3.14}$$

Here, A is the amplitude, ω_0 is the carrier frequency and μ is the modulation frequency. $J_\mathrm{n}(m_\omega)$ are Bessel functions of the first kind, n^th order with the modulation index m_ω, which is proportional to the ratio between ω_0 and μ. An infinite number of sidebands are created at $\omega+n\mu$ and $\omega-n\mu$, with the carrier frequency ω and the modulation frequency μ again given by the mechanical and the electrical excitation respectively. The amplitude of these decreases for an increasing n so that in practice only the first are considered.[42]

Figure 3.7 shows the sidebands arising at different frequencies, due to the mechanical and electrical excitation. FM KPFM uses the sidebands for the detection of the cantilever's response to the electrical excitation. The forces which act at the frequencies of the sidebands in FM KPFM can be derived from an oscillating tip-sample distance $z(t)$ and the capacitance gradient $C' = \frac{\partial C}{\partial z}$. This distance can be defined as

$$z(t) = z_0 + A_\mathrm{m}\cdot\cos(\omega_\mathrm{m} t), \tag{3.15}$$

with z_0 as the mean tip height and A_m and ω_m as the mechanical oscillation amplitude and frequency. The capacitance gradient is approximated by a Taylor series around the mean tip height as

$$C'(z) = \sum_{n=0}^{\infty} \frac{1}{n!} \frac{\partial^n C'}{\partial z^n} (z - z_0)^n. \tag{3.16}$$

Inserting equation 3.15 into equation 3.16 and solving until $n = 1$ gives

$$C'(z) = C' + A_\mathrm{m} C'' \cdot \cos \omega_\mathrm{m} t \tag{3.17}$$

for the first pair of sidebands. The capacitance gradient $C'(z)$ can be inserted into equation 3.6 to account for the influence of the cantilever motion on the electrical force over time, which is now defined as

$$\begin{aligned} F_\mathrm{E} = \frac{1}{2}\left(C' + A_\mathrm{m} C'' \cdot \cos \omega_\mathrm{m} t\right) \cdot \Bigg[& \Big(2(V_\mathrm{DC} - V_\mathrm{CPD}) \cdot V_\mathrm{AC} \cdot \sin(\omega_\mathrm{E} t)\Big) \\ & - \left(\frac{1}{2} V_\mathrm{AC}^2 \cdot \cos(2\omega_\mathrm{E} t)\right) \\ & + \left((V_\mathrm{DC} - V_\mathrm{CPD})^2 + \frac{1}{2} V_\mathrm{AC}^2\right)\Bigg]. \end{aligned} \tag{3.18}$$

Analogous to the electrical force in AM KPFM, this term can be divided into its spectral components, which are:

$$F_{\omega_\mathrm{E}} = C' \cdot (V_\mathrm{DC} - V_\mathrm{CPD}) \cdot V_\mathrm{AC} \cdot \sin(\omega_\mathrm{E} t), \tag{3.19}$$

$$F_{2\omega_\mathrm{E}} = -\frac{C'}{4} \cdot V_\mathrm{AC}^2 \cdot \cos(2\omega_\mathrm{E} t), \tag{3.20}$$

$$F_\mathrm{stat} = \frac{C'}{2} \cdot \left((V_\mathrm{DC} - V_\mathrm{CPD})^2 + \frac{1}{2} V_\mathrm{AC}^2\right), \tag{3.21}$$

$$F_{\omega_\mathrm{m} \pm \omega_\mathrm{E}} = \frac{A_\mathrm{m} C''}{2} (V_\mathrm{DC} - V_\mathrm{CPD}) \cdot V_\mathrm{AC} \Big[\sin\left((\omega_\mathrm{E} - \omega_\mathrm{m}) t\right) + \sin\left((\omega_\mathrm{E} + \omega_\mathrm{m}) t\right)\Big], \tag{3.22}$$

$$F_{\omega_\mathrm{m} \pm 2\omega_\mathrm{E}} = -\frac{A_\mathrm{m} C''}{8} \cdot V_\mathrm{AC}^2 \Big[\cos\left((2\omega_\mathrm{E} - \omega_\mathrm{m}) t\right) + \cos\left((2\omega_\mathrm{E} + \omega_\mathrm{m}) t\right)\Big] \tag{3.23}$$

and

$$F_{\omega_\mathrm{m},\mathrm{el}} = \frac{A_\mathrm{m} C''}{2} \cos(\omega_\mathrm{m} t) \cdot \left((V_\mathrm{DC} - V_\mathrm{CPD})^2 + \frac{1}{2} V_\mathrm{AC}^2\right). \tag{3.24}$$

Equations 3.19 through 3.21 are identical to the equations for AM KPFM, showing that these still hold true. The sideband equation 3.22 shows the same characteristic for the force at

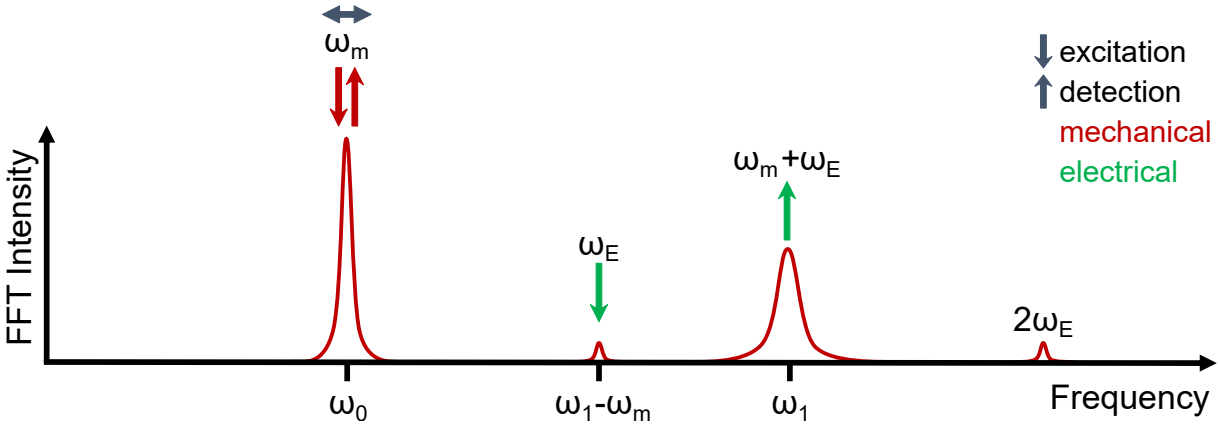

Figure 3.8: Frequency spectrum of the signals arising in H KPFM. The mechanical signal ω_m is excited and detected at the first eigenmode ω_0. The electrical signal ω_E is excited at $\omega_1 - \omega_m$. The detection of the electrical signal takes place at the second eigenmode ω_1. The infinite number of additional sidebands are not shown.[34]

these sidebands as the force at ω_E, meaning that the amplitude of the sidebands becomes zero when $V_{DC} = V_{CPD}$. Therefore the first sidebands can be used in the same way to determine the CPD.[34]

The main advantage over AM KPFM is that the force at the sidebands is proportional to the capacitance curvature instead of the gradient. As the capacitance curvature diminishes much faster, with increasing distance from the sample surface, than the gradient, the parts of the probe closer to the sample contribute more to the overall signal. This decreases the effect of the stray capacitance of the cantilever so significantly that it can be disregarded and the spatial resolution is increased to approximately the tip diameter.[43]

In FM KPFM usually a frequency in the low-kilohertz range is used for the excitation. Thereby the sidebands occur close to the mechanical excitation frequency, and therefore benefit from the amplification of the first eigenmode of the cantilever. For this to work however, the frequency-width of the mechanical oscillation must be narrow enough for the sidebands to be distinguishable.[44]

3.2.4 Heterodyne Mode

FM KPFM is often performed in a vacuum, in order to exploit sharper frequencies of the mechanical oscillation and generally lower noise levels, aiding the discrimination of the sidebands from the noise and mechanical oscillation. Performing measurements in a vacuum usually requires specialized (and expensive) equipment and also comes with an increase in the workload. Therefore the range of experiments performed is less versatile. A solution to the need of a narrow frequency-width of the mechanical oscillation is usage of the second eigenmode of the cantilever for the amplification of a sideband. This of course requires lock-in amplifiers which are able to demodulate the signal at these frequencies of up to 500 kHz.

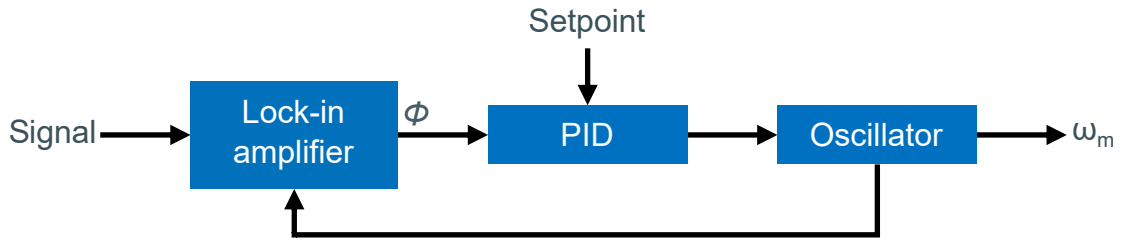

Figure 3.9: Signal path of a PLL. The phase difference between an oscillator and a signal is measured by a lock-in amplifier. This phase is send to a PID controller, which controls the oscillator with the aim to match the phase to the Setpoint. The oscillators frequency and phase is the output of the PLL.[34]

Figure 3.8 shows how the electrical excitation frequency is chosen so that $\omega_m + \omega_E$ equals the second eigenmode ω_1. Thereby, the sidebands frequency is clearly separated from the mechanical oscillation, decreasing the crosstalk between the two. This excitation and detection scheme, will be called heterodyne (H) KPFM. This method combines the high resolution of FM KPFM with the ease of use of AM KPFM.[34]

As with FM KPFM, one hurdle to overcome is the changing phase and frequency of the mechanical oscillation. As was shown in section 3.2.3, the movement of the cantilever and its interaction with the sample, leads to an oscillating effective resonance frequency, which effects the mechanical oscillation at the first eigenmode. For the frequency and phase of the second eigenmode this effect is negligible. However, the effective resonance frequency affects the sidebands created by this oscillation. Therefore, to keep the sideband constant at the second eigenmode, the electrical excitation frequency and phase have to constantly change as well.[34]

The changing mechanical oscillation is tracked by a phase-locked loop (PLL), the signal path of which is shown in figure 3.9. In this PLL, the signal from the AFM photodetector is initially demodulated at around the frequency, where the mechanical oscillation is expected. The lock-in amplifier gives the phase information of this to a PID controller, whose setpoint is zero. The PID controller in turn controls the oscillator which is used as the reference signal for the lock-in amplifier, closing the loop. Thereby, the oscillator dynamically gives out a signal whose frequency and phase is always adjusted to that of the actual mechanical oscillation of the cantilever. At the same time, this signal ω_m is used to calculate the electrical excitation $\omega_1 - \omega_m = \omega_E$ so that $\omega_m + \omega_E = \omega_1$ remains constant. The sideband at ω_1 can now be demodulated for KPFM.[45]

3.3 Scanning Photocurrent Microscopy

Simple optoelectronic devices, often consist of a semiconductor material, which is contacted by metal electrodes. Analysis of the response to illumination can give insights into the de-

vices properties, not only with respect to the semiconductor itself, but also its contact interfaces to the electrode material. Illumination excites charge carriers into the conduction band of the semiconductor whereby its conductivity is increased along with the measured current of the device. The current which is induced by optical excitation is called photocurrent. In order to perform experiments on a device with regard to its photocurrent characteristics with a high spatial resolution, SPCM was developed.
In SPCM, the device is biased by applying a voltage to the source electrode and measuring the current. A laser, with an energy above the semiconductors band gap, scans the device. For each position of the laser, the resulting current is measured. Thereby a SPCM map is created, revealing the optically active regions of the probed device. Especiall, the two contact types discussed in section 2.2.2 can be distinguished using SPCM.[46, 47]

3.3.1 Schottky Behavior

The separation and movement of excited charge-carriers is facilitated by electric fields. As the electric field is the negative 1st derivative of the electrostatic potential, in-built and external electric fields are indicated in band diagrams as changes in potential or energy. In basic devices with two Schottky contacts, these changes occur in the SCRs at the semiconductor-metal interfaces. Therefore, only charge-carriers, excited in these regions, contribute to a current.
It is important that with regards to a steady-state photocurrent, for each excited electron reaching an electrode, an excited hole has to reach the other electrode. Otherwise, the device would charge up over time, creating opposing electric fields, which in turn inhibit current flow.[47]
Figure 3.10 shows band diagrams of an n-type Schottky device under negative (a) and positive (b) bias, along with schematic SPCM profiles. The negatively biased source electrode in figure 3.10a is expressed by the increased source energy relative to the drain. The change of the source energy does not change the barrier height from source electrode to the semiconductor. The potential difference in the SCR of the semiconductor however does increase. Thereby the electric field in this region is also increased, which in turn increases charge-carrier separation. This is observed in the SPCM profile in figure 3.10c. As the laser is scanned along the device with different biases, only the illumination of the source SCR yields a measurable current, which increases for higher potential differences. Under illumination of the drain SCR, excited charges would theoretically also be separated in some capacity, but the resulting current will be much lower, as the forward biased Schottky contact does not exhibit an increased electric field.
Figures 3.10b and d show the analogous behavior for positive biases at the source. As the source contact is forward biased, electrons are extracted from the semiconductor, charging

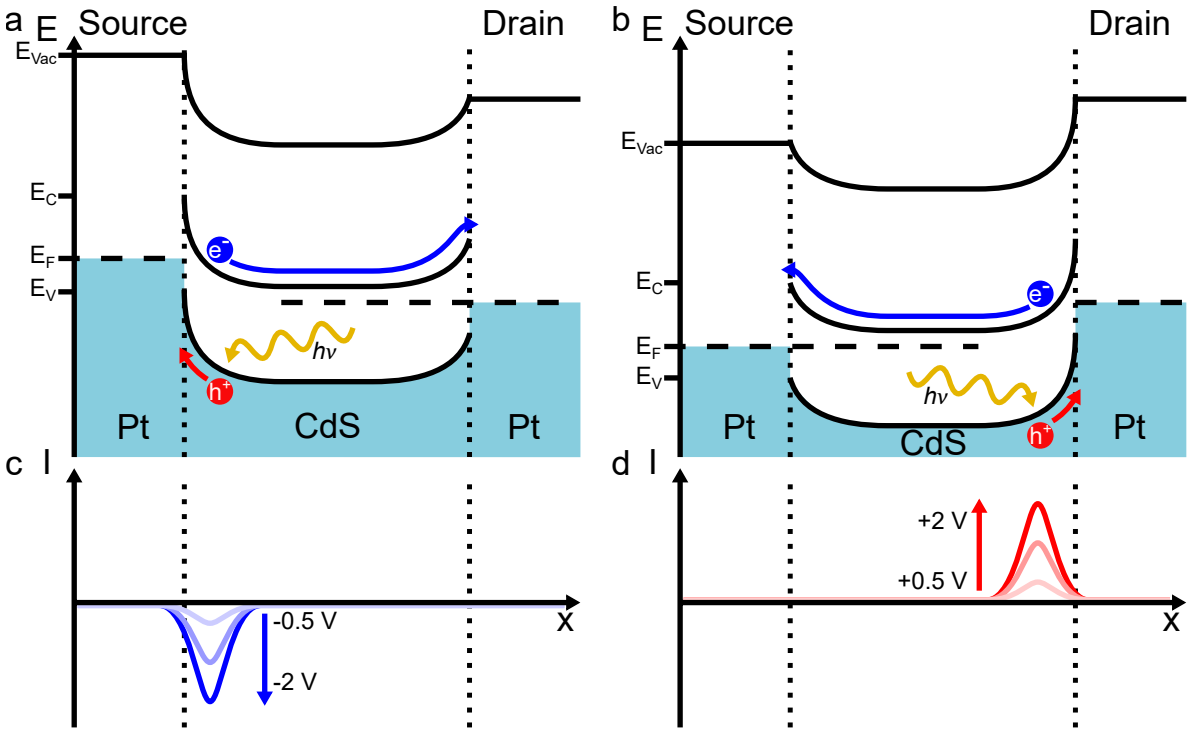

Figure 3.10: Illustrations of an n-type Schottky device under illumination, with a) a negative (source in reverse) and b) a positive (drain in reverse) biased source electrode. The position where charge-carriers, which contribute to a photocurrent, are excited is indicated by the yellow arrow. Exemplary photocurrent profiles are illustrated for c) a negative and d) a positive biased source electrode.

it positively. The drain contact is biased in reverse, increasing the SCR there. Thereby, positive photocurrents are observed in the drain SCR.[48]

3.3.2 Ohmic Behavior

In devices with two ohmic contacts, the application of a bias at the source electrode has a different effect on the semiconductor's potential, compared to a Schottky device. A band diagram of an ohmic device is shown in figure 3.11. As a negative bias is applied to the source electrode, not only its energy is increased, but also that of the semiconductor at the source contact, while the grounded drain contact remains its original energy. As the semiconductor electrically connects the two electrodes at different biases without significant barriers, the energy drops linearly across the semiconductor. The energy courses in the SCRs do not share this linearity, but will not be taken into account. A linearly decreasing energy corresponds to a linearly increasing potential, which indicates a constant, nonzero electric field in the semiconductor. This electric field separates excited charge carriers for every illumination position of the semiconductor, in contrast to the Schottky device, where charge-carrier separation was limited to the SCRs.[21]

In this device, the different mobilities of the electrons and holes become significant. For n-

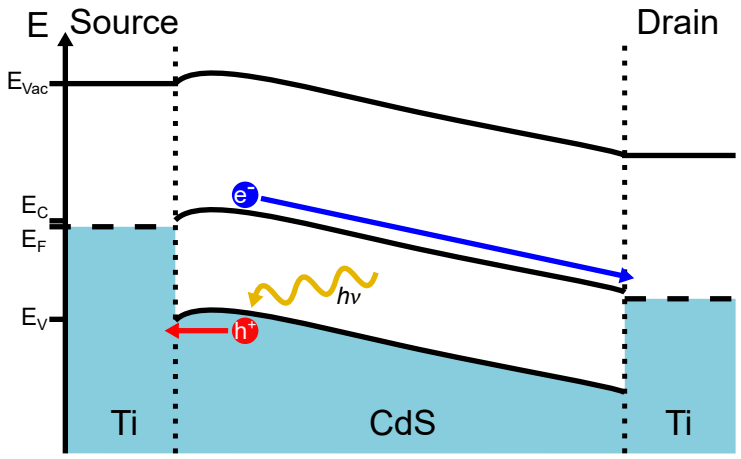

Figure 3.11: Band diagram of an ohmic device with a negatively biased source. Charge carriers are separated regardless of the illumination position.

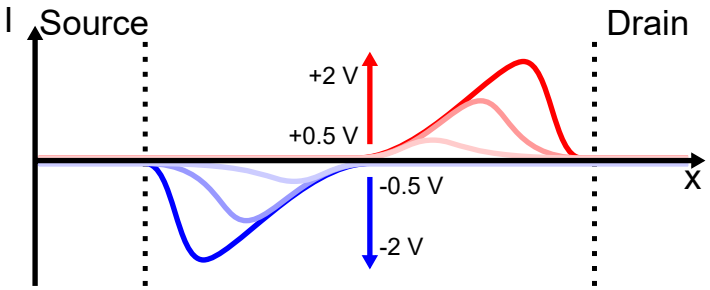

Figure 3.12: Exemplary SPCM profiles for an ohmic device, with different biases applied at the source.

type CdS, it was shown that the electrons (majority charge carriers) have higher mobilities than the holes. In SPCM experiments, this leads to the photocurrent being mainly limited to the excited holes ability to reach a contact.[49]

For different biases, SPCM profiles are illustrated in figure 3.12. For negative biases, a maximum is observed closer to the hole collector electrode (source) than to the electron collector (drain). This maximum shifts towards the source contact for more negative biases. The decreasing current away from this maximum to the electron collector (drain), is associated with decreased ability of excited holes reaching the source contact, thereby the current in this region is hole-limited. *Vice versa*, the decreasing current away from the maximum to the hole collector (source) is associated with a decreasing number of excited electrons reaching the drain contact, indicating an electron-limited current. Since for a steady-state current, both charge-carriers types need to reach their respective collecting electrode, this leads to a maximum current, where the number of holes and electrons reaching their respective contacts is equal and at its maximum.[49]

In the past, Gu *et al.* had used the slopes of the logarithmic SPCM profiles to determine the mobility-lifetime products for electrons and holes. It was assumed that, since the slopes for different biases seem to be equal, the movement of charge carriers toward their respective

collecting electrode is diffusion dominated. Therefore, the diffusion lengths of the charge carriers $L_{\mathrm{h(e)}}$ were extracted by applying an exponential fit to the slopes. The diffusion length is related to the lifetime τ and the diffusion coefficient D by $D = L^2 \cdot \tau$. This can be inserted into the Einstein-Smoluchowski relation in 2.5 to yield

$$\mu\tau = \frac{qL^2}{k_\mathrm{b}T}. \tag{3.25}$$

Thereby values for the electron's and hole's mobility-lifetime product were obtained. The mobility, which comes in units of $\frac{\mathrm{m}^2}{\mathrm{Vs}}$, itself however was not obtained, because the experiments were not time resolved, whereby no value with a relation to time could be extracted.[49]
A problem with this approach is the assumption of a diffusion dominated current with equal slopes for different biases. Graham *et al.* calculated that if the difference in mobilities of the charge-carrier types is large enough, excited charge carriers would distribute themselves unevenly across the semiconductor, with one charge-carrier type having a broader distribution than the other. This in turn would create an electric field that superimposes the external electric field, which at last affects the charge-carrier movement and the resulting SPCM profiles and slopes, which would thereby not be equal for different biases. This electric field was experimentally observed by Schäfer *et al.* as presented in section 2.2.3.[25,50]
Effects such as these show that not only external or in-built electric fields need to be taken into account, but also the electric fields generated by the charge carriers themselves. The complex distribution of the charge-carrier distribution creating an electric field, which in turn affects the charge-carrier distribution creates a dynamic equilibrium, which requires self consistent calculations or experiments to be characterized.[50,51]

3.4 Lithography

For any kind of nanoparticle, to be used in an electrical circuit of a device, electrodes need to contact the nanoparticle. The size of these electrodes themselves might vary, but they need to be spatially defined and cleanly separated by only small distances below the size of the particle, which is to be contacted. Thereby, the current flow between these electrodes is facilitated by the nanoparticle, which gives the whole device unique characteristics and applications.
One method to produce electrodes on a sample is optical lithography, where the desired electrode pattern is obtained by locally illuminating a photosensitive material called photoresist; the general procedure of which is shown in figure 3.13. Often, the photoresist is an organic polymer, in a solution. The sample in figure 3.13a is covered by the resist and spun in a spin-coater. Thereby, excess resist is removed while a uniform thin film of around 0.1 µm to 2 µm is left on the sample (figure 3.13b), depending on the rotational speed of the spin-coater. Afterwards, the sample is heated in the softbake process, which evaporates parts the

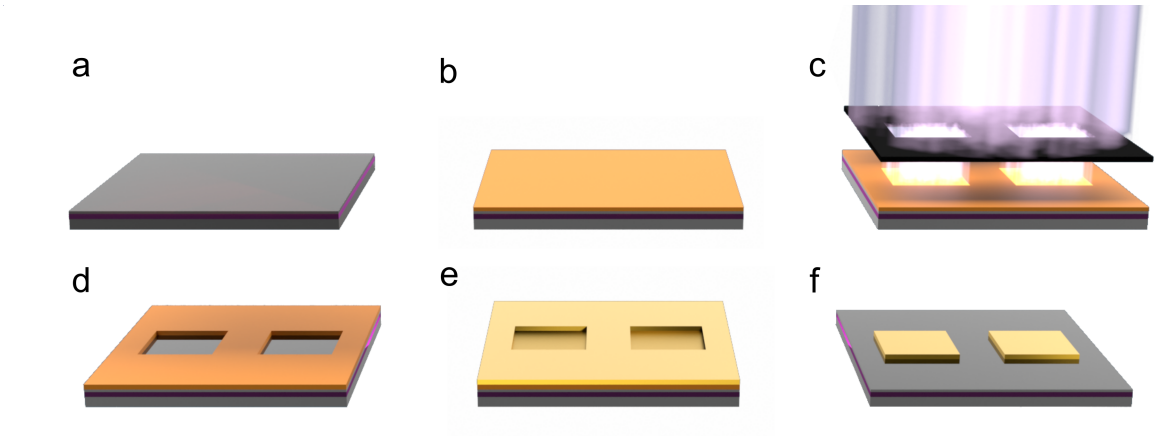

Figure 3.13: Illustration of the stages of optical lithography. a) A plain ITO sample with a SiO_2 top layer and b) after the application of the photoresist. c) The photoresist is illuminated trough a mask. d) After development, the illuminated sections are removed. e) A metal is deposited and f) after the lift off, the desired metal structure is obtained.

solvent from the resist, thereby densifying the film.

When parts of the photoresist are illuminated with sufficient power and wavelength, the illuminated sections of the resist undergo a photochemical reaction. In practice, the local illumination can be achieved by a number of methods. Often a mask is used, to obscure parts of the sample from the light, as shown in figure 3.13c. Alternatively, the sample can be illuminated by a laser or an electron beam (in e-beam lithography) which requires special photoresists.

The illuminated regions of the resist act differently from the unilluminated regions, when the sample is submerged in a developer. For positive photoresists, only the illuminated regions are dissolved by the developer (see figure 3.13d), while for negative photoresists it is only the unilluminated regions. Some types of photoresist require an additional post-exposure bake prior to development to complete the photochemical reaction and stabilize the film.

After development, the desired structure is already transferred to the photoresist. Figure 3.13e shows how when a metal is applied to the sample by evaporation or sputtering, the metal is in direct contact with the sample only where the resist was removed. Therefore, when the remaining photoresist is dissolved in the lift-off process, the metal covering theses regions will be removed as well. In the end, metal structures are obtained, which are defined by the illumination of the sample, as shown in figure 3.13f.[52]

The lithography performed to produce the samples for this work was done by Daniel Lengle. A more detailed description of the process can be found in his PhD thesis.[53]

4 Experimental Part

In this chapter the setup and materials that were used in this work will be discussed. The exact measurement conditions and choice of laser will be addressed in the sections of the respective experiments.

4.1 Used Equipment

The equipment and its model an manufacturer, which was used in this work, is shown in table 4.1, grouped by the respective application.

Table 4.1: Used equipment, model and manufacturer.

	Equipment	Model	Manufacturer
Current	Current amplifier	SR570	Stanford Research Systems
	Lock-in amplifier	MFLI 5 MHz	Zurich Instruments
Optics	Sample Stage	Tip-assisted optics module	Bruker
	488 nm Diode Laser	LDH-D-C-488	Picoquant
	440 nm Diode Laser	LDH-D-C-440	Picoquant
	Laser controller	PDL 800-D	Picoquant
	Power meter	1830	Newport
	APD	PDM series	MPD
	Mirror scanner	GVS012	Thorlabs
	Inverted optical microscope	Axiovert 200	Zeiss
	Oil Objective	Achroplan 44 00 80 100x	Zeiss
	Immersion Oil	Immoil-F30CC	Olympus
	Air Objective	MPlanApo N 100x	Olympus
	Realtime controller	ADwin-Gold	ADWin
	Optical microscope	BX51	Olympus
SPM	Atomic force microscope	Nanowizard 4XP	Bruker
	Cantilever	SCM-PIT-V2	Bruker
	Lock-in amplifier	HF2LI	Zurich Instruments
	Image analysis software	Gwyddion 2.65	Czech Metrology Institute

The cantilevers used for all SPM measurements were made of a silicon and coated with an platinum iridium (PtIr) alloy.

4.2 Synthesis

The synthesis of nanomaterials was not a part of this work. The materials studied, were synthesized by my colleagues. As such, this section will only briefly address the work done by them.

Nanowires

In this work CdS nanowires were studied, which were synthesised by Daniel Lengle, as part of his PhD thesis. The CdS nanowires were synthesized via a solvothermal method. Here, cadmium diethyldithiocarbamate was used as a single-source precursor. Dissolved in ethylenediamine, the reaction took place in an autoclave at 200 °C for 60 h, after which the mixture was allowed to cool down to room temperature for 24 h. The CdS nanowires were isolated by multiple centrifuging and washing steps and finally suspended in ethanol for storage. The exact process and cleaning procedures can be found in his PhD thesis.[53]

Nanosheets

The nanosheets studied in this work were synthesized by Jennifer Schulz. The general SnSe nanosheet synthesis is based on a method by Vaughn *et al.*. Tin chloride dissolved in oleylamine and selenium dissolved in trioctlyphosphine were used as precursors. These were mixed with hexamethyldisilazane and slowly heated to 240 °C. After 30 minutes, the mixture was rapidly cooled. The mixture was centrifuged and the precipitate was washed multiple times with toluene and ethanol. At last, the nanosheets were suspended in toluene.[54]
Framed tin sulfide (SnS)@SnSe nanosheets were obtained by the dropwise addition of sulfur dissolved in oleylamine during the SnSe nanosheet synthesis.[55]
The synthesis of SnSe nanosheets decorated with gold nanoparticles (AuNPs), is based on an approach developed by Tsangas *et al.*. The SnSe nanosheets reacted with chloroauric acid in a solution of oleylamine and oxalic acid at room temperature.[56]

4.3 Sample Preparation

The optical lithography by which the CdS nanowires and the SnS@SnSe-framed nanosheets were electrically contacted, was done by Daniel Lengle.[53]
Two sample types were used, which were, indium tin oxide (ITO) coated borosilicate glass slides (PGO, CEC020T, ≈20 Ω/sq) and only for contacted nanosheets, silicon wafers with a top layer of 300 nm SiO_2 (Si-Tech Inc., N/As,<0.005 Ωcm, LOT-No. 10419).
The ITO coated glass slides were used for measurements, which required both a transparent sample, but a conductive back gate, which was provided by the ITO layer. Both sample types had a size of 2 cm by 2 cm. Another requirement for KPFM and current measurements is an insulating layer, such as the one already provided by the SiO_2 layer on the silicon wafers.

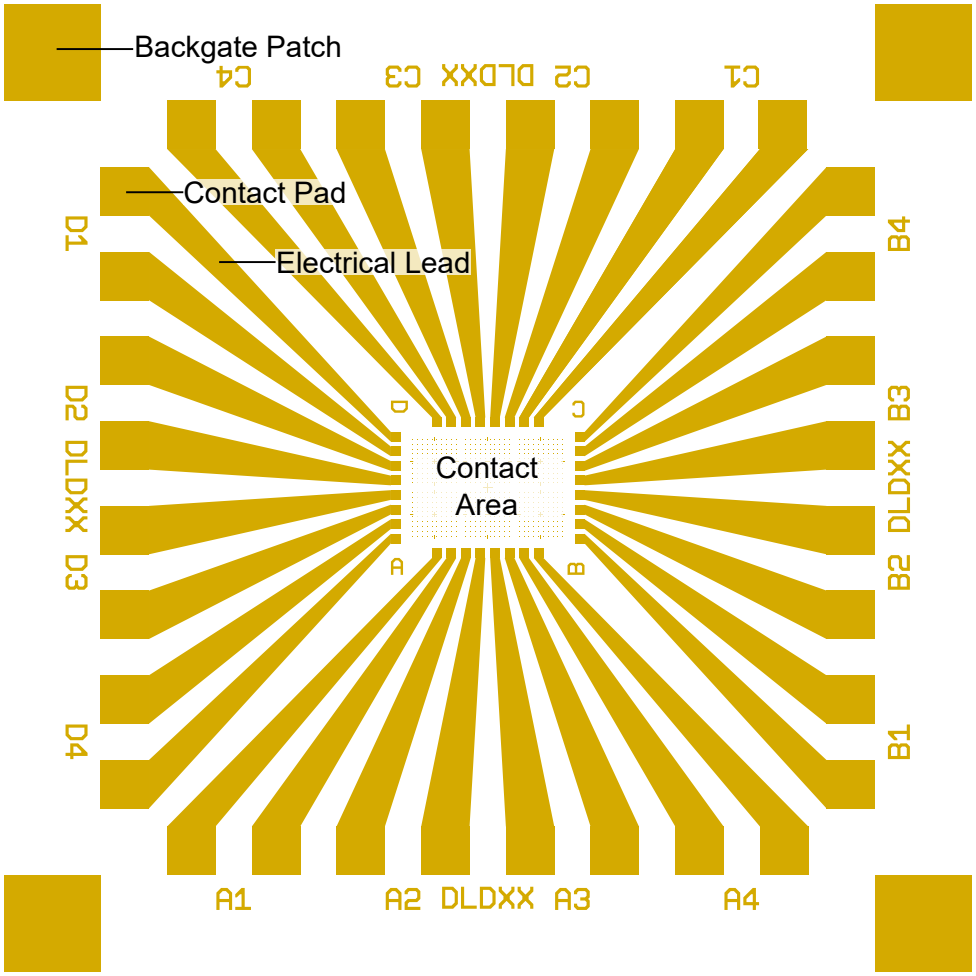

Figure 4.1: Sample design for contacting nanostructures. At the outer edges four square contacts patches have a connection to the ITO backgate. 32 gold electrical leads (8 on each side) can be used for wire bonding on the larger outside contact pad and lithographic electrical connection to nanostructures on the inside. Each pair (source and drain) is labeled by their side A-D and a number 1-4.

To that end, a layer of 300 nm SiO_2 was deposited on top of the ITO layer, using plasma-enhanced chemical vapor deposition (PECVD) by Teemu Hakkarainen of the Tampere University in Finland.

In the first lithography step, gold markers, contact pads and electrical leads were applied to the samples. The design, which was chosen for these is shown in figure 4.1. During the lithography, first 10 nm titanium and then 40 nm gold were evaporated onto the samples. The titanium improved the adhesion of the gold to the surface.
The four edges of the samples had patches, which were scratched open by a diamond cutter, to create a connection to the ITO back gate.
In total, each sample possessed 32 electrical leads, which were grouped in pairs as source and drain contacts, labeled A1 - D4. These leads connected the outer contact pads, which were later used for contacting, with the inner contact area. The size of this area was chosen so

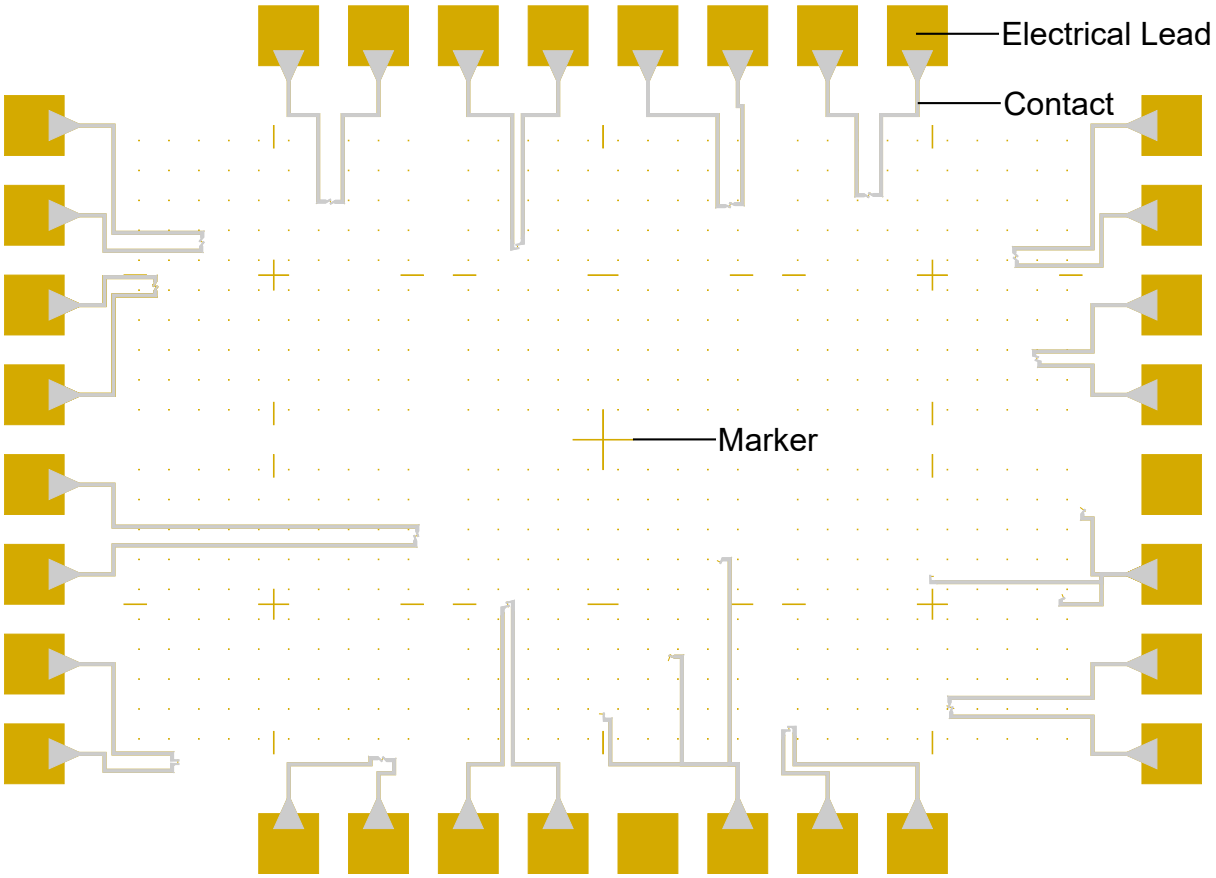

Figure 4.2: Exemplary contact area of a sample. The outer squares represent the inner parts of the gold contact leads shown in figure 4.1. Markers (crosses, lines and points) of gold were applied in the first lithography step for orientation. The gray leads are the electrical connection of the desired contact material made in the second lithography step, connecting the nanostructures to two gold leads.

that the objective below the sample would not collide with the sample holder, when placed in the center directly below a contacted nanowire.

For the deposition of the nanowires, the nanowire suspension was briefly ultrasonicated, and subsequently spincoated onto the sample, in order to separate nanowire bundles and obtain single nanowires in the measurement area. The nanowires were contacted by the desired contact material, again using optical lithography. Figure 4.2 shows the measurements area, along with all markers and the contacts connecting the gold electrical leads to the nanowires.

In some cases, faulty electrical leads could not be used, either because they were broken, or because the had a short circuit to the back gate. In this case, the other lead of the pair was used to contact nanowires on only one side, for other experiments.

For the study of nanosheets, this design was used as well. Due to their smaller size, and therefore more difficult contacting, nanosheets were contacted on Si/SiO_2 substrates. In this case, KPFM and SPCM measurements were not performed simultaneously, but subsequently, as

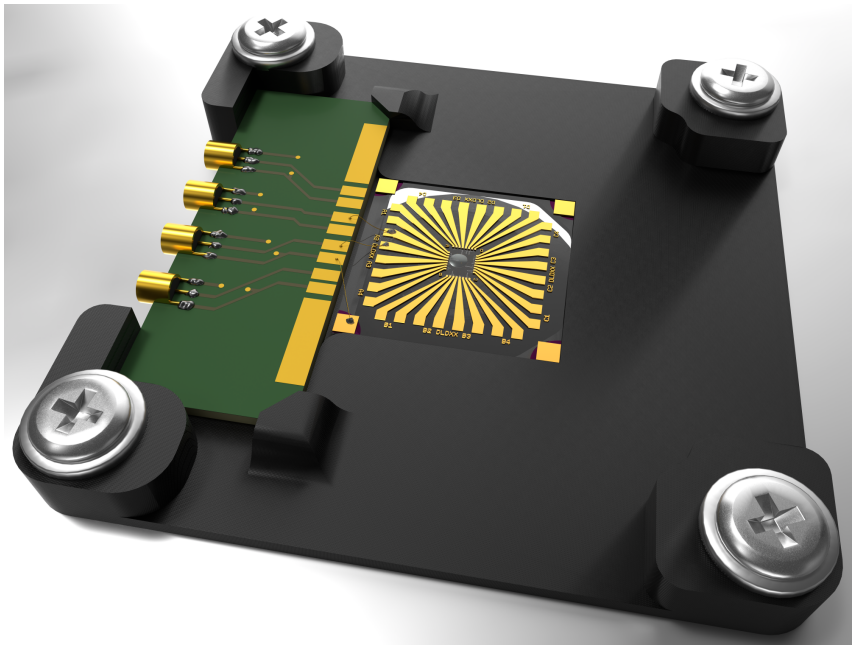

Figure 4.3: Illustration of the sample holder with the chip carrier bonded to a sample.

the sample was turned upside down towards the objective for optical measurements.
Uncontacted nanosheets, were deposited in the measurement area by drop casting 2 µL of the undiluted suspension directly onto the sample. After evaporation, the sample was ultasonicated in isopropanol for 2-3 seconds and dried under nitrogen flow. The ultrasonication step was repeated until multiple single nanosheets, separated from larger clusters which could damage the KPFM tip, were observed by optical microscopy.
After preparation of a sample, it was placed on a 3D-printed sample holder, which was then screwed onto the AFM stage over an opening for the objective. A connected sample is illustrated in figure 4.3.
On the sample holder next to the sample, a selfmade chip carrier could be clamped. The chip carrier housed four BNC adapters, which could be connected to current source and measuring devices. Each BNC adapter was connected to two contact pads, one for grounding and one for the electrical signal. Thereby four electrical signal contact pads could be connected to the source and drain contacts of two nanowires simultaneously, using wire bonding.
For wire bonding a gold wire was used. The first bond was placed on the chip carrier and then the wire was cut to an appropriate length. In order to prevent damage to the sample, the gold wire was not bonded onto the sample, but stuck to it, using conductive silver paste. Thereby, after bonding, an electrical connection between two nanowires and two BNC adapters respectively was created.

4.4 Current Measuring Setup

For current measuring experiments on semiconductor devices, the source contact was connected to the MFLI lock-in amplifier output, which acted as the current source. The drain was connected to the SR570 current amplifier, which converted the current flowing into a voltage. The amplification depended on the maximum current flow during the experiment and was set between 1 nA/V and 1 mA/V. The value was set so that the maximum current flow would result in a bias of about 1 V. This output was sent to the voltage input of the MFLI lock-in amplifier to be measured. This way, the lock-in could continuously record the current, while applying or sweeping the bias at the source contact.
In this setup, a negative bias at the source would create a negative current which was measured at the drain, as electrons flow from the source to the drain. Thereby the drain would act as the electron collector and the source as the hole collector. For positive biases, the opposite is true.
For SPCM measurements, the recorded voltage was sent from the MFLI to the AFM controller, in order to be mapped to the position of the laser.

4.5 Optical Setup

A sketch of the optical setup and beam path, which was built by my colleague Nicklas Giese, used for optical excitation and measurements is shown in the appendix figure B.1.
For optical excitation (Laser 1) first, a 488 nm or a 440 nm diode laser was used. The laser was spatially filtered and guided through a series of neutral-density (ND), laser-line (LL) and band-pass (BP) filters corresponding to the respective laser. Afterwards the laser was passed through a beam splitter, where 92 % of the light was transmitted to a power meter (PM) and 8 % was reflected onto a mirror scanner. A telecentric lens system then guided the light to the objective in the inverted optical microscope, which focused the light on the sample surface. Both an air objective and an oil objective were used.
A second laser (Laser 2) along with filtering was installed in the setup as well. It was directed onto the sample behind the mirror scanner, to be used as static illumination while the other laser could be moved around.
Being used as a confocal microscope, the reflected and emitted light from the sample was collected by the objective back through the mirror scanner and again passing the beam splitter. The transmitted 92 % of the light was guided to flipable mirror which could reflect the light into a spectrometer, or passing the light to another beam splitter. The 8 % of the light reflected by the beam splitter was passed through ND filters onto an avalanche photodiode (APD) (APD 1). The transmitted 92 % of the light was passed to a long-pass (LP) filter, which only passed light red shifted from the laser wavelength onto an APD (APD 2), detecting the PL.

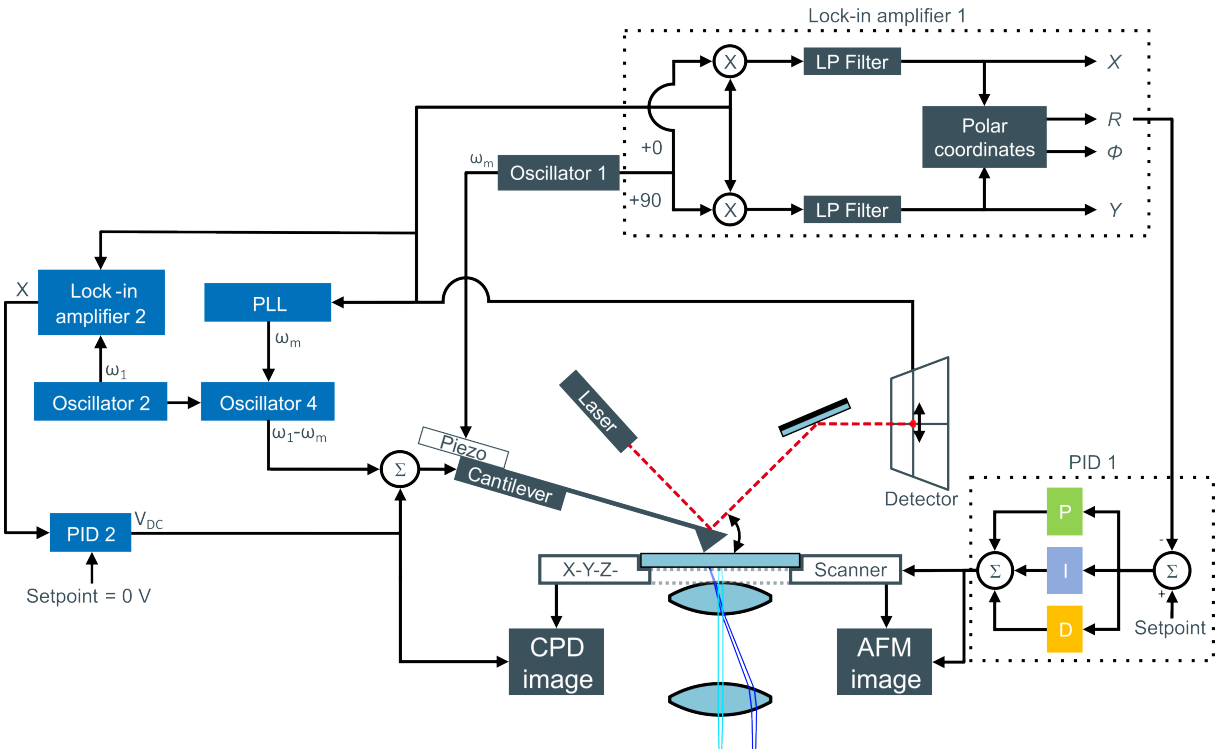

Figure 4.4: Sketch of the AFM and KPFM setup with the HF2LI lock-in amplifier components in blue, and the AFM controller components in dark blue. Here, the tip-sample distance is controlled at the sample, which is possible, but in practice, the tip height is varied.

The signals from the APDs were sent both to the ADwin-gold (goldbox) to be used in the self made laser-scanning software and the photon counting module of the AFM controller. The AFM controller would create maps of the number of photons counted for each position during an AFM measurement.
The whole beam path was enclosed in a lightproof box with one opening to the AFM environmental chamber on an optical table.

4.6 Atomic and Kelvin Probe Force Microscopy Setup

All KPFM measurements in this work were performed in heterodyne mode. This was realized by combining the AFM controller with an HF2LI digital lock-in amplifier. The latter includes 2 signal inputs and outputs, 8 demodulators, 6 digital oscillators, 4 PID controllers and 2 PLLs.
Figure 4.4 shows a sketch of the signal paths for AFM and H KPFM. A more detailed version may be found in the appendix figure B.2. The photodetector signal from the AFM controller was sent to the input of the lock-in amplifier. A PLL, containing an oscillator (3) and a PID controller detected the mechanical oscillation ω_m of the cantilever during AFM measurements in tapping mode. This value was subtracted from the second eigenmode ω_1, provided by oscillator 2 and used as the electrical excitation frequency ω_E at 2 V at the cantilever.

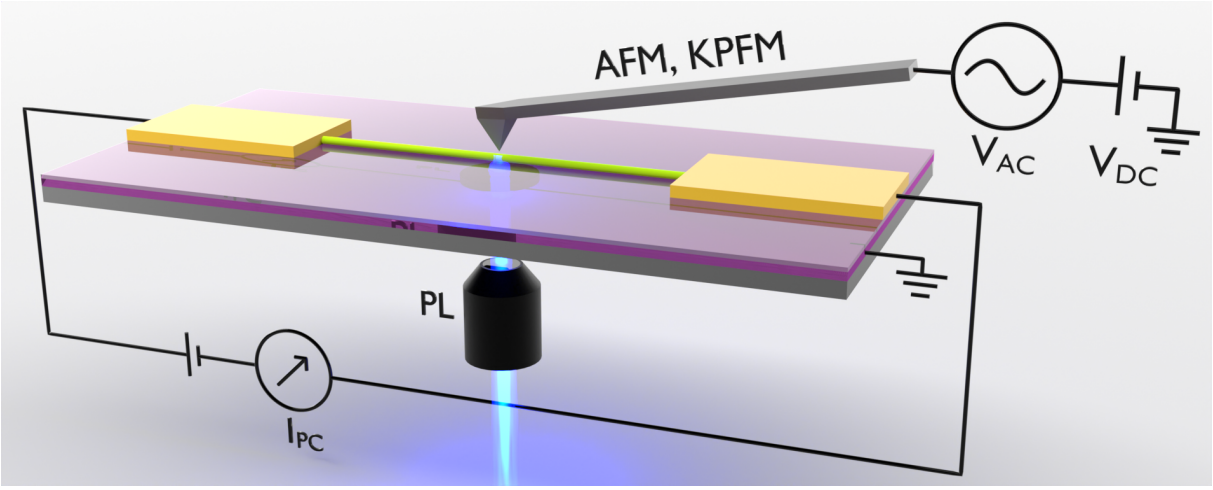

Figure 4.5: Setup for simultaneous current, optical and surface potential measurements. Here, the substrate is a transparent layering of glass (bottom gray), grounded ITO (middle purple) and SiO_2 (top gray). On it, golden electrodes contact a nanowire. The electrodes are connected to a current measuring setup. The tip from above is aligned to the laser spot from below.

Oscillator 2 also provided the reference signal for the lock-in amplifier to demodulate the photodetector signal at the second eigenmode. The phase shift between the electrical excitation and measurement was chosen so that the imaginary part of the signal Y was always zero. Thereby, demodulation of the real component X by the lock-in amplifier yielded the amplitude of the vibration at the second eigenmode. The X component was used instead of the amplitude R, because the X component changes linearly with the applied constant bias and can become negative, as is required by the PID controller, which is not the case for R.
This X component was used as the input signal for a PID controller whose setpoint was set to 0 V. The controlling output of this controller was both used as the constant bias V_{DC} at the cantilever and also sent to the AFM controller to be mapped out as the surface potential along the topography.
An illustration of the setup for simultaneous current, optical and surface potential measurementsis shown in figure 4.5. Samples without electrical contacts were grounded by the second output of the HF2LI lock-in amplifier. As the bias for KPFM measurements was controlled at the cantilever, an increase in the measured value V_{DC} can be interpreted either as a lower work function, a decrease in negative charge carriers, an increase in positive charge carriers, or more generally a higher surface potential. The accurate interpretation depends on the exact experimental circumstances.
The inverted optical microscope on which the tip-assisted optics (TAO) stage of the AFM setup was mounted was encased in a self made acoustically insulated metal box, called environmental chamber, with an opening to the optical setup on the same optical table.
The combination of optical excitation, KPFM and SPCM measurements as shown in fig-

ure 4.5 can be categorized as two different operation modes. In a simple variant, the sample could be illuminated locally in one spot during a KPFM measurement. This is called locally-illuminated (LI) KPFM and was done in order to investigate the charge-carrier separation during local illumination, and its effects on a semiconductor.
Alternatively, the laser could be aligned to the probing tip. Thereby, every position of a KPFM measurement was the illuminated position at the time of measurement. This is called laser-aligned (LA) KPFM. Alignment was achieved by keeping the AFM tip in one position while scanning the laser and recording the reflection. The laser was then positioned at the point of the reflection of the AFM tip apex. For subsequent measurements, instead of moving the tip and laser together, the sample was moved between them, using the TAO stage. Thereby, their position remained aligned. This was used for combined SPCM and KPFM measurements. In this mode, information about the topography, current flow, surface potential, laser reflection and photoluminescence were recorded simultaneously by the AFM controller.

5 Results and Discussion

In this chapter the experimental results will be presented and discussed. Firstly, some general experiments regarding the setup itself will be discussed. Then, experiments on different nanowire devices will be presented, with a focus on an ohmic device. Lastly, preliminary studies on nanosheets will be presented, including experiments on framed nanosheets, contacted nanosheets and nanosheets decorated with AuNPs.

5.1 Water Adsorption

Prior to this work, KPFM methods were already developed and implemented into the optical setup, though combined optical and surface-potential experiments were not yet performed. It was found that KPFM surface-potential maps tended to show varying results each day, especially changing with the seasons, as the relative humidity in the laboratory had a profound impact on the results of surface measurements. The effect of the relative humidity on work function measurements was discussed in section 2.3. Experiments which focused more on the measuring method, than the results themselves, did not need low humidity, and key measurements could be performed on days with low relative humidity.
Yet, this important parameter had to be brought under control, to obtain reliable data. As outlined in chapter 4, the measurement setup is encased in a self-made acoustically insulated metal box, mounted onto an optical table. The perforation of the table itself, as well as openings for the laser in-and output, and cables meant that it was not possible to completely seal the box airtight, in order to control the inner atmosphere.
To control the relative humidity inside the box, a dehumidifier was installed. It circulates air within the box through a layer of silica gel, which in turn is continuously dried by an additional current of warm air. Since the dried air circulates through the box, back into the dehumidifier at large volume flows, low relative humidities down to 2 % could be achieved. One major drawback however is that the vibrations of the dehumidifier may be picked up by the AFM tip, creating high noise levels, so the dehumidifier was only run between experiments.
Figure 5.1a shows the relative humidity inside the box over time during dehumidification. The humidity inside the measuring chamber decays exponentially during the drying process. Figure 5.1b shows how without any active drying, the humidity increases slower than it has decreased during the drying process, as the time between 20 %RH (blue line) and 30 %RH (red line) without drying is longer than the time between 30 %RH and 20 %RH with drying.
These curves show that in order to dry the box from 50 %RH down to an acceptable level of 20 %RH, the dehumidifier has to run for about 40 minutes, while afterwards it takes up to

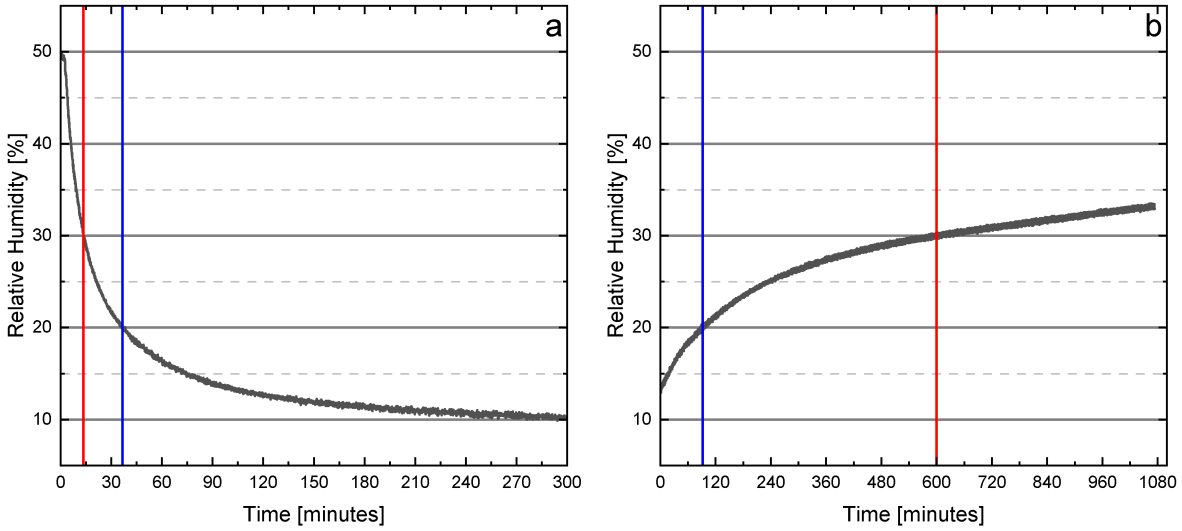

Figure 5.1: a) Relative humidity over time during operation of the dehumidifier. b) Relative humidity over time after operation of the dehumidifier. The time at which 30 %RH(20 %RH) is reached is indicated by the red(blue) lines.

8 hours to reach the upper limit of 30 %RH without dehumidification. Though this assumes that the box is not opened at any time, it goes to show that measurements in relatively dry air are possible using this setup.

Especially KPFM measurements with biases applied to metal contacts, and measurement with long measuring times are affected by water adsorption. KPFM images of a CdS nanowire contacted by a biased platinum contact on one side are shown in figure 5.2. Since AFM and therefore KPFM maps are scanned line by line from the bottom to the top, each scan has a fast (x) and slow (y) axis. The KPFM images in figure 5.2 were scanned at 0.5 lines per second with 300 lines on the slow axis, whereby each image took 10 minutes to record. The false color scale for these specific experiments was chosen to clearly show the points at which the substrate's surface potential was measured as 0.7 V and 1.4 V, to highlight the surface-potential change over time. Figure 5.2a shows that at 40 %RH with advancing measurement times, the surface potential of the substrate increases close to the biased platinum electrode. The nanowire appears to be charged positively as well. In figure 5.2b (15 %RH), the platinum electrode is biased positively as well, but the substrate and the nanowire do not show any change of the potential over the course of the measurement.

The charging over time at 40 %RH can be attributed to the water layer on the substrate facilitating charge transfers between the contact and the substrate's surface. In contrast, when the experiment is performed at a lower humidity of 15 %RH, as shown in figure 5.2b, no such charging can be observed. This goes hand in hand with the theory in section 2.3, where 40 %RH showed a considerable effect of the adsorbed water on the surface potential, while 15 %RH showed a reduced effect on the surface potential, even though 2 ML of water remained.

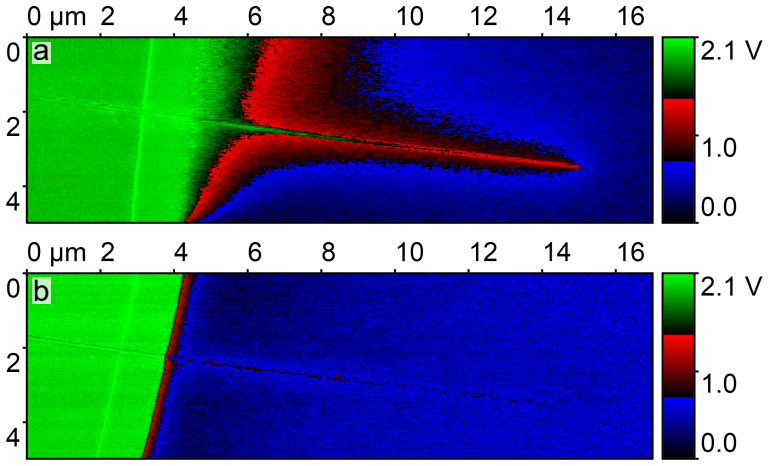

Figure 5.2: a) Surface-potential map of a CdS nanowire on SiO_2 contacted by platinum (left) which is biased at +2 V at 40 %RH. b) Surface-potential map of the same wire at 15 %RH. Each false color zone has a range of 0.7 V.

It has to be noted that in terms of the Schottky contact between the CdS nanowire and the platinum contact, a positive charging of the nanowire would have been expected for a positively biased contact in figure 5.2b. For this particular sample however there appears to be no charge transfer between the two, which further shows that the nanowire in figure 5.2a is charged through the water layer starting from the platinum contact.
Based on these experiments, from this point onward, all experiments were performed at 25 %RH or lower. For this, the chamber was either dehumidified before the experiments, or for experiments under oxygen exclusion, dry nitrogen was continuously flowed through the box.

5.2 The Internal Electric Fields of Nanowires with Ohmic Contacts *in Operando*

The results and discussions in sections 5.2.1-5.2.5 are part of a joint project with Daniel Lengle, Carlo Höhmann, Alf Mews and Tobias Kipp and will be found as well in our upcoming publication.[57]
When investigating charge-carrier separation and charge transport, model systems are very important starting points. Such systems should be consistently producible, from readily available materials. Ideally, the spatial dimensions of such a system should be well within the resolution of the experiments, to obtain unambiguous results. In this regard, investigating the charge-carrier transport through CdS nanowire devices is suitable, since these can be produced with different contacts on varying substrates and investigated both in terms of the electrical and also optical behavior. As previously discussed in section 3.3.2, Gu *et al.* attempted to extract information about mobility-lifetimes products in CdS nanowires

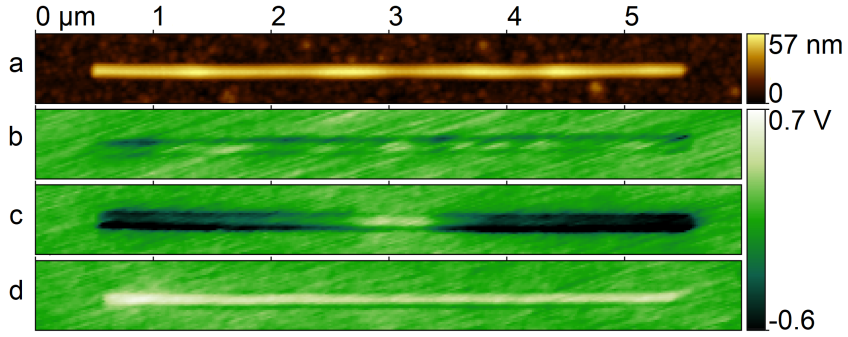

Figure 5.3: a) Topography image of an uncontacted CdS nanowire. b)-d) KPFM maps of the same wire b) without illumination, c) with local illumination at 3 µm (LI KPFM) and d) with the laser aligned to the KPFM probes position(LA KPFM).

solely from SPCM measurements.[49] Sources of error in this approach were identified by Graham *et al.*, as mobility-induced internal electric fields would alter the charge-carrier distribution.[50] Experimentally these fields were also observed by Schäfer *et al.* for CdSe nanowires.[25] This shows that more sophisticated approaches are necessary to consider such effects, in order to obtain more accurate results. Therefore, to further deepen the understanding of charge-carrier transport and separation in such devices, KPFM measurements were performed with and without illumination in combination with SPCM measurements.

In the following experiments, for the local illumination of nanowires, a laser with a wavelength of 488 nm was used at a power density at the sample of 12 W/cm^2 focused to a spot with a diameter of around 300 nm. The experiments were performed in an ambient atmosphere at 25 %RH.

5.2.1 Effect of Local Illumination

The original experiments probing the electric fields in illuminated nanowires by Schäfer *et al.* were performed on CdSe nanowires using EFM under local illumination on transparent substrates. In contrast to KPFM, in EFM the CPD is not being compensated during the measurement, so minor deviations of the work function were not taken into account.

In order to confirm similar behavior of CdS nanowires to CdSe nanowires, KPFM measurements of CdS nanowires were performed under local illumination on transparent substrates. The results of these measurements are shown in figure 5.3. The AFM scan in figure 5.3a shows the topography of the nanowire with diameter of 40 nm and a length of 5 µm, and the KPFM map in figure 5.3b shows the surface potential, which was recorded simultaneously, without illumination. Here, no significant changes of the surface potential across the nanowire were found and this measurement serves the purpose of a reference to other KPFM maps.

The surface potential shown in figure 5.3c measured by LI KPFM shows regions of positive

and negative surface potential, compared to the surface potential in the unilluminated case in figure 5.3b. The positive surface potential is found in the region where the nanowire was locally illuminated (at around 3 µm), while the negative surface potential is found in the unilluminated rest of the nanowire.

As mentioned in section 4.6, an increased surface potential in these experiments can be interpreted as an increased number of positive charge carriers or a decreased number of negative charge carriers, assuming that the work function itself remains constant. Thereby, the positive and negative surface potentials in figure 5.3c can be explained analogous to the findings of Schäfer *et al.*, discussed in section 2.2.3. As the nanowire is locally illuminated in the center, the excited charge carriers distribute themselves at first diffusively along the nanowire based on their mobilities. Since the mobility of the electrons is higher than that of the holes, the electrons distribute themselves along the whole wire, while the holes largely remain at the point of illumination. This leads to an excess hole concentration (EHC) at the point of illumination, observed as a positive charge, and a negative charging of the rest of the nanowire. The potential difference across the nanowire creates an internal electric field, which in turn causes a drift of the charge carriers, as a direct consequence of the diffusion of the charge carriers. The concurrence of the two transport mechanism means that they often cannot be clearly differentiated. As such, this mechanism will be referred to as diffusion/-drift and the resulting electric field will be called the mobility-induced internal electric field.

Figure 5.3d shows the LA KPFM image of the nanowire, where the surface potential is constant across the whole wire, but more positively compared to figure 5.3b. The magnitude of the positive charge is similar to that of the positive maximum observed at the point of illumination in figure 5.3c. In LA KPFM experiments, the nanowire is always illuminated at the position of surface-potential measurement. Thereby, without any other external electric fields present, the surface potential here reflects the EHC at the point of illumination qualitatively for different illumination positions of the nanowire. As the surface potential in figure 5.3d is constant along the whole wire, this shows that the EHC remains constant, no matter the illumination position.

The AFM and KPFM experiments were also performed with a different CdS nanowire, which was contacted by indium electrodes to obtain ohmic contacts. The contacts were electrically connected to a circuit such that they served as source and drain electrodes. Figure 5.4a shows the topography of the nanowire with a diameter of about 30 nm that is electrically contacted by indium on the left ($x \leq 0.5\,\mu m$) and right ($x \geq 6.5\,\mu m$). Figure 5.4b shows the corresponding surface potential, which is similarly uniform as that of the uncontacted nanowire in figure 5.3b. Compared to figure 5.4b, the LI KPFM map in figure 5.4c shows a more positive potential at the point of illumination at around 3 µm to 4 µm, similar to the positive charge shown in figure 5.3c. In contrast to figure 5.3c however, here it can be observed that the unilluminated parts of the nanowire do not exhibit negative charging during

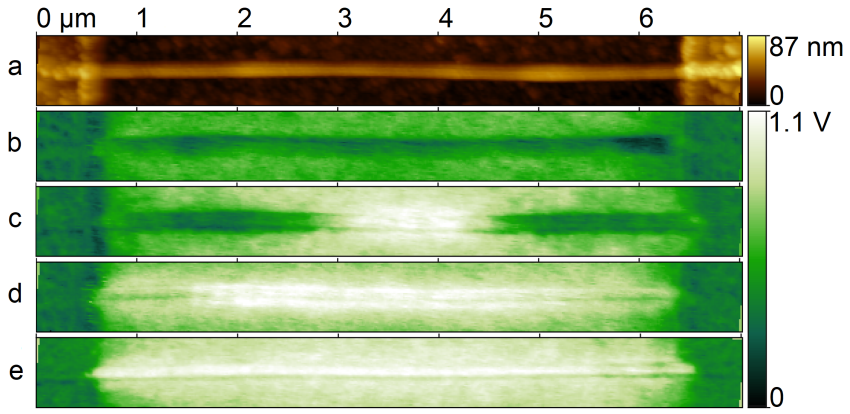

Figure 5.4: a) Topography image of a CdS nanowire with ohmic indium contacts. b)-e) KPFM maps of the same wire b) without illumination, c) with local illumination between 3 µm and 4 µm (LI KPFM), d) with the laser aligned to the KPFM probes position(LA KPFM) and e) under global illumination.

the illumination of the center.

The origin of the positive potential can again be understood through the concept of charge-carrier separation by diffusion/drift, which was explained previously. Additionally, as the unilluminated parts of the nanowire are not charged negatively, the total charge of the nanowire in figure 5.4c is more positive. During illumination, excited electrons seem to diffuse/drift into the electrical contacts, leaving behind the positive charge carriers.

Figure 5.4d shows the LA KPFM map of the same nanowire, where a generally increased surface potential, which drops in both contact regions, is observed. To reiterate, in LA KPFM, the respective position of the surface potential measurement is always locally illuminated, as the tip and the laser are aligned. Thereby, as no bias is applied, the surface potential here can be interpreted as the qualitative trend of an EHC, which can be explained by the diffusion/drift of charge carriers. When the local illumination is close enough to a contact, parts of the excited holes can diffuse/drift into the metallic contact. Thereby, the EHC is reduced, compared to regions where excited holes are not able to reach the contacts. The electrical currents caused by this charge-carrier movement will be addressed in section 5.2.2.

In addition to local illumination, the whole nanowire was also globally illuminated. For this, the laser was defocused until its spot on the sample was roughly around 6 µm. In order to maintain a comparable power density of 12 W/cm^2, the laser power at the sample was increased to from 8.7 nW to 3.5 µW. The resulting surface potential is shown in figure 5.4e, where it can be observed that the whole nanowire shows a more positive surface potential compared to figure 5.4b and no drop in the surface potential is present at the contacts, like in figure 5.4d.

The generally increased surface potential represents a positive charging of the nanowire. As the electrons have a higher mobility than the holes, it is likely that this charging is due to excited electrons flowing off into the contacts. An explanation for the lack of a surface po-

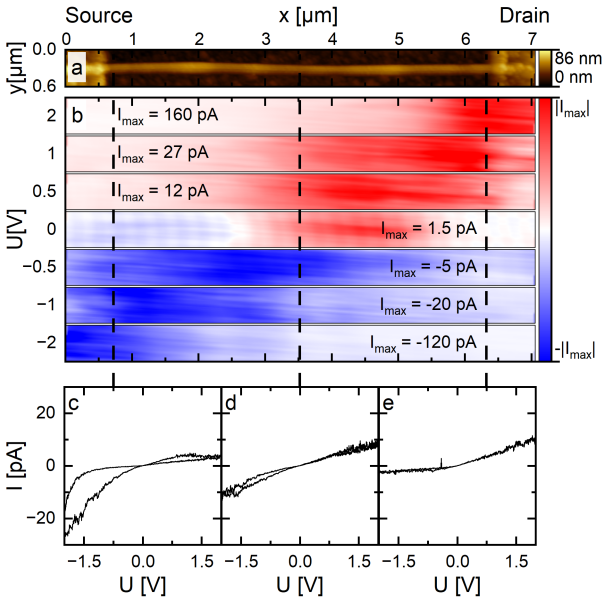

Figure 5.5: a) Topography of a CdS nanowire with ohmic indium contacts. b) SPCM maps of the same wire at different biases. c)-e) IV-curves recorded for different local illumination positions c) at the source contact, d) in the middle and e) at the drain contact, as indicated by the dashed lines in b).

tential drop close to the contacts may be found when considering that the whole nanowire is illuminated. As both contacts are illuminated simultaneously, no steady-state photocurrent in one direction can be formed, since the same number of excited holes move into both contacts equally. The thereby decreased number of excited holes at the contacts, would alter the potential in these regions, whereby the other excited holes in the rest of the nanowire would redistribute themselves in order to restore the dynamic equilibrium. The resulting even distribution of excited holes means that the increased surface potential is even across the wire as well.

Here, it was shown that CdS nanowires do exhibit mobility-induced charge-carrier separation upon local illumination, whereby electric fields are present inside the semiconductor. Furthermore, when the nanowire was integrated into a device, the EHC upon illumination was affected by the movement of charge carriers into the contacts. These internal electrical fields may impact current-voltage measurements of this device under illumination.

5.2.2 Scanning Photocurrent Microscopy

As discussed in section 3.3, in order to observe a steady-state photocurrent, the total charge of the nanowire needs to remain constant during the measurement. Therefore, for each hole moving into a contact, contributing to the photocurrent, an electron needs to move into the other. Thus, the photocurrent is limited by the charge-carrier type fewer of which reach their respective collecting electrode. This gives rise to specific characteristics in SPCM maps.

Figure 5.5 shows the topography and SPCM maps for different source-drain voltages, along with IV-curves for different illumination positions of the CdS nanowire with ohmic contacts. Without illumination, no measurable current was observed for biases between -2 V and +2 V. In figure 5.5a the topography of the nanowire, presented in the previous section (5.2.1), is shown as a reference for the SPCM measurements and IV-curves in figures 5.5b-e. Figure 5.5b shows the photocurrent during the SPCM measurements for different biases. In each SPCM map, a maximum of the absolute photocurrent can be observed. In the SPCM map for 0 V, a positive and a negative photocurrent maximum can be seen. The position of the absolute photocurrent maximum shifts towards the drain for positive biases and source for negative biases, and the absolute currents (red for positive and blue for negative biases) increase with increasing absolute biases.
According to the theory in section 3.3, the changing position of the photocurrent maximum for different biases originates in the electric field in the nanowire, which in turn is based on the ohmic nature of the contacts. Since the maximum absolute photocurrent position is always located closer to the hole collecting electrode (drain for positive biases), it can be deduced that the mobility of the holes is lower than that of the electrons, as the holes are narrowly distributed around the illumination position, analogous to the findings in the previous section.
The SPCM map for 0 V also shows a measurable negative and positive photocurrent. The photocurrent data is not centered relative to the nanowire, because the current measurements in the low-pA range introduce a time delay during the demodulation, shifting the map along the fast scanning x-axis, in this case to the left. As the SPCM maps shown here stem from LA KPFM measurements, the 0 V map shows the current recorded during the measurement of figure 5.4d. Thereby, the previously discussed decrease in EHC at the contacts in figure 5.4d, can be correlated to the current observed here. The excited holes flow into the electrode that is closer to the illumination, which then acts as the hole collector, decreasing the EHC while the current is increased.
Figures 5.5c-e show IV-curves, recorded for the different illumination positions as indicated by the dashed lines in figure 5.5b. While the IV-curve for center illumination (figure 5.5d) is linear, source (c) or drain (e) illumination changes the slope, depending on the sign of the bias. Qualitatively, this is to be expected, since the uncentered local illumination introduces an asymmetry into the otherwise symmetric device.
For source illumination at negative biases, or drain illumination at positive biases, generally larger currents can be observed than for the opposite cases. These larger currents occur when the direction of the external electric field accelerates the excited holes towards the closer electrode, while the electrons have to reach the farther electrode (electron limited current). In the opposite case, smaller currents are observed, as the excited holes are accelerated towards a farther electrode. The holes' mobility then limits the current flow (hole

limited current).
The hysteresis visible in figure 5.5c may be explained by impurities in the contact region. During the IV-measurement, trapped charge carriers might be depleted over time, contributing to the current. Once these charge carriers are reduced in number, the measured current therefore decreases for the remaining time of the measurement.
In general, the magnitudes of the currents in the IV-curves are lower than those observed in the SPCM maps in figure 5.5b for comparable biases. The explanation for this may be similar to the explanation of the hysteresis. It has to be taken into account that the duration of the illumination is longer during IV measurements, as compared to SPCM measurements. For IV measurements, the local region is illuminated for a few minutes. During SPCM measurements however, the laser is scanning the sample, and illuminates the contact region only for a few hundred milliseconds per line. This means that during IV measurements the aforementioned trapped charge carriers are in parts already depleted, before larger biases are applied during the measurement. In contrast, during SPCM measurements, the contact areas are only illuminated shortly, releasing trapped charge carriers to be directly measured as a current. Since for subsequently measured lines, the photocurrent maximum does not decrease in magnitude, it can be assumed that the freed trap states are refilled before the next illumination. Further discussion of the SPCM profiles will take place in section 5.2.4 along with discussions of LA KPFM measurements.

5.2.3 Locally-Illuminated Kelvin Probe Force Microscopy

As was shown in section 5.2.1, local illumination of CdS nanowires leads to a separation of the excited charge carriers, which in turn creates an internal electric field. To study the effects of the internal and external electric fields, LI KPFM measurements were performed and afterwards used for simulations. The results of the simulations which will be discussed in section 5.2.5.
Figure 5.6a shows a LI KPFM map with +2 V applied to the source contact, and a dashed red line as a visual guide of where the KPFM profiles in figures 5.6b and c were extracted. The LI KPFM profiles in figure 5.6b show differing progressions depending on the illumination. While the surface potential decreases linearly for no illumination, for source illumination a maximum at the source contact is visible, after which the potential again drops largely linearly, but less steep and remaining in general more positive, compared to no illumination. For drain illumination the surface potential drops linearly from the source electrode to a minimum at around 4-5 µm, followed by a local maximum at the drain contact. Figure 5.6c in general shows similar but inverted potential trends.
As was shown in section 3.3.2, when applying a bias across a nanowire device with ohmic contacts, the potential drops linearly over the nanowire. This linearity is reflected in the surface-potential profiles for no illumination in figures 5.6b and c and corresponds to a con-

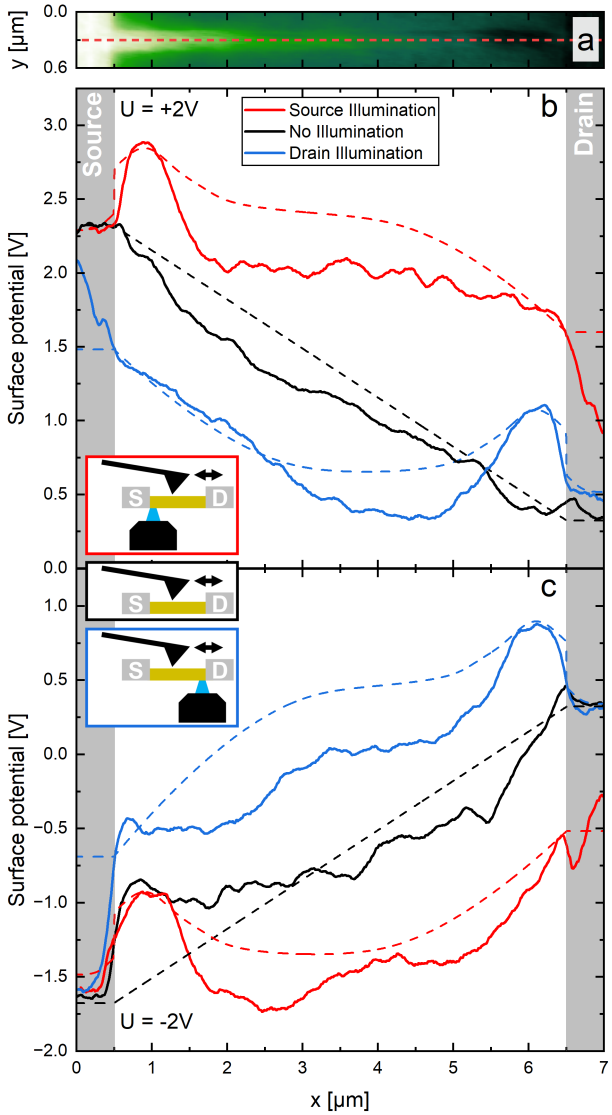

Figure 5.6: a) LI KPFM map of a CdS nanowire with ohmic indium contacts with external bias. The dashed red line indicates where the LI KPFM profiles were extracted. b) Surface-potential profiles at +2 V external bias. c) Surface-potential profiles at -2 V external bias. The dashed lines in b) and c) show the respective simulation results.

stant electric field in the nanowire.

For KPFM experiments under local illumination, the distinct positive local maximum in each blue and red curve coincides with the position of the illumination, as the local EHC increases the surface potential, which is comparable to the findings in section 5.2.1.

The illumination of either contact leads to distinct surface-potential profiles. The deviations of the profiles go along with the findings in section 5.2.2, where the different charge-carrier mobilities lead to different currents depending on the illumination position. Figures 5.6b and c show that along with the hole- and electron-limited currents, also different surface potentials can be observed. When the point of illumination is close to the hole collector (drain for positive biases), the holes can directly flow into that contact, while the excited elec-

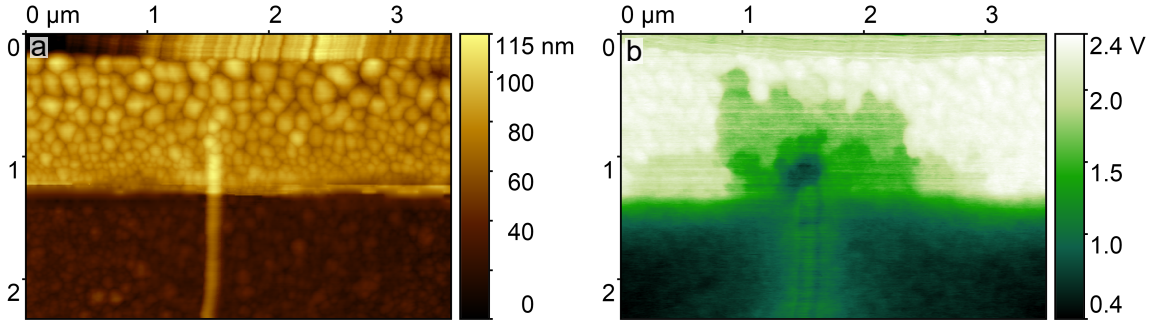

Figure 5.7: a) Topography image of one of the indium contacts (top half) with the nanowire (lower half). b) The surface-potential map measured simultaneously at a bias of +2 V under global illumination.

trons need to travel along the nanowire to the electron collector. This leads to an increased electron concentration along the nanowire, which is measured as the decreased surface potential for drain illumination (compared to no illumination) in figure 5.6b. *Vice versa*, with the illumination close to the electron collector (source for positive biases), the less mobile holes need to move to the farther electrode. The increase in hole concentration along the nanowire is measured as an increased surface potential (compared to no illumination) for source illumination in figure 5.6b. As the device is generally symmetric, the analogous interpretation holds true for negative applied biases shown in figure 5.6c.

The nonlinear behavior of the surface potential for any illumination shows that excited charge carriers experience a changing electric field and therefore drift on their way to their respective collecting electrode. This complicates calculations of their mobilities based on measured photocurrent profiles, as such calculations had previously considered only the constant external electric field. LA KPFM measurements were performed in an effort to evaluate the impact that these changing surface potentials have on SPCM measurements, as will be presented in section 5.2.4.

In figures 5.6b and c for some measurements, changes in the surface potential of the contacts themselves can be observed. Theses changes were especially pronounced when the currents were electron limited. AFM and KPFM measurements of one of the biased indium contacts were done to investigate the surface potential differences of the contacts. In the AFM data in figure 5.7a in the upper half of the image, multiple droplets of indium can be observed. The uppermost region of the topography map shows artifacts resulting from interactions of the tip with the high gold contact in this region, which was deposited on top of the indium to promote efficient biasing of the indium. Figure 5.7b shows the surface potential of the contact and the wire at a bias of +2 V under global illumination, revealing potential steps between the indium droplets towards the wire.

The indium droplets apparently have significant resistances between each other, limiting current flow between the nanowire and the gold. As a result of the intra-material resistance,

the actual potential that reaches the nanowire is lower than the applied bias. While this effect does not adversely affect the findings in this section, the actual potential at the nanowire is essential when modeling the system for simulations.

5.2.4 Laser-Aligned Kelvin Probe Force Microscopy

In order to combine SPCM with KPFM data, laser-aligned KPFM was developed in this work. The tip and the laser are aligned to each other and the sample is moved between them, while at the same time biases can be applied to the sample. This technique can yield simultaneous information about the topography, the evolution of the surface potential at the point of illumination, as well as the resulting photocurrent, photoluminescence, and the reflection of the laser. The spatial resolution of the reflection is increased to the diameter of the KPFM tip, since its reflection amplifies the signal further. Therefore this setup could also be used for apertureless scanning near-field optical microscopy (SNOM).

The SPCM profiles shown in figure 5.8 were extracted from the already discussed SPCM maps (figure 5.5) and as such show the same photocurrent maxima for different biases. From these profiles, it can be determined that the exponential decay of the photocurrent profiles is not equal for different applied biases. Therefore no diffusion length for the holes can be calculated as was done by Gu *et al.* discussed in section 3.3.2.[49] The measurements here corroborate the calculations of Graham *et al.*, by showing that the internal electric fields discussed in sections 5.2.1 and 5.2.3 alter the drift of excited charge carriers, and thereby the photocurrent profiles.[50] As such, the photocurrent profiles cannot be analyzed solely based on the mobilities and the constant external electric field. Also the impact of the intra-material resistances of the indium contacts would need to be taken into account for such analysis.

The profiles shown in figure 5.9 were extracted from LA KPFM maps recorded simultaneously to the SPCM maps. Figure 5.9a shows the LA KPFM profiles, containing information about the local surface potential at the point of illumination. Compared to the SPCM data in figure 5.8, it is clear that an increasing absolute photocurrent towards the hole collector electrode, coincides with a decreasing local surface potential in figure 5.9a. Furthermore, a distinct change in the slope at $x \approx 2.5\,\mu m$ for positive biases ($x \approx 4.5\,\mu m$ for negative biases) can be observed. The decreasing surface potential towards the hole collector is due to the increasing number of holes reaching the hole collector, when the excitation point moves closer to that electrode and shows the major impact of the minority charge carriers on the photocurrent.

In an effort to clear up the LA KPFM profiles, in figure 5.9b the LA KPFM data was adjusted by the respective linear potential arising from the external electric field and offset by the applied bias. This data, qualitatively represents the EHC. For each applied bias, the EHC exhibits a maximum at a different position, and decreases linearly from there towards both contacts.

As the adjusted LA KPFM profiles are different for different applied biases, the external elec-

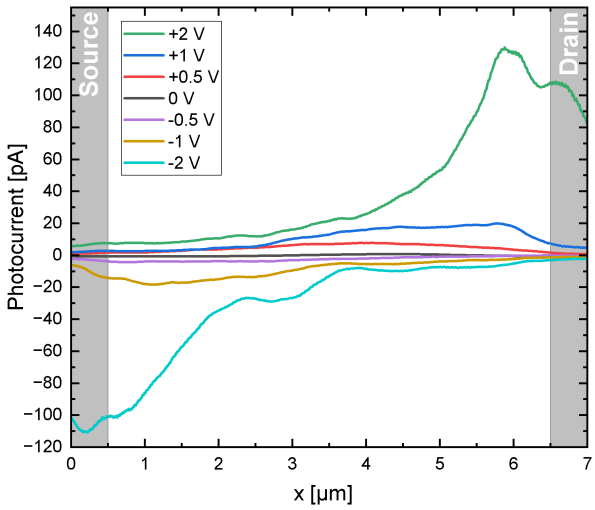

Figure 5.8: SPCM profiles of a CdS nanowire with ohmic indium contacts recorded simultaneously with LA KPFM profiles.

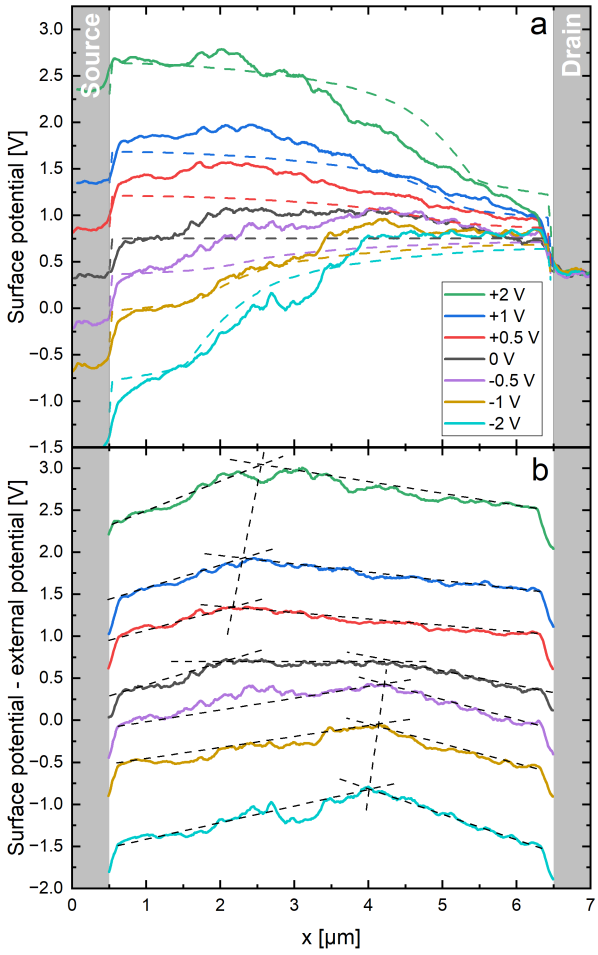

Figure 5.9: a) LA KPFM profiles of a CdS nanowire with ohmic indium contacts, where the dashed lines represent the simulations results. b) LA KPFM profiles adjusted for the external surface potential and offset by the applied bias, where the black dashed lines act as visual guides.

tric field must have an impact on the excited charge-carrier distribution and the resulting internal electric field. Therefore, the total electric field in this device exists as a superposition the external electric field and the internal electric field, induced by the charge-carrier mobility differences, in a dynamic equilibrium. As the actual charge-carrier mobilities of this system are unknown, iterative calculations need to be performed to gain access to the underlying charge-carrier distributions and dynamics and also material parameters such as the charge-carrier mobilities themselves.
Simulations by which such calculations are performed need input data to be fitted to. The KPFM maps presented so far are suitable for this purpose as these represent the local surface potential, the derivative of which is the electric field. The following section will therefore outline the simulation results, which were fitted to the data presented so far.

5.2.5 Simulation Results

All modeling and simulations were performed by Carlo Höhmann using the software COMSOL Multiphysics 6.3, and will be part of his thesis. Therefore, this section will only briefly discuss some of the simulation results to the extend of understanding the underlying reasons for the trends of the KPFM data.
Figure 5.10 shows the simulated LI KPFM data, fitted to the measured data, along with the simulated charge-carrier concentrations. For the positive bias in figure 5.10 with a) source and b) drain illumination, the charge-carrier concentrations show distinct trends, just like the surface-potential curves discussed previously. Based on the trends of the charge-carrier concentrations, both panels 5.10a and b are divided into three regions (**I** - **III**). In order to compare the similarities and differences between source and drain illumination, these regions will be discussed separately.
In region **I**, where the illumination takes place, it is observable that both source and drain illumination results in a peak of the surface potential as well as both charge-carrier concentrations. Even though the absolute electron concentration remains higher than that of the holes, when adjusting for the electron doping concentration of $4.8 \cdot 10^{12}$ electrons/cm^3, the concentration of excited holes in this region is actually higher than that of the excited electrons. The explanation of this is based on the different mobilities, as previously discussed in section 5.2.1.
In figure 5.10a, during source illumination the hole concentration remains elevated in the nanowire region **II** towards the drain (hole collector) electrode, while the electron concentration begins to decrease. This can be explained by the external electric field accelerating the electrons towards the source and the holes towards the drain electrode.
In region **III**, the electron concentration begins to reach its effective doping concentration, while the hole concentration is down to largely insignificant amounts. Here, the surface potential starts to become linear and dropping to the potential of the electrode, since in the

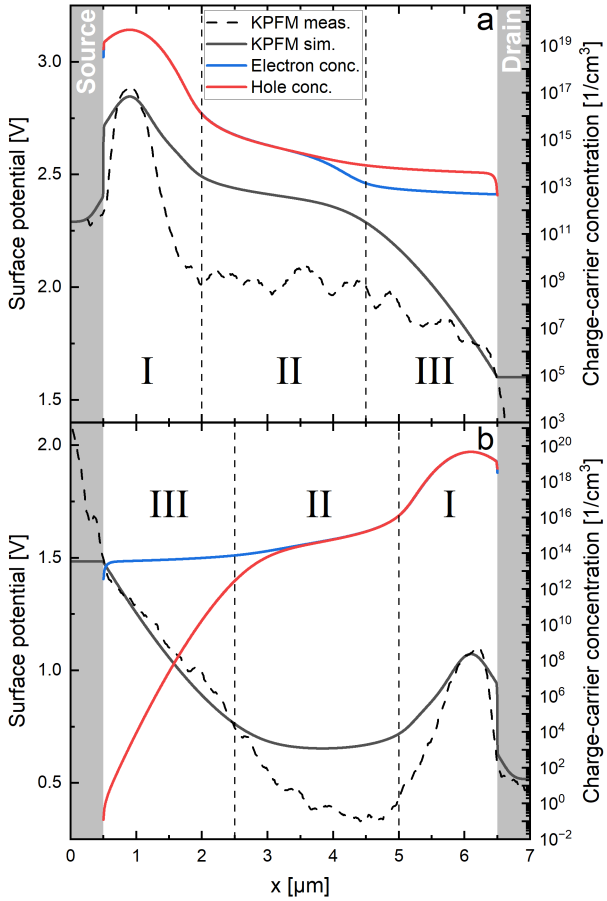

Figure 5.10: Simulated surface potential (black) and charge-carrier concentration (red and blue) profiles of an ohmically contacted CdS nanowire under local illumination and +2 V bias, along with the original measured LI KPFM profiles (dashed data). a) The wire is illuminated at the source. b) The wire is illuminated at the drain. The panels have been divided in three regions (**I** - **III**) based on the charge-carrier concentrations.

absence of sufficient amounts of excited charge carriers, the electric field becomes constant. For drain illumination in figure 5.10b, even though the surface-potential profiles appears to be quite different, compared to figure 5.10a, the profiles of the charge-carrier concentrations are comparable to source illumination, especially in region **I**. The major impact of the increased charge-carrier concentration directly at the point of illumination on the surface potential creates the local surface potential maximum, independently of source or drain illumination.

In region **II** for drain illumination, the general observation is inverted to the source illumination discussed above. Here, the electron concentration remains elevated, while the hole concentration begins to drop. This leads to a more negative surface potential compared to source illumination or no illumination (as shown in figure 5.6).

Lastly in region **III**, the electron concentration again reaches its effective doping concentration, while the hole concentration has dropped off to insignificant levels. Just as for source illumination, the absence of excited charge carriers leads to the constant electric field and

Table 5.1: Average charge-carrier lifetimes of the different regions of a CdS nanowire with ohmic indium contacts under local illumination at the source and the drain.

Region	Source illumination	Drain illumination
I	$8.6 \cdot 10^3\,\mu s$	$11 \cdot 10^3\,\mu s$
II	$9.1 \cdot 10^6\,\mu s$	$9.5 \cdot 10^6\,\mu s$
III	$67 \cdot 10^6\,\mu s$	$76 \cdot 10^6\,\mu s$

linear surface potential towards the electrode potential.

After using the charge-carrier concentrations to evaluate the surface-potential profiles, it becomes apparent that their courses from regions **I** to **III** are actually quite similar for both illumination positions, with a different total charge. It is mainly in region **III**, where the upwards or downwards trend of the surface potential towards the respective electrode is different for the two potential profiles. The similarities also become apparent when looking at the charge-carrier lifetimes in the different regions. These lifetimes give an average measure of how long a charge carrier stays excited before recombining. At the surface-potential maximum in region **I** for both source and drain illumination, the lifetime is determined to be 39 µs. This is within the range found in the literature for radiative recombination in CdS nanowires of 1.3 µs-394 µs, which fits with the fact that the simulation model used here only considers direct recombination and excludes non-radiative recombination pathways.[58] The average regional lifetimes for source and drain illumination are shown in table 5.1, with the general trend of increasing from the point of illumination in region **I** to region **III** for both source and drain illumination. The lifetimes for drain illumination are generally longer than for source illumination in the respective regions.

The trend of the lifetimes from region **I** to **III** can be explained by the decreasing amount of excited charge carriers from the point of illumination to the farther electrode. With fewer charge carriers available for recombination, the charge-carrier lifetimes increase significantly. Lifetimes in the range of seconds indicate that a charge carrier reaching these regions does not have a recombination partner and will most likely reach the respective collecting electrode to contribute to the current. The generally increased lifetimes for drain illumination in comparison to source illumination, can also be explained by the decreased hole concentration, as the holes drift towards the drain electrode, and are thereby not available for recombination at the source electrode. While the same argument could be made for the electrons during source illumination, the n-type doping leads to electrons still being available for recombination, which leads to shorter lifetimes, limited by the availability of excited holes for recombination.

Lastly, the charge-carrier mobilities used for these simulation were $37\,\frac{cm^2}{Vs}$ for electrons and $9 \cdot 10^{-9}\,\frac{cm^2}{Vs}$ for holes. These values were obtained by iterative fitting of the simulations to the measured data. The initial values for these fits were $6 \cdot 10^{-3}\,\frac{cm^2}{Vs}$ for electrons and $4 \cdot 10^{-6}\,\frac{cm^2}{Vs}$

for holes. The electrons initial value was chosen based on results from Daniel Lengle, and the holes initial value was chosen based on works by Utterback *et al.*.[53,59,60] Further details on the fitting procedures and reasoning for these values will be found in our upcoming publication.[57]

5.2.6 Effect of the Probing Tip

Up to this point, a possible effect of the KPFM measuring tip on the SPCM measurements, was not taken into account. Since in KPFM, the potential differences between the tip and the sample are nullified, it can be reasonably assumed that charge carriers are not affected by the tip's work function. However, it was found that the short-circuit current (I_{SC}) for no bias could not be measured when SPCM measurements were performed independently from LA KPFM measurements.

To study this, SPCM measurements without bias were repeated with tip-laser alignment but without a constant external bias being applied to the tip. When a 500 kHz, 2 V AC voltage was applied to the tip, even without the DC nullifying potential needed for KPFM, a current was measured. This experiment was repeated in AFM tapping mode, and for different hover mode lift heights keeping a constant tip-sample distance and different AC frequencies.

Figure 5.11a shows the topography as a reference for the SPCM maps for different tip-sample distances in figure 5.11b. These show the I_{SC} with a positive and a negative current maximum, which was previously discussed in section 5.2.2 with the tip present. The absolute currents decrease for larger tip-sample distances, but are still measurable for a distance of 100 nm and even up to 500 nm, which shows that the I_{SC} of up to 1.5 pA is induced by the tip. It can be ruled out that charge carriers are transferred from the tip to the sample to contribute to the current, because the distances are too large. Instead, the AC electric field from the tip must be responsible for the charge-carrier separation.

Figure 5.12a shows the topography as a reference for the SPCM maps for different frequencies applied to the tip during tapping mode in figure 5.12b, where it is observed that the

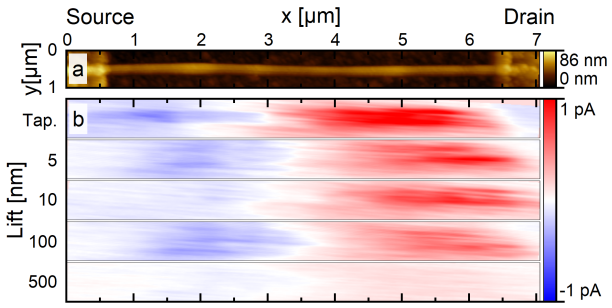

Figure 5.11: a) Topography image of a CdS nanowire with ohmic indium contacts. b) SPCM maps of the same wire recorded with the tip and laser aligned, with a 500 kHz, 2 V AC voltage applied to the tip, in tapping mode and different lift heights.

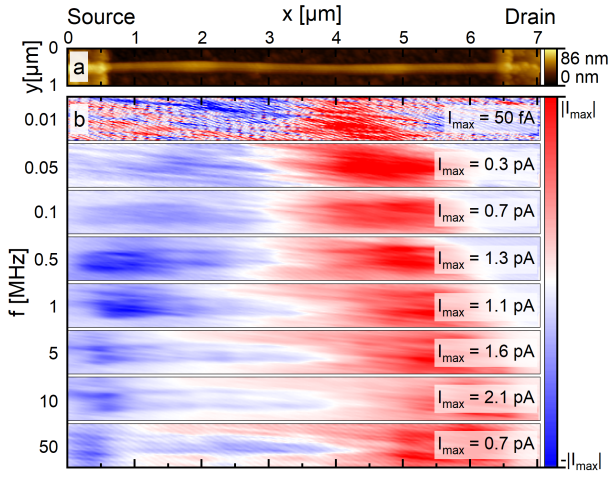

Figure 5.12: a) Topography image of a CdS nanowire with ohmic indium contacts. b) SPCM maps of the same wire recorded with the tip and laser aligned in tapping mode, with a 2 V AC voltage applied to the tip at different frequencies.

photocurrent maxima shift towards the respective closer contact for increasing frequencies applied to the tip.

These shifts further hint towards a drift of the excited charge carriers, facilitated by the alternating electric field of the KPFM tip. Apparently, for higher frequencies, the distribution of the excited holes is narrower than for lower frequencies, whereby only holes which are excited closer to a contact, can reach the contact in order to contribute to the current. This may be explained by the fact that for lower frequencies, the holes drift in each direction for a longer time, before the electric fields switches direction again.

The observed current magnitudes never surpass 2.1 pA and seem to be independent of the applied frequency, with the exception for when the positive and negative maxima move

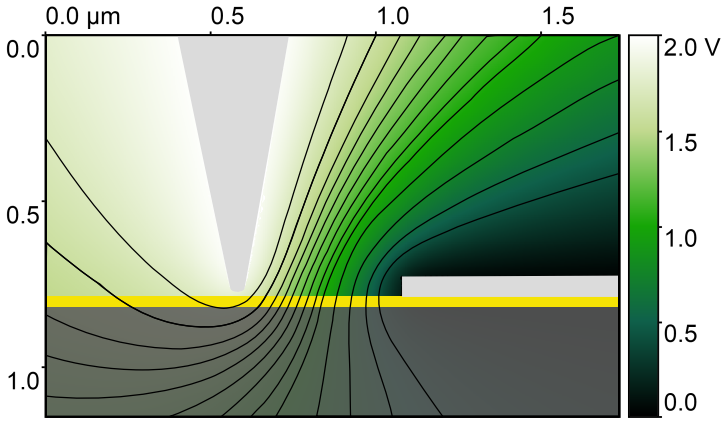

Figure 5.13: Results from simulations of the potential between the tip biased at +2 V and the sample, as a cross section. The substrate's SiO_2 layer is indicated in the lower part of the image in dark gray with the yellow CdS nanowire on top. On top of this to the right, the grounded electrode is indicated in light gray, while the light gray cone to the left indicates the position of the probing tip. The black lines represent contour lines.

closer at lower frequencies, where their currents begin to cancel each other out. To further corroborate this theory, the electric field between a tip with a constant bias of +2 V over a nanowire in the vicinity of a grounded contact was simulated by Carlo Höhmann.
Figure 5.13 shows the simulated potential between the tip and the nanowire device. The probing tip (light gray) is biased at +2 V and is positioned above the nanowire (yellow). To the right, on top of the nanowire the grounded electrode is indicated in light gray. It can be seen that with the tip above the nanowire, the potential contour lines permeate the nanowire perpendicular, which represents a potential change along the nanowire towards the electrode on the right. This potential change corresponds to an electric field between the tip and the electrode inside the nanowire, which separates excited charge carriers.
These findings show that an effect of the probing tip on the photocurrent exists during LA KPFM measurements. Based on the limited current magnitude which is induced in the low pA-range, the findings and interpretations in the previous sections however still hold true.

5.3 CdS Nanowires with Different Contacts

To study the effects that Schottky contacts have on the device properties, CdS nanowires were contacted with Schottky contacts on both sides (Schottky device). Furthermore, a sample was produced, where each nanowire has one Schottky contact on one side and one ohmic contact on the other side, with the aim to create diode devices. In the following sections, experiments on Schottky and diode devices will be presented, with the findings of the previous section in mind.

5.3.1 Schottky Contacts

To form a Schottky contact, the electrode material needs to have a higher work function than the CdS nanowire, which is about 5 eV.[29] As such, platinum with a high work function of 5.6 eV was chosen as the contact material.[61] The characterization of these devices posed unique challenges for the measurements, as not only generally lower currents were observed compared to the devices with ohmic contacts, but the stability was worse. This expresses itself in higher current noise levels, as well as a higher possibility of a fracture of the nanowire occurring, breaking the circuit. Therefore, not all measurements presented for the Schottky devices stem from the same device.
In the experiments on Schottky devices, for the local illumination of the nanowires, the laser with a wavelength of 440 nm was used at a power density at the sample of 12 W/cm^2. The experiments were performed in an ambient atmosphere at 15 %RH.
Figure 5.14 shows IV-curves of a Schottky device with and without global illumination, which in this case was achieved by a LED lamp attached to the AFM head. From the IV-curves it is clear that without illumination, no current can be measured, and only with illumination a

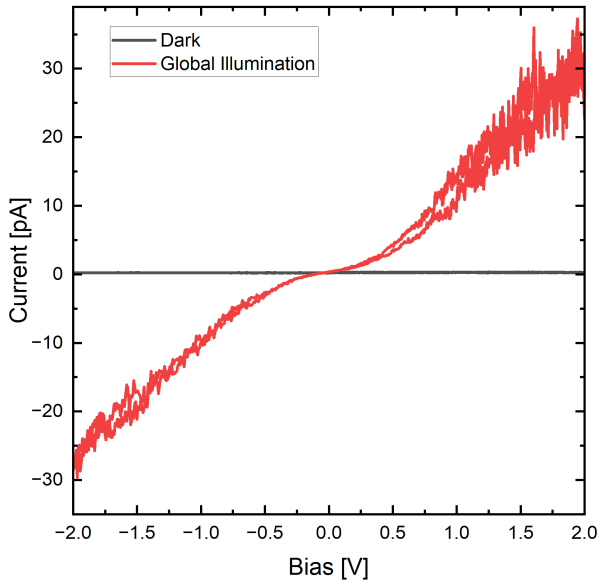

Figure 5.14: IV-curves of a nanowire with Schottky contacts, with and without global illumination.

current is observed, which shows the IV-characteristics of two back-to-back Schottky contacts.

Additionally, SPCM maps were recorded. Figure 5.15a shows the topography of the Schottky device, with the platinum contacts on the left ($x \leq 1.5\,\mu m$) and right ($x \geq 8\,\mu m$) of the CdS nanowire. The topography serves as a reference for the SPCM maps in figure 5.15b. These maps show a symmetric photocurrent response for positive and negative biases. For absolute biases larger than 3 V, the SPCM maps show localized photocurrent maxima at the drain for positive biases and at the source for negative biases. For absolute biases below 3 V, the photocurrent maxima broaden and move closer to the nanowire's middle. In general, for decreasing applied absolute biases the absolute current decreases as well. For no applied bias, no photocurrent is observed.

The localized photocurrent maxima, for absolute biases larger than 3 V, are in accordance with the theory for Schottky contacts discussed in section 3.3.1. Here, excited charge carriers are separated in the SCRs of the reverse biased Schottky contacts, where the electric field is increased by the applied bias. However, the broadening and centering of the photocurrent maxima for lower biases is not expected, based on the basic Schottky contact theory, since the region outside the SCRs should not be affected by externally applied electric fields, which would lead to charge-carrier drift.

The observed behavior for absolute biases below 3 V is much akin to the SPCM behavior of devices with ohmic contacts. In section 5.2.2, this behavior was attributed to the superposition of both external and internal electric fields and charge-carrier diffusion. In the case presented here, the external electric fields cannot be considered for charge-carrier separation in the middle of the nanowire, due to the Schottky barriers on both sides of the wire. As ex-

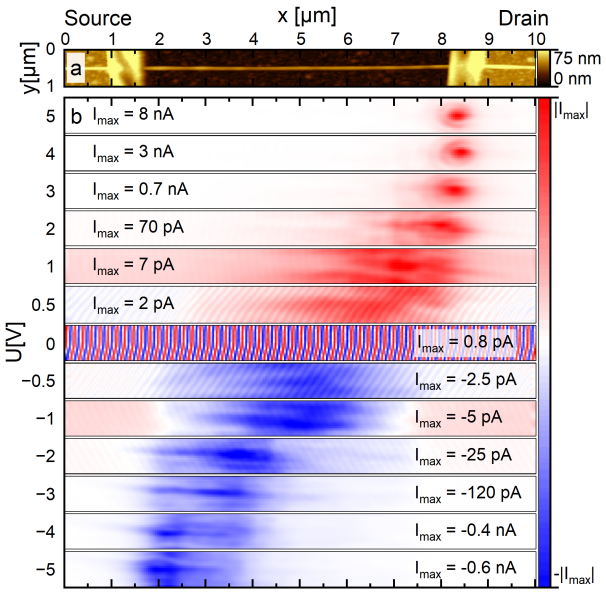

Figure 5.15: A CdS nanowire with platinum Schottky contacts with a) topography and b) SPCM maps at different biases.

plained in section 3.3.1, external electric fields in these devices are confined to the SCR at the respective reverse biased Schottky contact. Therefore an explanation has to revolve around the diffusion of excited charge-carriers towards the Schottky barriers and their subsequent drift inside the SCRs. It is important to repeat that in order to contribute to a steady-state photocurrent, each hole reaching one contact needs an electron to reach the other contact.

Figure 5.16 shows schematic band diagrams for different biases, illumination positions and if the excited charge-carriers reach their respective collecting electrode, based on the SPCM measurements. Only when both charge-carrier types reach their respective collecting electrode, a current is measured.

Figures 5.16b and d illustrate, how no photocurrent is observed for low absolute biases (<3 V) with the illumination close to the hole collector (drain for positive biases). When excited in this region, only the holes reach their collecting electrode and not the electrons. In the SCR, electric fields are present even without biases being applied. These fields would accelerate the holes to the closer electrode (drain) and electrons to the farther electrode (source). Due to the proximity of the excitation to the hole collector (drain), the current limitation must be due to the electrons not reaching the electron collector (source) on the other side of the nanowire.

From the previous study in section 5.2, it is clear that excited electrons are distributed wider than the holes. Still in figures 5.16b and d, the Schottky barrier at the electron collector seems to limit current flow. In general, this Schottky contact is forward biased with regard to this electron flow. Yet, a barrier exists for the flow of electrons in the conduction band, possibly due to the upward band bending. For low applied absolute biases (≤3 V) this barrier appar-

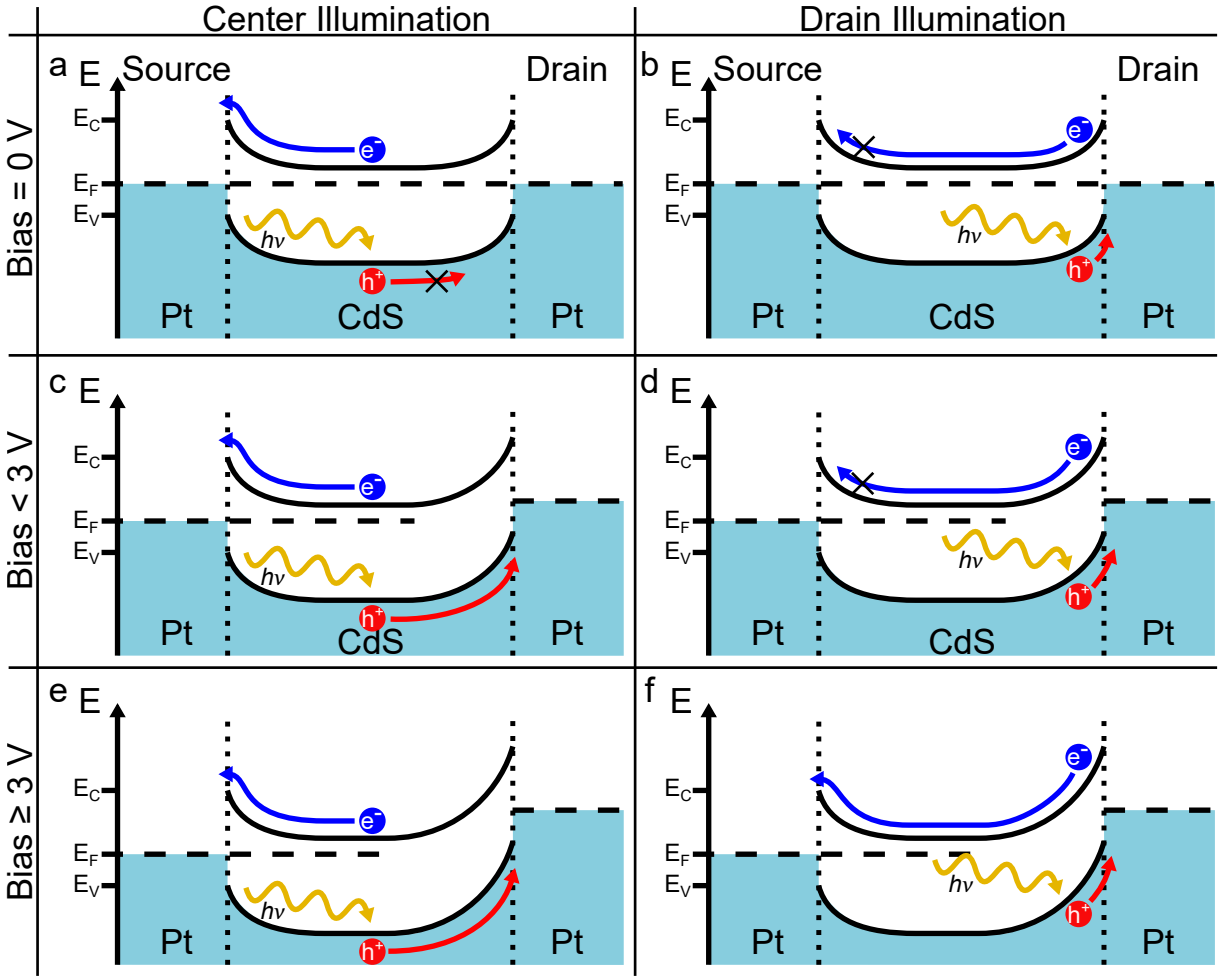

Figure 5.16: Exemplary band structures of a CdS nanowire with platinum Schottky contacts under illumination with applied biases. Here, the drain acts as the hole collector and the source acts as the electron collector. a) No bias is applied to the source and the center is illuminated. b) No bias is applied to the source and the drain is illuminated. c) Biases below 3 V are applied to the source and the center is illuminated. d) Biases below 3 V are applied to the source and the drain is illuminated. e) Biases equal or above 3 V are applied to the source and the center is illuminated. f) Biases equal or above 3 V are applied to the source and the drain is illuminated. The blue and red arrows indicate the path of the respective charge carriers to their respective collecting electrode. If a charge carrier is not able to reach its electrode, this is indicated by the black cross.

ently cannot be overcome by electrons excited into the conduction band in the SCR of the other contact (hole collector).

As shown in figure 5.16f, when the potential difference of the hole collector SCR is increased by the application of larger absolute biases, electrons excited in this region are at a higher energy as well. This might be the reason why for larger absolute biases (≥3 V), electrons do reach and overcome the barrier at the electron collector. Thereby a steady-state photocurrent is measured with SPCM behavior akin to a Schottky device with localized photocurrent maxima at the contacts, only for absolute biases above 3 V, as shown in figure 5.15b.

For low absolute biases, photocurrents are observed in the middle of the nanowire, as shown in figure 5.15b. Figure 5.16c and e illustrate how excited charge carriers reach the SCRs of their respective collecting electrode. As the excitation takes place outside the SCRs, the charge carriers only move diffusively and by the mobility-induced internal electric field (as discussed in section 5.2.1), whereby the photocurrents can be described as diffusion dominated. The photocurrent maxima are still closer to the hole collector, as the holes have a lower mobility than the electrons. Excited holes, which reach the SCRs of their respective collecting electrode are accelerated by the electric field into the contact to contribute to the current.
Lastly, it is observed that even this diffusion dominated photocurrent of excited charge carriers in the middle of the nanowire increases for larger applied external biases. As the diffusion should not be affected by external electric fields, this must be explained by the increasing electric field inside the SCR of the reverse biased electrode. This increases hole drift in this area and therefore the current, which remains limited by the amount of charge carriers reaching the SCR. Figure 5.16a thus illustrates that without an applied bias, no excited holes reach the SCR, whereby no current is measured.
These experiments show that the diffusion/drift of charge carriers in the semiconductor outside of the SCRs of Schottky devices can play a significant role in the current flow. Also, a forward biased, sufficiently large, Schottky barrier can limit current flow for low applied biases. To conclusively prove these explanations, extensive studies and simulations would be necessary, similar to those performed for the CdS device with ohmic contacts.

5.3.2 Diode Devices

The devices presented up to this point were fabricated with symmetric contacts of the same metal. Thereby the devices' behaviors were nearly symmetric as well. Similar currents for positive and negative biases were measured, with the sign inverted.
To probe the behaviors of asymmetric contacted nanowires, a device with mixed contacts was fabricated. The experiments in sections 5.2 and 5.3.1 were important verify the materials that would reliably form ohmic or Schottky contacts. For the Schottky contact, the barrier created by platinum electrodes was deemed too large, based the experiments in section 5.3.1. Therefore, gold was chosen because of its lower work function of 5.3 eV.[61] For the ohmic contact, indium was chosen.
In the experiments on diode devices, for the local illumination of nanowires a laser with a wavelength of 440 nm was used at a power density at the sample of 24 W/cm^2. The experiments were performed in a nitrogen atmosphere (oxygen below 5 %) at 20 %RH.
SPCM maps of a diode device, with a gold source and indium drain, are shown in figure 5.17. It should be noted that a problem with the source contact was identified, as for each applied volt of bias at the current source, the source contact's potential was found increase by only

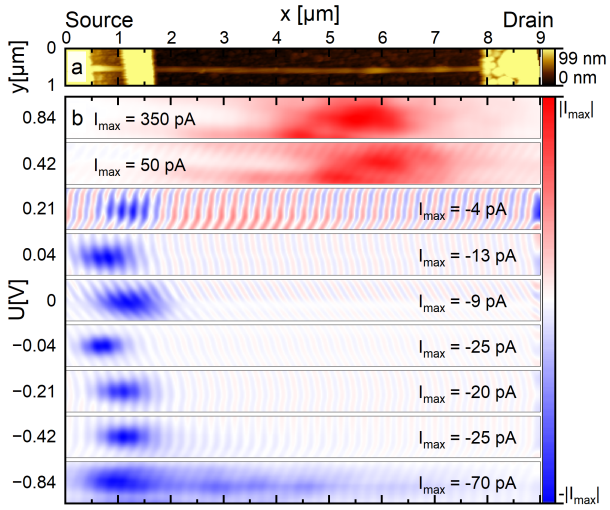

Figure 5.17: a) Topography image of a CdS nanowire with a Schottky gold source contact and an ohmic indium drain contact. b) SPCM maps at different biases of the same nanowire device.

0.42 V. Thereby, the biases indicated in the following data are in general lower than in the previous experiments.

Figure 5.17a shows the topography of the diode device, with the Schottky gold source contact on the left ($x \leq 1.5\,\mu m$) and the ohmic indium contact on the right ($x \geq 8\,\mu m$) of the CdS nanowire. The topography serves as a reference for the SPCM maps in figure 5.17b. Here it can be observed that a negative photocurrent is measured at the source contact, even for no applied bias. For negative biases, the photocurrent spot at the source contact increases and for -0.84 V the photocurrent extends over the nanowire itself. For positive biases, the photocurrent decreases until it disappears above 0.21 V and for even larger biases, a positive photocurrent, which is not confined to the contact regions, is measured.

The negative photocurrent spot can be explained by the separation of the charge carriers by the electric field of the Schottky contact. Electrons are collected by the drain contact, and holes by the source. Equivalent to solar cells, the observed current at 0 V is called short-circuit current (I_{SC}). In order to explain the SPCM maps in figure 5.17, the band structure of this device for different applied biases is visualized in figure 5.18. Figure 5.18a shows a sketch of the band structure of the diode device without an applied bias. The band bending at the Schottky source contact is responsible for the charge-carrier separation leading to the observed I_{SC}.

When a positive bias is applied to the source as illustrated in figure 5.18b, the energy of the contact is decreased, which reduces the band bending and thereby the electric field in the SCR. This explains the decreasing photocurrent in this region, as the charge carriers are separated less efficiently by the electric field.

As is shown in figure 5.18d, for larger biases the external potential is sufficient, to completely

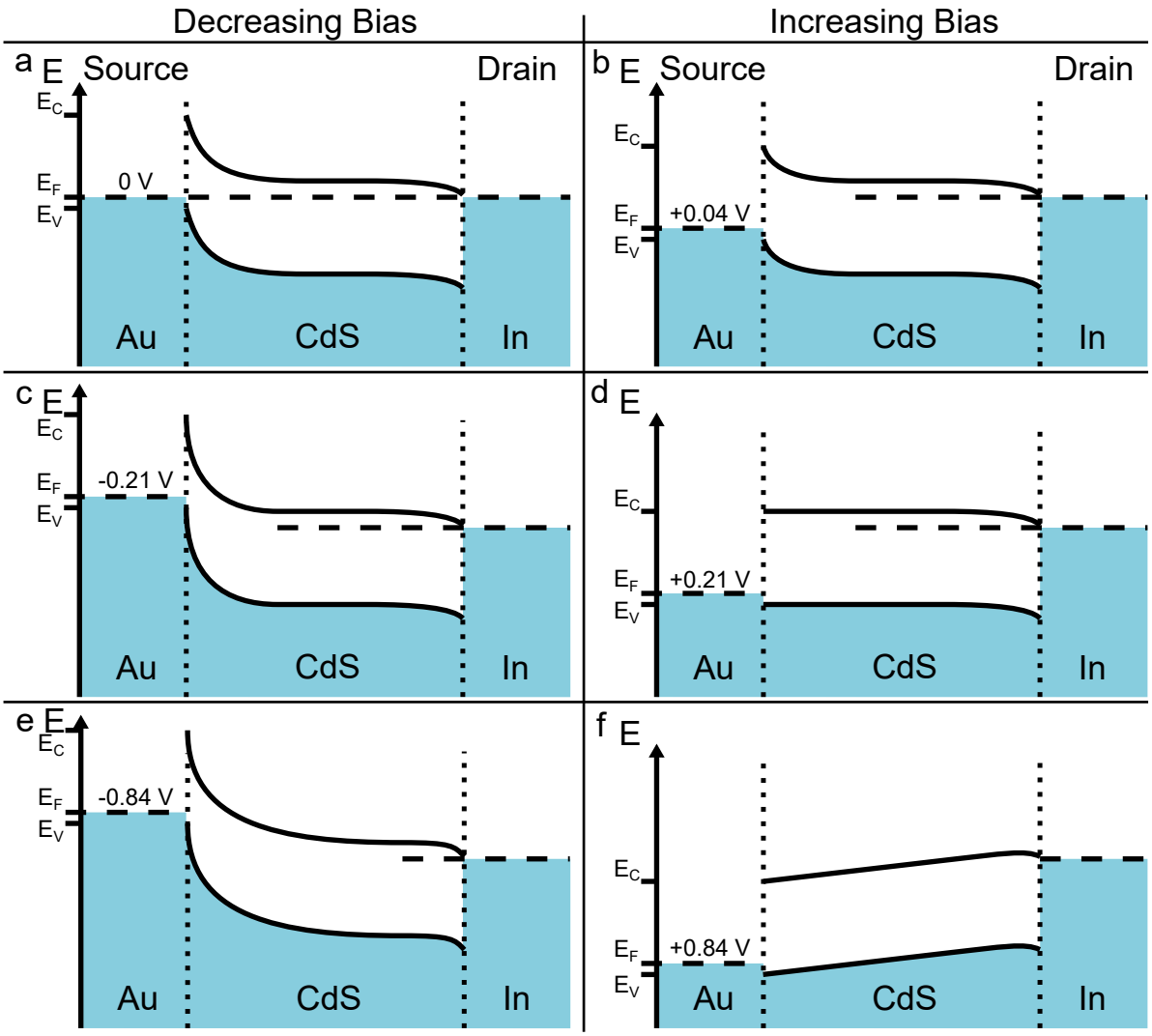

Figure 5.18: Exemplary band structures of a CdS nanowire diode device applied biases. The biases are specified on top of the respective source's Fermi level. a) No bias is applied to the source contact. b), d), f) Positive biases are applied, with the Schottky contact forward biased. c), e) Negative biases are applied, with the Schottky contact biased in reverse.

remove the band bending at the Schottky contact. The bias, which is applied at this point is called open-circuit voltage (V_{OC}). Further increasing of the applied bias leads to a slanted potential over the whole nanowire, as shown in figure 5.18f. The device now behaves ohmically with respect to the majority charge carriers (electrons), which is also reflected in the SPCM maps for biases larger than 0.4 V in figure 5.17b. Just like observed with the device with ohmic contacts, the photocurrent is now distributed over larger parts of the nanowire, as the whole nanowire exhibits the external electric field, which separates the charge carriers.

Figures 5.18c and e show how for negative applied biases, the SCR at the reverse biased Schottky contact increases. This increases the drift of charge-carriers and therefore the photocurrent. As the bias decreases further, the SCR extends ever farther along the nanowire, as

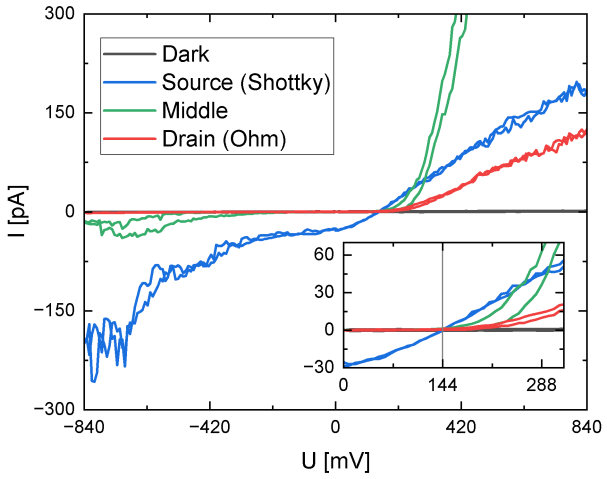

Figure 5.19: IV-curves of a CdS nanowire diode device with different local illumination positions. The inset shows the region around the V_{OC}, indicated by the gray line. Also in the inset, the I_{SC} is visible at 0 V bias.

shown in figure 5.18e. This is reflected as well in the SPCM map for -0.84 V in figure 5.17b, as here negative photocurrents can be measured over the whole nanowire, while charge carriers are separated by the extensive electric field.

The diode behavior of this device is also reflected in its IV-curves without illumination and for different illumination positions, as shown in figure 5.19. As with every other CdS nanowire device, no current is observed without illumination. For different local illumination positions, the IV-curves show the same trends as the SPCM maps, though with more bias information at the expense of spatial information.

For source illumination (blue curve) at 0 A, the I_{SC} of -0.03 nA is visible. For decreasing biases, the absolute current increases exponentially until -0.7 V, where it plateaus at around -0.2 nA. For positive biases, the absolute photocurrent is reduced until the V_{OC} is reached at 0.144 V, where the current is 0 V. For even larger positive biases, the photocurrent increases linearly.

The exponential behavior for negative biases fits to a reverse biased Schottky contact, whose SCR is increased. The reason for the plateauing is less straight forward, and might be related to the extensive photocurrent observed in figure 5.17b for -0.84 V. The electric field at this point may be sufficient to accelerate all excited holes into the source contact. Thereby the measured current flow would not anymore be limited by charge-carrier mobilities, but the excitation rate, which is constant, though other current limiting factors cannot be clearly ruled out.

For positive biases, the V_{OC} at 0.144 V indicates the bias at which the SCR at the Schottky contact is completely eliminated, which is also illustrated in figure 5.18d. From this point onward for more positive biases, ohmic behavior takes place with the IV-curve being linear for increasing biases. This fits well with the findings in figures 5.17b and 5.18f.

When the nanowire is illuminated at the ohmic drain contact (red curve), no current is observed for negative biases, while for positive biases, the current increases linearly only after the V_{OC} of 0.144 V is surpassed. For this excitation position, no holes are able to reach the SCR at the Schottky contact. Only for the ohmic behavior above the V_{OC}, does the electric field in the nanowire separate the charge carriers, whereby a photocurrent is measured, which increases linearly with the bias, as was already observed for source illumination. As the illumination is close to the hole collector, the current is electron limited.
The same holds true for the illumination in the middle of the nanowire (green curve), though the current increases much steeper (up to 1.5 nA for 0.84 V) than for source or drain illumination. In accordance to the theory discussed for the nanowire device with ohmic contacts, the currents are limited either by the excited electron's or hole's ability to reach their respective collecting electrode. At this illumination position, the current is apparently less limited by the electrons than for drain illumination.
For negative biases and illumination in the middle of the wire, a negative current can be observed for biases below -0.42 V. As shown in figure 5.18e, at this point, the SCR extends far enough into the nanowire to accelerate the charge carriers excited in the middle.
All of this goes to show the added complexities for diode devices, compared to their symmetric counterparts with just ohmic or Schottky contacts. To further probe the electric fields in this device, LI KPFM measurements were performed. Here, only profiles of these measurements are displayed, as the details are not easily discernible from color maps (shown exemplary in appendix figure B.3). Figures 5.20a and b show that the surface-potential profiles of the nanowire of the asymmetric diode device are different for positive and negative biases. This is in contrast to the symmetric ohmic device in figure 5.6. The KPFM data shows that for no illumination (black curves), the potential drop across the nanowire is steeper with the Schottky contact forward (positive) biased in figure 5.20a, than when the Schottky contact at the source is biased in reverse (negative) in figure 5.20b.
As a negative bias is applied to the source contact, as shown in figure 5.20b, electrons cannot overcome the barrier from the metal to the nanowire in order to propagate the potential. For the positive bias in figure 5.20a (which is above the V_{OC}), the potential drops across the whole nanowire, as is illustrated in figure 5.18f and is similar to the ohmic device in figure 5.6.
The surface-potential profiles for different illumination positions largely follow the trend of the respective unilluminated curves. Only for illumination of the ohmic drain contact with the positive bias in figure 5.20a, deviations are observed across the nanowire, where the surface potential is decreased relative to no illumination and increased at the point of illumination itself. For the negative bias in figure 5.20b only drain illumination, with an increased surface potential at the point of illumination, deviates significantly from the surface potential without illumination. The increased surface potential at the point of illumination is much less pronounced for illumination of the Schottky source contact, relative to drain

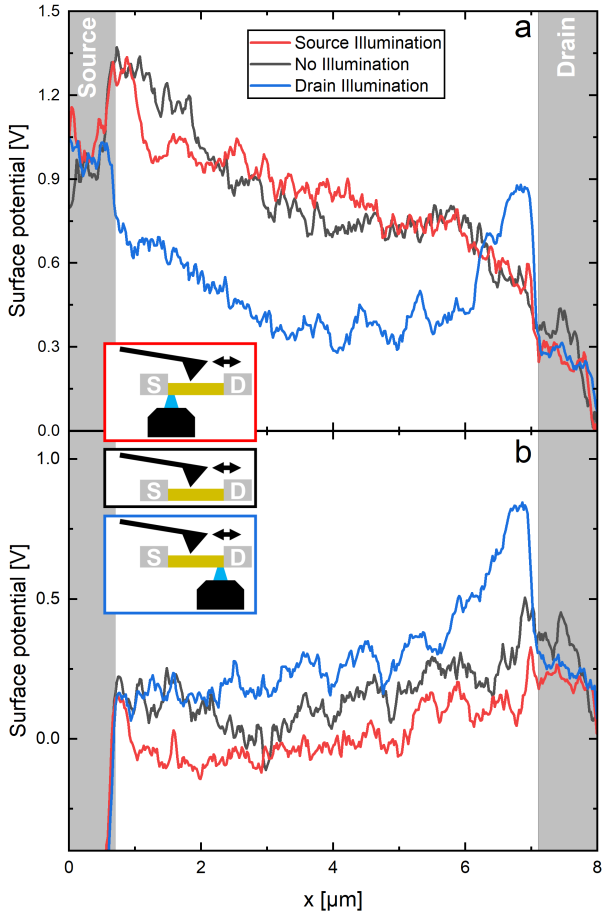

Figure 5.20: a) LI KPFM profiles of a CdS nanowire diode device with no (black) illumination, source (red) illumination and drain (blue) illumination at +2 V external bias. b) LI KPFM profiles with the same illumination positions at -2 V external bias.

illumination.

The interpretation of the surface potential curve for illumination of the ohmic drain contact for the positive bias, in figure 5.20a, is the same as for the ohmic device, discussed in section 5.2.3. Here, excited electrons are accelerated by the electric field towards the source contact. The charge-carrier concentration across the nanowire along with the external electric field leads to the lowered surface potential, relative to no illumination.

The increased surface potential at the point of illumination at the ohmic drain contact can again be explained by the EHC at this position. Interestingly, for illumination of the Schottky source contact, the increased surface potential at the point of illumination is less pronounced for both biases. This would indicate that excited holes are accelerated away from this position. For the positive bias, the SCR of the Schottky contact should be diminished by the external bias. Therefore, the reason for the less pronounced surface potential increase is unclear at this point.

For illumination of the Schottky source contact at the negative bias in figure 5.20b, the decreased EHC, relative to drain illumination, can be explained by the SCR which is responsible

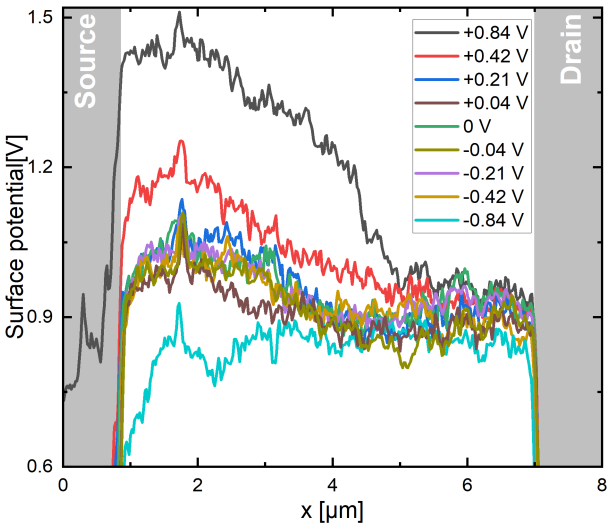

Figure 5.21: LA KPFM profiles of a CdS nanowire diode device with external biases.

for the charge-carrier separation. Thereby holes are accelerated into the source contact. This is also reflected by the current in the SPCM map for 0 V in figure 5.17 and the IV-curves for source illumination in figure 5.19. At the drain contact no such SCR is present, whereby the EHC is comparable to the ohmic behavior. As the external electric field for negative biases largely stays confined to the SCR of the Schottky contact, the potential profiles of the illuminated wire are much more similar to no illumination than for the forward biased case or the ohmic device in general.

Further information on the excited hole distribution, and asymmetric device behavior, was gathered using LA KPFM, the resulting surface-potential profiles of which are shown in figure 5.21. The curves in figure 5.21 were not adjusted for a linear external potential, as was done in figure 5.9, because in this device the external potential only drops linearly across the wire for large forward biases and otherwise drops nonlinearly across the SCR of the Schottky contact. The LA KPFM data was recorded simultaneously to the SPCM data shown in figure 5.17. It can be divided into three different categories.

Firstly, for positive biases above the V_{OC} (+0.42 V and +0.84 V) the surface potential rises from the source contact to the maximum at around 2 µm, from where it decreases towards the drain contact (hole collector). This is largely the same behavior as was observed for the ohmic device described in section 5.2.4, where it was explained that the drop of the surface potential (and EHC) towards the drain contact is due to an increasing amount of excited holes reaching the contact. Here, this corresponds to the current observed in figure 5.17 for the respective biases (+0.42 V and +0.84 V). The lower surface potential right at the source electrode compared to the maximum correlates to a lower EHC, observed for source illumination in figure 5.20, may be explained by the hole diffusion/drift into the source contact.

Secondly, the 0 V and low absolute bias (+0.21 V to -0.42 V) LA KPFM data largely behave uni-

formly. Again, from the source contact the surface potential rises to a maximum at 2 µm, after which it then drops off towards the drain contact. For low absolute biases the external electric field is confined to a small region (SCR) near the source electrode, whereby the surface potential of the nanowire is the same as the surface potential for no applied bias. For the illumination close to the Schottky source electrode, the SCR accelerates the holes into the source contact, whereby the surface potential is lower than at the maximum. An explanation for the existence of the maximum is more complicated and might be grounded in the combination of the differing electron and hole mobilities, and the SCR. When the excitation takes place outside but close to the SCR of the Schottky source contact, the wider distribution of excited electrons leads to them being accelerated by the SCR towards the drain contact, as the electrons, which diffuse to the source, are affected by the electric field in the SCR. On the other hand, the holes, which do not move far from the point of excitation, do not experience the same drift in the other direction, as they do not reach the SCR of the Schottky source contact. Thereby the EHC is increased, relative to excitation positions farther from the SCR to the drain, where less electrons diffuse into the SCR to be accelerated. In essence, at the maximum EHC, the electron distribution is shifted away from the point of illumination, while the hole distribution remains localized to the point of illumination.
Thirdly, the large reverse bias of -0.84 V leads to a different behavior compared to lower absolute biases, as was observable the SPCM maps in figure 5.17 as well. The surface potential in general is lower than for the larger biases (-0.42 V to +0.84 V). As the SCR and its electric field are increased by the applied bias, ever more holes are accelerated into the source contact. This also affects holes that are excited farther away from the source contact, which leads to the photocurrent profile of the nanowire shown in figure 5.17 for -0.84 V.
These findings show that the asymmetric diode device possesses properties of both devices with two Schottky and two ohmic contacts. However, the diffusion/drift of the charge carriers leads to additional differences in the nanowire's surface potential, exceeding the observations in purely ohmic or Schottky devices. As such, the characterization of a diode device alone is not sufficient to fully characterize ohmic and Schottky contacts to a semiconductor, and does not eliminate the need to characterize devices with only ohmic or Schottky contacts. In order to quantitatively analyze this data and corroborate the theory presented here, similar simulations as were shown in figure 5.2.5 would be necessary.

5.4 Nanosheets

In addition to experiments on nanowires, similar studies were performed on SnS and SnSe nanosheets, as well as heterogeneous structures such as framed SnS@SnSe nanosheets and SnSe nanosheets decorated with AuNPs. The aim was to find charge-carrier separation and mobility induced charging in p-type semicondcutors with different properties to the n-type

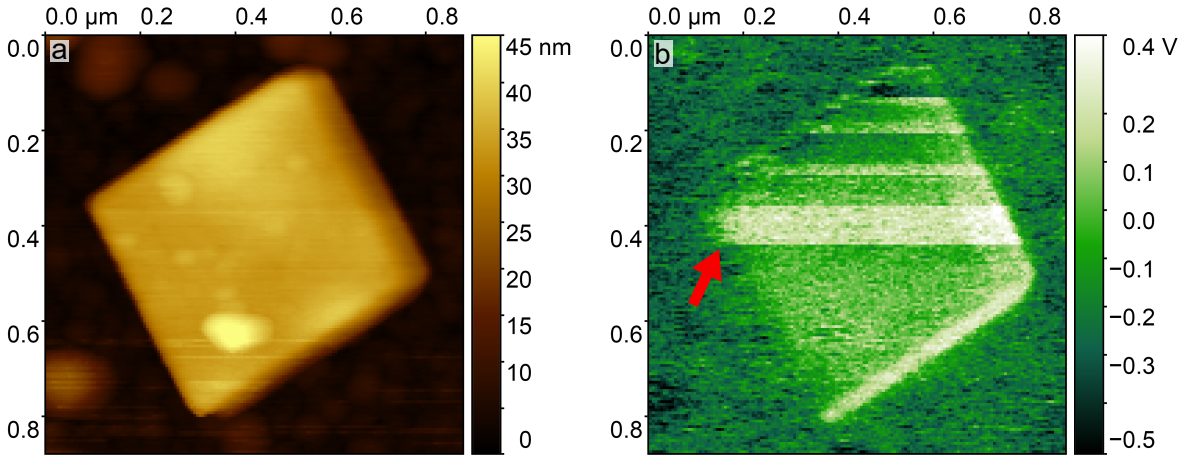

Figure 5.22: a) Topography image of a SnS@SnSe nanosheet which exhibited charging during the measurement. b) Surface-potential map of the same nanosheet, where one exemplary position where charging took place is indicated by the red arrow.

CdS nanowires described in section 5.2.1. Also, for heterogeneous structures, charge-carrier separation between the materials should be found.
For the local illumination in all nanosheet experiments, a laser with a wavelength of 440 nm was used at different power densities at the sample, up to 740 kW/cm^2. The experiments were performed in a nitrogen atmosphere (oxygen below 5 %) at 20 %RH.

5.4.1 Triboelectric Charging

During preliminary measurements of copper sulfide (CuS) nanosheets, it was found that nanosheets pose unique challenges for KPFM measurements, compared to nanowires. Beyond problems caused by the stacking of nanosheets into large clusters, KPFM measurements of individual nanosheets revealed that they could exhibit strong electrostatic charging of up to ±10 V during the measurement. The charging usually occurred, when during a line scan the measuring tip was right at the edge of the nanosheet and persisted until the next charging event or until the charge dissipated through the SiO_2 insulating layer into the backgate, which could take hours depending on the charge amount.
The charging of a SnS@SnSe-framed nanosheet along with its topography is shown exemplary in figure 5.22. The topography in figure 5.22a shows that the nanosheets surface is mostly flat apart from a few spots, which might be smaller remnants of SnS or SnSe. AFM and KPFM maps are measured in fast x axis scan lines from the bottom to the top with a slow y axis. In figure 5.22b it can be seen that starting from specific scanning lines, the nanosheet experiences charging, while the substrate in the background is not affected. By doing multiple measurements at different resolutions and measurement angles, it was found that the charging always occurred at specific positions at the edge of the nanosheet with an apparently random charge. These specific positions however, do not show any special features in

the topography. Direct charge transfer due to a potential difference between the tip and the sample was ruled out, since this potential difference is continuously nullified in KPFM. It was concluded that the charging is most likely due to triboelectric charging of the nanosheet by the measuring tip, as the tip may rub against the sheet each scan line. Triboelectric charge transfer on the nanoscale is a complex process and may be influenced in SPM experiments by the applied forces, electric fields, ambient conditions or damage and contamination of the measuring probe.[62] Changing the measuring parameters of the AFM controller or the KPFM lock-in amplifier could not reliably prevent this charging, even when the mechanical interaction between the tip and the sheet was minimized. Also, no connection to either the humidity or oxygen content of the atmosphere was found. It was therefore deemed imperative to improve the discharging through the backgate, as the charging itself could not be prevented.

5.4.2 Charge Separation in SnS@SnSe Nanosheets

Independently from the triboelectric charging, no mobility induced charge-carrier separation was measurable for either SnS or SnSe, and further experiments were performed on SnS@SnSe-framed nanosheets under illumination. These sheets stem from a different synthesis batch than the one shown in figure 5.22. To facilitate efficient discharging of the nanosheets, experiments were performed on ITO without the insulating SiO_2 layer. This however bears the possibility of band bending and chemical reactions by the direct contact between the nanosheets and the metallic ITO surface, therefore these measurements were conducted primarily as prove of concept.

The topography and surface potentials of a SnS@SnSe-framed nanosheet with and without illumination are shown in figure 5.23. The topography in figure 5.23a shows that a difference in height between the SnSe core and the SnS frame of the nanosheet of around 1 nm exists. This may be explained by the synthesis mechanism, which is not part of this work.[55]

The surface potential data in figure 5.23b shows no difference between the core and the frame. It is possible that SnS from the frame also covers the basal plane at the surface of the SnSe core, whereby mainly the surface potential of SnS is measured. For the interpretation of the KPFM data, the information about the SnSe-core position and orientation gained from the topography is important, as very small differences in the surface potential can be found and measured more easily by averaging over the respective regions. As shown in figure 5.23c, during illumination of the sheet with 250 W/cm^2, the cores surface potential is on average 20 mV below that of the frame. Figure 5.23d shows the same sheet after the illumination, where the surface potential difference between the core and the frame is not measurable anymore. This shows that the surface potential difference is reversible with and without illumination.

As it is likely that SnS covers the SnSe surface and the SnS layer shields the surface potential

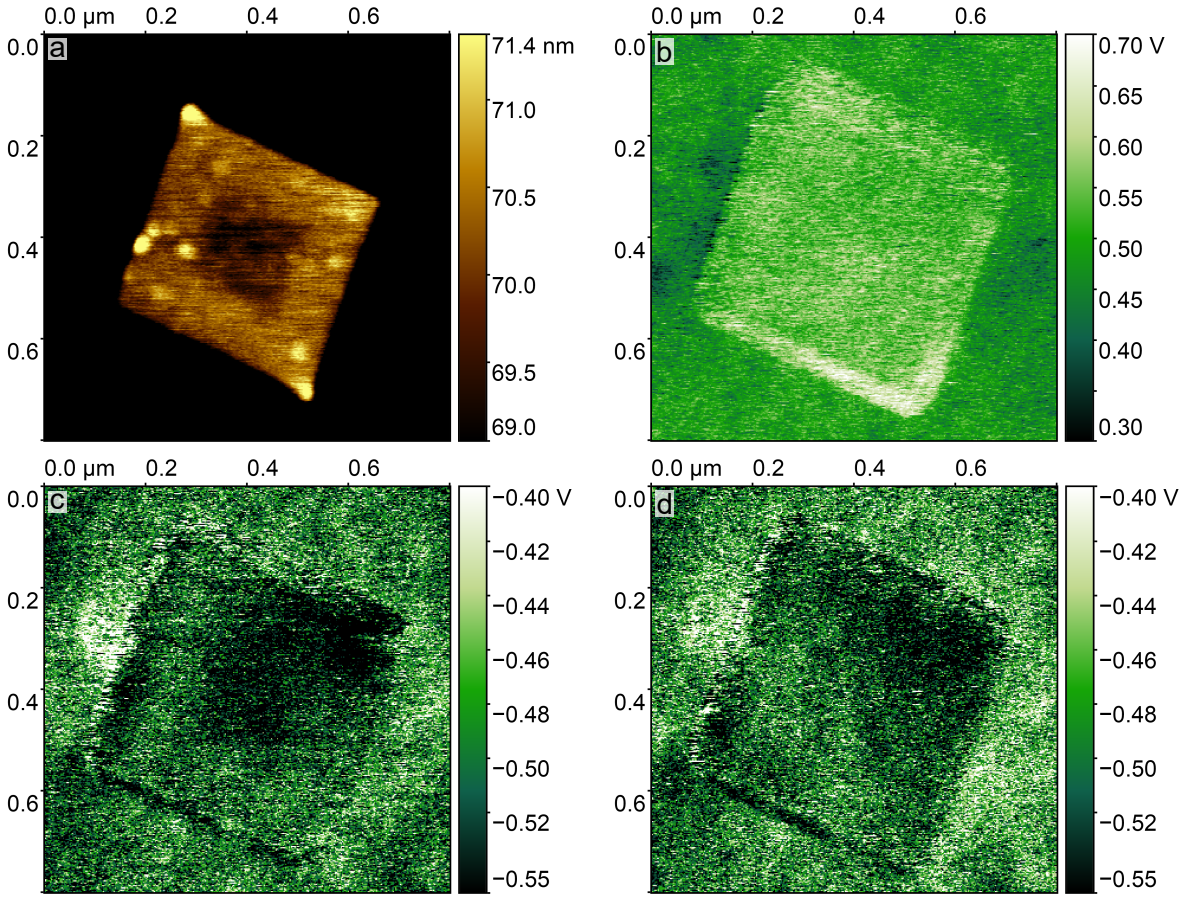

Figure 5.23: a) Topography image of a SnS@SnSe-framed nanosheet. b)-d) Surface-potential maps of the same sheet, obtained b) before, c) during and d) after illumination at 250 W/cm^2.

of the SnSe, the potential difference is probably lower than the actual difference between the two materials. Yet, this gives an indication that the work function of SnSe may be lower than that of SnS, because under illumination, excited electrons are apparently transferred from the frame to the core. This goes along with the work function literature values of 3.91 eV for SnSe and between 4.3 eV and 4.9 eV for SnS.[63, 64]

As previously mentioned, a significant issue with these measurements is that the nanosheet is in direct contact with the ITO surface. Therefore, exact interpretations of the measurements are not possible, and they mainly serve as a prove of concept for future measurements. Furthermore, the bare ITO surface showed another problematic property, as it charges up positively upon illumination. Figure 5.24 shows the topography and surface potential of the ITO surface with nanosheets. Beforehand, centered to the image, a region of 9x9 µm was scanned with the laser at 250 W/cm^2. Figure 5.24a shows the topography of the ITO surface with six nanosheets on top. Here, no influence of the previous illumination can be seen. In the KPFM data in figure 5.24b however, the 9x9 µm region of the ITO, which was illuminated beforehand, was charged up positively compared to the unilluminated parts around it. The nanosheet to the very right was additionally measured beforehand with the laser, whereby

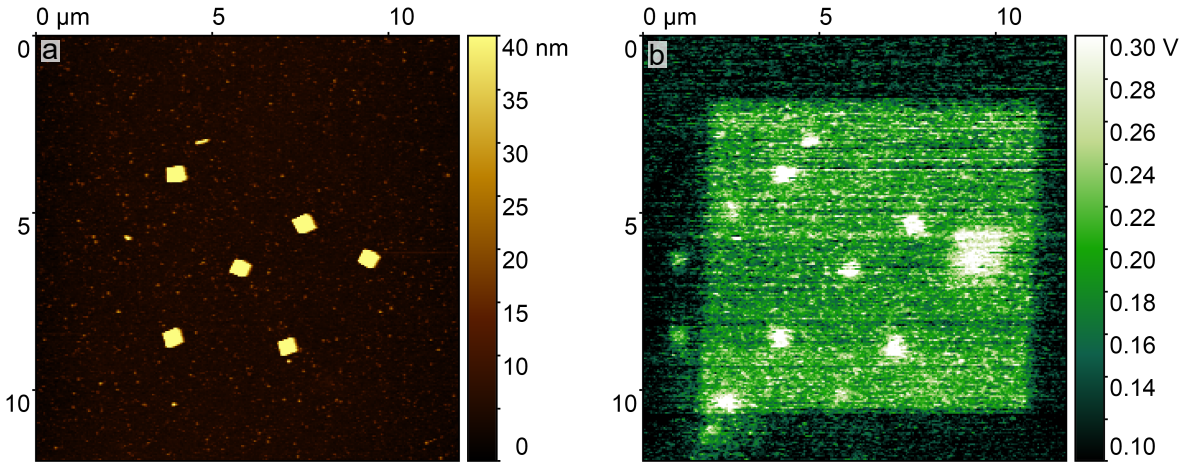

Figure 5.24: a) Topography image of the ITO sample surface with six nanosheets. b) Surface-potential map of the same area, after the center region was scanned with the laser at 250 W/cm^2.

the region scanned around it, is even more positively charged. This kind of charge persists for a long duration (up to days) and the charging and discharging is independent from the atmosphere. As the substrate is grounded, one would expect this charge to flow off faster, after the illumination stopped. The persistence of the charge may indicate a chemical reaction at the surface of the ITO, induced by the laser.
These findings show the importance of an insulating and passivating layer in KPFM experiments with and without illumination. Not using a passivating layer for faster discharging of the sheets, is not suitable to account for the charging of nanosheets during measurements and different solutions need to be found in order to properly characterize nanosheets with and without frames.

5.4.3 SnSe Nanosheets Decorated with Gold Nanoparticles

Another way to amend the triboelectric charging on ITO samples passivated by SiO_2 is to use the fact that the charging is fast and happens mostly at the edges of the nanosheet. Since it can be assumed that the whole nanosheet is charged immediately (in the time frame of the experiment), post processing may be used to determine the median of each scan line and subtracting this value of each respective line. Thereby all scan lines are brought to a common average value, reversing the charging observed in the KPFM map. To that end, the align-rows feature of the software gwyddion can be used, which is usually used for the alignment of AFM topography maps. For the determination of the median line value, only values on the nanosheet are used to only account for its charge and not the background. As the whole scan line, including the background, is adjusted, this leads to corresponding artifacts in the background to the left and right of the nanosheet.

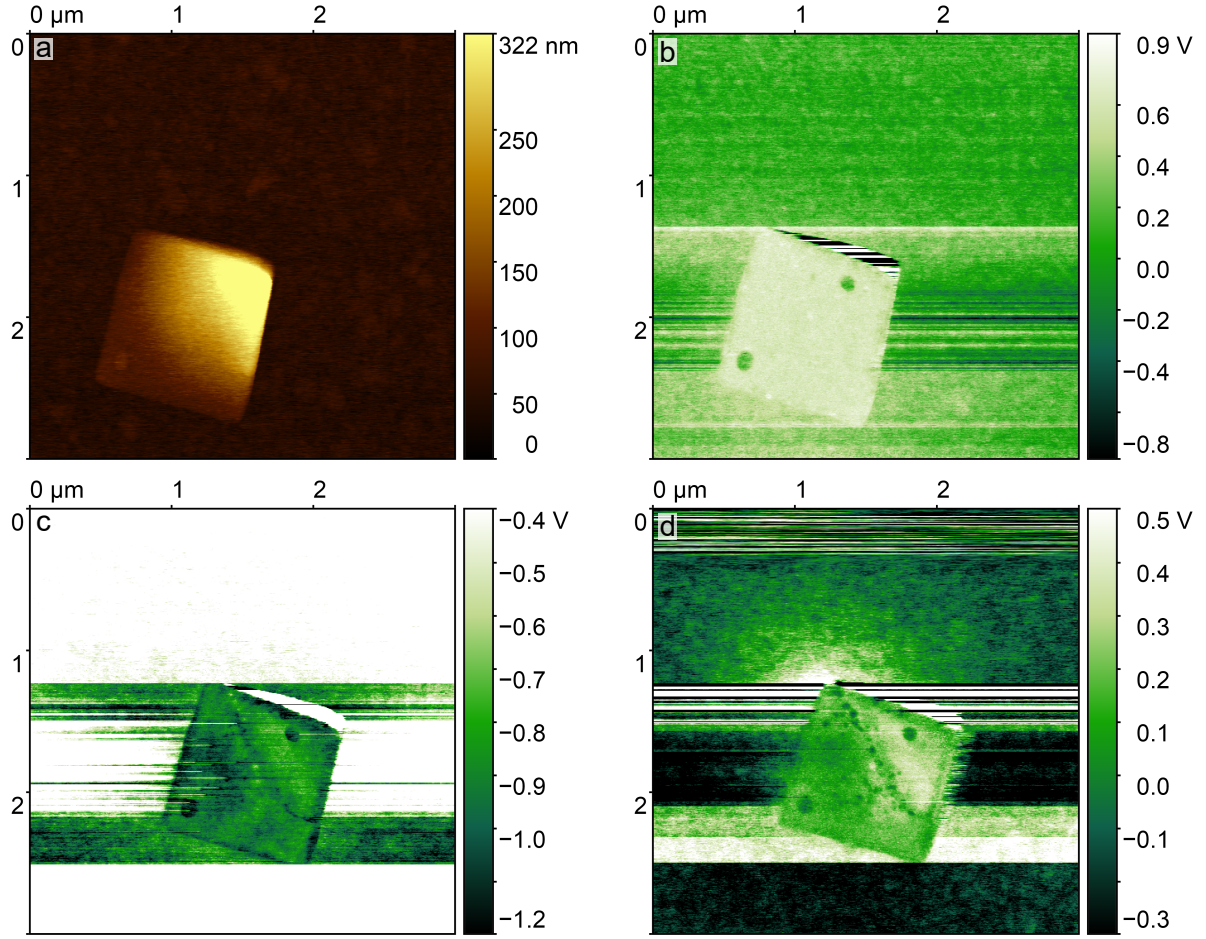

Figure 5.25: a) Topography image of a SnSe nanosheet decorated with AuNPs. b)-d) Surface-potential maps of the same nanosheet, obtained b) before, c) during and d) after illumination with a power density of 740 kW/cm^2. The surface-potential maps were post processed using row alignment.

Row alignment was used on the KPFM data of a SnSe nanosheet decorated with AuNPs shown in figure 5.25. Exemplary surface-potential images of the illuminated sheet before row-alignment and the masked region for determining the respective median line values may be found in the appendix figure B.4. Figure 5.25a shows the topography of the SnSe nanosheet, where the top right corner appears to be higher than the rest of the sheet, which may be stacking of another sheet, or non-uniformity of the sheet's surface itself. The AuNPs with diameters of just a few nanometers, which are expected to exist at the edges and the basal plane of the nanosheet, are not visible in the topography. Figure 5.25b shows the surface potential of the nanosheet before illumination, which is largely uniform apart from two circles of lower potential, which are most likely larger or clustered AuNPs. These clusters are faintly visible in the topography as well, and have a diameter of about 100 nm and a height of 50 nm. The clusters were excluded when determining the median line value for row alignment in order to obtain an accurate value for the SnSe nanosheet itself. A uniform surface potential of significant parts of the nanosheet is necessary for the row alignment procedure

to be accurate.
During illumination, the surface potential of the nanosheet, shown in figure 5.25c, is lowered compared to before or after the illumination. In addition to this, more negative small spots akin to the two larger ones seen before appear on the nanosheets basal plane. The lowered surface potential in general can be explained by the surface band bending of the p-type semiconductor as explained in section 2.3. Thereby excited electrons move to the surface, whereby a lower potential is measured. The even more negative spots seem to be AuNPs that charge up more negatively than the sheet during illumination of the semiconductor and the AuNPs seem to be more abundant at the edge of the higher feature in the top right corner of the sheet. Interestingly, the horizontal lines starting from the nanoparticles on the basal plane indicate that in these regions triboelectric charging took place during the measurements. Apparently the charged nanoparticles promote this type of charging of the nanosheet via the tip.
After illumination, the surface potential of the nanosheet shown in figure 5.25d, is again higher than during illumination, but still lower than before illumination, also the AuNPs are still negatively charged and visible as well. The surface band bending might not yet be completely reestablished, as well as the reverse charge transfer from the metal particles to the semiconductor.
To summarize this section, using row alignment in post-processing, the charge transfer between a SnSe nanosheet and attached AuNPs could conceptually be shown. Of course other solutions against the charging still need to be found, in order to perform more accurate measurements for quantitative analysis. A next step could be finding different insulating layers, or using thinner SiO_2 layers between 10-50 nm. These would not be sufficient to prevent a short circuit to the backgate for current measurements using electrodes, but may be sufficient to passivate the ITO surface, while also improving the discharging of the nanosheets after triboelectric charging events.

5.4.4 Contacted SnS@SnSe Nanosheets

Experiments of contacted nanosheets have the advantage that the AFM tip does not scan the sheets edges, as they are largely covered by the contacts, preventing the charging explored in the previous sections. Also, if any charging should occur during the measurement, charges can flow off directly through the contacts. The size of SnS@SnSe-framed nanosheets of 1 µm^2-2 µm^2 is very close to the resolution limit of the optical lithography setup used for the devices shown here. Therefore, first devices were fabricated on Si/SiO_2 instead of ITO substrates, as the Si/SiO_2 substrates provide a more uniform surface and are more reliable for lithography. Since the Si/SiO_2 substrates are not transparent, simultaneous optical and surface-potential measurements were not possible.
The aim was to perform preliminary measurements on the conductivity of the sheets with

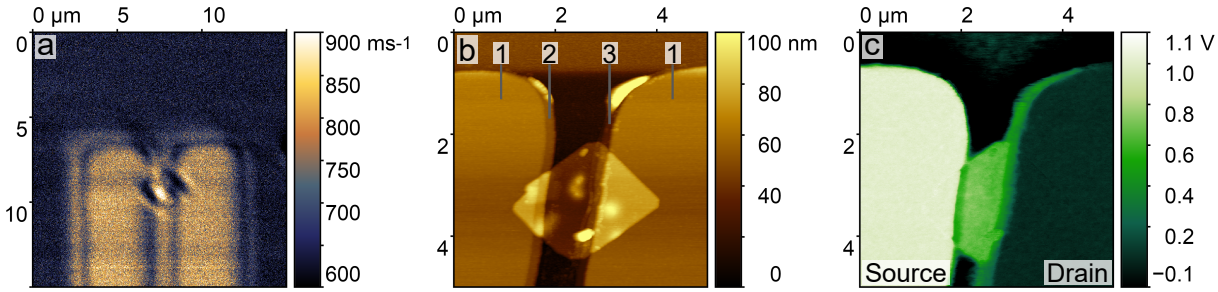

Figure 5.26: a) Laser reflection image of a SnS@SnSe-framed nanosheet contacted by Ti/Au on a Si/SiO_2 substrate. b) Topography image of the same contacted sheet, where the different contact material compositions (1)-(3) are marked for (1) Ti/Au, (2) Au and (3) Ti. c) Surface-potential map of the same sheet with +1 V bias at the source contact.

and without illumination. For these first experiments, framed nanosheets were used, to additionally investigate if the applied biases lead to different potentials between the core and the frame. Also, it should be verified if 40 nm gold on 10 nm titanium (Ti/Au) is a suitable contact material for the study of the sheets, while the titanium is used for better adhesion of the gold to the sample's surface.

Figure 5.26 shows images of a contacted nanosheet with respect to its laser reflection, topography and surface potential at +1 V bias. All of the data was measured on the same nanosheet. From the reflection of the laser on the sample in the region of the contacted nanosheet (figure 5.26a), it is clear that the nanosheets are highly reflective, even more than the gold contacts. This aids finding the sheets by optical methods but raises the question of whether these materials are suitable for optoelectronic applications, if large parts of incident light are reflected and not absorbed.

Figure 5.26b shows that the gold layer of the contacts is shifted to the right by about 200 nm, resulting in three distinct regions where the electrodes contact the sheet. In general, the bulk of the contacts is made of Ti/Au (1). Due to the shift of the gold layer, the right edge of the source contact shows a 10 nm height step, whereby the gold is in direct contact to the sheet (2). Conversely, the left edge of the drain contact shows a 40 nm height step, as the gold contact is shifted to the right, whereby parts of the titanium on the right are not covered with gold (3). This can also be seen in figure 5.26c by the increased surface potential on the grounded drain contact's left side, which can be attributed to a titanium dioxide surface. No difference between a SnSe core and a SnS frame can be discerned.

The IV-curves shown in figure 5.27 obtained with and without illumination of the nanosheet show a symmetrical, Schottky-type behavior. Only a small difference in current is observed upon illumination, possibly due to the highly reflective semiconductor surface, whereby a number of photons would not be absorbed to excite charge carriers. The symmetry indicates that both contacts are in general made of the same materials. However, the Schottky behavior suggests that the electrical contact is mainly facilitated by the titanium adhesion layer

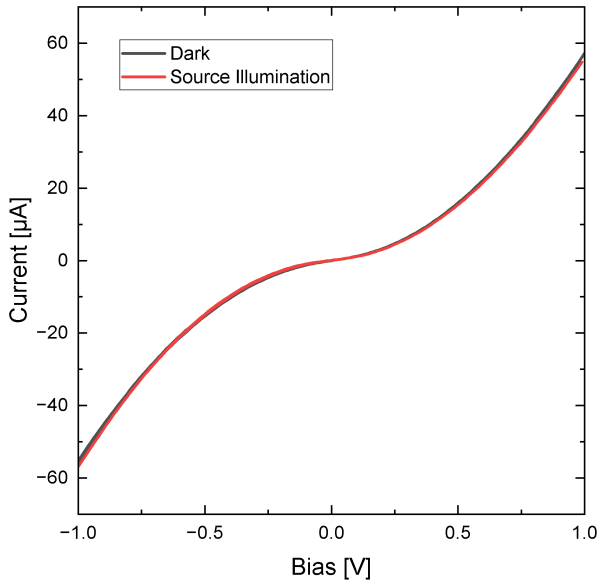

Figure 5.27: IV-curves of a SnS@SnSe-framed nanosheet contacted by Ti/Au with and without illumination of the source contact with a power density of 120 kW/cm^2.

instead of the gold. For gold, with a work function of about 5.3 eV, ohmic contacts to the p-type SnS@SnSe nanosheet would have been expected. The outer material of the framed nanosheet is most likely completely made of SnS with a work function of 4.3 eV-4.9 eV.[64] Since titanium has a work function of 4.3 eV,[61] which is generally lower than that of SnS downward band bending occurs in the semiconductor in the contact regions.

The sketch in figure 5.28 illustrates the band bending in the semiconductor, close to the electrodes. In the contact regions to the titanium electrodes in figure 5.28a, downward band bending occurs in the semiconductor. As SnS and SnSe are p-type semiconductors, holes are the majority charge carriers, for which Schottky barriers in the contact regions exist. In the SCRs, the electric fields are expected to separate excited charge carriers, by accelerating ex-

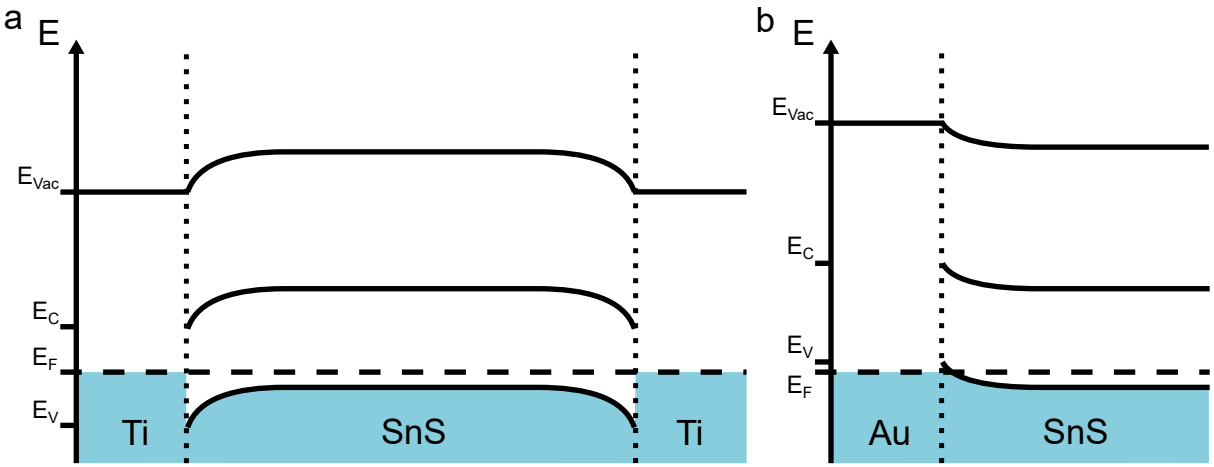

Figure 5.28: a) Exemplary band structure of a SnS nanosheet contacted by titanium. b) Exemplary band structure of the contact region between a gold contact and a SnS nanosheet.

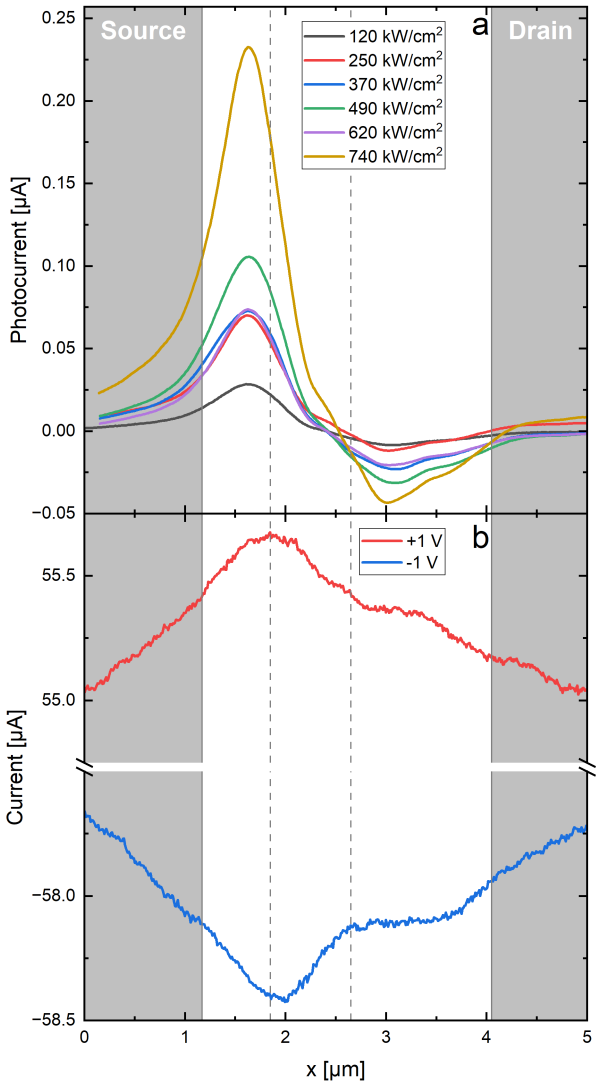

Figure 5.29: a) SPCM profiles of a SnS@SnSe nanosheet with two Schottky contacts at different laser powers and no bias, whereby solely the photocurrent is observed. b) SPCM profiles of the same sheet at different biases and a laser power of 120 kW/cm^2, where the current is a combination of the photocurrent and the dark current. The area between the vertical dashed gray lines (1.9 µm<x>2.7 µm) indicates the exposed parts of the sheet, with the covered parts of the sheet to the left and right of this region until the gray areas (x<1.2 µm, x>4.1 µm), where only the electrodes are present.

cited electrons into the respective contact and holes into the nanosheet. In contrast to this, in figure 5.28b upward band bending is illustrated in the semiconductor to the gold contact, which would correspond to an ohmic contact with respect to hole transport, which is not reflected in the IV-curves.

To probe the charge-carrier separation in the SCRs, SPCM profiles were recorded for different laser powers with no bias and with different biases, which are shown in figure 5.29. Here, the area between the dashed lines indicates the exposed parts of the sheet (1.9 µm<x>2.7 µm). To the left and right of this area the sheet is covered by the electrodes, until the gray areas

(x<1.2 µm, x>4.1 µm) where only the electrodes are present. Figure 5.29a shows maxima of the absolute short-circuit current (I_{SC}) for all laser powers, occurring when the parts of the nanosheet which are covered by the electrodes are illuminated. This shows that the SCRs mainly exists in the vertical titanium-SnS interface below the contacts. The aforementioned 200 nm gold overhang, seen in figure 5.26b, which is also in contact with the nanosheet appears not to have a significant impact on the I_{SC}.
The SPCM profiles in figure 5.29b show a different behavior, compared to the I_{SC}. The measured currents are spatially broader in general, the absolute current maxima are not located below the contacts, but at the edge, and the absolute current maxima are at the same contact even for different signs of the applied bias. The positions of the absolute current maxima coincide with the gold contact at the source electrode, which seems to affect the photocurrent, if biases are applied. The combination of two interfaces with different electrical characteristics, one Schottky type and one ohmic type contact, at the same electrode, is too complex to be represented in a simple band diagram, so simulations would again be necessary to fully understand the charge-carrier dynamics. However, the positions of the absolute I_{SC} maxima in figure 5.29a show that the large contact area of the sheets below the electrodes is very important for the transfer of charge carriers. This must be taken into account, when designing new samples with ohmic, Schottky or mixed contacts.
Figure 5.30 shows KPFM profiles of the nanosheet without illumination, as the non-transparent substrate does not allow for simultaneous usage of the optical setup. Figure 5.30a shows the surface potential of the device for different applied biases (without illumination). For no applied bias, it can be observed that the surface potential of the nanosheet is higher than that of the surrounding gold surface. To the right of the sheet at $x \approx 2.75$ µm, the increased surface potential of the titanium dioxide can be seen. The left side of the sheet itself at $x \approx 2$ µm shows a decrease in its surface potential. Relative to no bias, for $+1$ V and -1 V applied bias, the source's surface potential is shifted by the respective bias, while the grounded drain contact remains at the same surface potential. Between these, the nanosheet's surface potential is increased (decreased) by about 0.30 V - 0.35 V for the positive (negative) bias.
The decreased surface potential of the sheet at $x \approx 2$ µm may be explained by the sheets contact to the gold of the source electrode. The upward band bending of the sheet towards the contact, illustrated in figure 5.28b, corresponds to the decreasing surface potential observed in the KPFM data. This data also hints towards the reason why the Au-SnS contact area shows a photocurrent peak for both positive and negative applied biases (see figure 5.29b). Not the lowered surface potential of the sheet itself, but the larger potential step to the source contact at x=1.9 µm may accelerate excited electrons to the source for positive and to the drain for negative applied biases, leading to the increased absolute current flow for both positive and negative biases, when this region is illuminated.

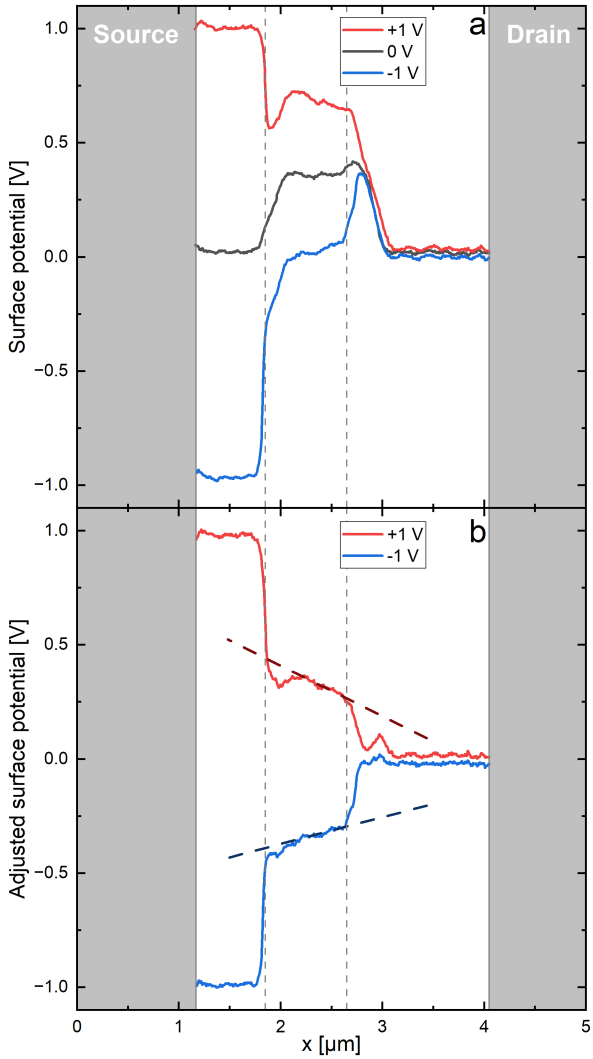

Figure 5.30: a) KPFM profiles of a contacted SnS@SnSe nanosheet with applied biases. b) The same profiles adjusted for the surface potential measurement without an applied bias, where the red and blue dashed lines indicate the linear fit of the potential change of the nanosheet. The area between the vertical dashed gray lines (1.9 µm<x>2.7 µm) indicates the exposed parts of the sheet, with the covered parts of the sheet to the left and right of this region until the gray areas (x<1.2 µm, x>4.1 µm), where only the electrodes are present.

Lastly, it can be taken advantage of the fact that, in contrast to nanowire devices, this device shows a measurable current without illumination. Thereby the change in potential over the nanosheet when biases are applied along with the measured current can be used to determine its conductivity. To that end, figure 5.30b shows the adjusted surface potentials, where the unbiased surface potential was subtracted from the biased potentials (from figure 5.30a). Thereby, possible deviations of the nanosheet's surface potentials, due to surface adsorbents or other surface effects, which would be the same in every KPFM profile, are removed from the data.

The adjusted surface potentials are linear across the nanosheet, apart from the deviating potential at the source contact. The linear changes in surface potential of the nanosheet were

fitted to determine potential differences ΔV of 0.11 V for +1 V applied bias and 0.04 V for −1 V applied bias over a distance l of 0.46 µm. The topography map in figure 5.26b was used to determine the average cross section of the nanosheet A over this distance as 0.053 µm^2. The current I was measured to be 56 µA for +1 V applied bias and 59 µA for −1 V applied bias. Using these variables, the equation

$$\sigma = \frac{I}{\Delta V}\frac{l}{A} \tag{5.1}$$

can be used to calculate the conductivity σ of the SnS@SnSe-framed nanosheet. This is possible as the current flow through the nanosheet itself can be described as ohmic, independent from the nature of the contact materials interfaces. Thereby the conductivity based on the measurements at +1 V applied bias is calculated to be 44 S/cm. Interestingly, when based on the measurements for −1 V, the resulting conductivity is 130 S/cm. While the exact reasons for this deviation are unclear, one reason might be the trapezoid shape of the nanosheet between the contacts. Nevertheless, the values are within the ranges found in the literature with 55 S/cm - 500 S/cm for SnSe[8,65,66] and 5 mS/cm - 1 S/cm for SnS.[67,68]

These experiments show that KPFM of such devices is a powerful tool not only for surface characterization, but can also replace additional four-point measurements. These are challenging to perform on small structures, such as the ones presented here, due to the difficulties in fabricating even two electrodes, let alone four.

Besides addressing the challenges around triboelectric charging, future characterizations of these nanosheets should be performed on transparent substrates for simultaneous optical, current and surface potential measurements. Also, to investigate the different contact types, the contact materials should be clearly defined to prevent ambiguities as found with regard to figure 5.29. To that end contacts could be made entirely of titanium for Schottky contacts, or the top gold layer could have a larger overlap, so only the gold is in contact with the nanosheet, for ohmic contacts. The lithography used to produce these contacts would ideally be electron-beam lithography, due to its higher resolution compared to optical lithography, which aids the contacting of smaller nanosheets.

6 Summary and Outlook

In this work, different independent setups for optical, electrical and surface potential measurements were successfully combined for simultaneous measurements of nanostructured semiconductor devices. This allowed for the electrical characterization of these semiconductor devices under local illumination by using SPCM and also enabled the development of H KPFM methods under local illumination. Specifically, LI KPFM was used for measurements of surface-potential profiles of biased devices under local illumination and LA KPFM was employed to qualitatively reveal the extent of the EHC caused by different charge-carrier mobilities and electric fields. Using this setup, the recording of SPCM, LA KPFM, laser-reflection, PL and topography maps was achieved in one single experiment.

The combination of all these methods was used to gain further insight into the mechanics of charge-carrier separation in nanoscopic semiconductor devices *in operando*. This was done extensively for the analysis of a CdS nanowire device with ohmic indium contacts. First of all, the mobility induced charge-carrier separation in CdS nanowires under local illumination with and without contacts was demonstrated while introducing LI and LA KPFM. SPCM revealed the ohmic character of the CdS nanowire-indium contact with electron and hole limited currents. The different electric fields leading to these currents were studied by surface potential measurements. It was found that the mobility induced charge-carrier separation has a significant impact on the electric fields present in locally illuminated nanowire devices, while the charge-carrier distribution is also affected by the external electric field.

Simulations of the system were deemed most practical to determine key variables of the semiconductor material such as the mobilities and also to gain further insight into the different electric fields in the active device.

Additionally the effect of the measuring tip on the excited charge-carrier distribution and resulting currents was studied. It was found that the alternating electric field of the KPFM tip could alter the charge-carrier distribution in the sample and thus affect the amount of excited charge carriers reaching their respective collecting electrodes, inducing currents in the range of a few picoamperes.

In addition to the study of CdS nanowires with ohmic contacts, experiments were also performed on CdS nanowire devices with two platinum Schottky contacts and diode devices with one ohmic and one Schottky contact, to gain first insights and plan efficient measurement series. For the Schottky device it was found that for low applied biases some ohmic behavior still occurred with diffusion-dominated currents. For the diode device, typical diode SPCM maps and IV-curves were obtained, and the device could be switched between ohmic and Schottky currents, depending on the applied forward or reverse bias. However, the surface potentials of the diode device revealed that diffusion/drift of the charge carriers

together with the SCR lead to different charge-carrier distributions, compared to both ohmic and Schottky devices.
Using the same setup, SnSe, SnS and SnS@SnSe-framed nanosheets were studied as well. Here, for uncontacted sheets, spontaneous charging prevented unambiguous measurements. No practical solution was found so far, though by using ITO for fast discharging and post-processing, some initial insights into the charge-carrier separation of illuminated framed nanosheets and SnSe nanosheets decorated with AuNPs were found.
This triboelectric charging needs to be addressed for accurate and quantitative measurements in the future. To that end, different insulating layers on the ITO with different thicknesses could be explored, as well as the charging mechanism in general.
For contacted SnS@SnSe-framed nanosheets no triboelectric charging was observed. Again the nature of the contact interfaces was revealed using SPCM and KPFM. The latter also proved useful, as it provided a means to determine the conductivity of the nanomaterial itself.

The setup and methodology presented in this work are suitable for future characterizations of nanoscopic semiconductor devices. Based on the preliminary insights for tin chalcogenides and CdS nanowires with different contact materials, experiments should be performed similarly to those shown here for the CdS nanowire device with ohmic contacts. To ensure optimized metal-semiconductor interfaces, electron-beam lithography should be used for the fabrication, especially for smaller nanostructures. For nanowires it was unclear if the different results between Schottky and diode devices for low applied biases were due to the different Schottky contact metals (gold and platinum), or due to the respective device nature in general. Therefore it would probably not suffice to only use diode devices to characterize its ohmic characteristics with forward biases and Schottky characteristics with reverse bias. As such, for each semiconductor material to be studied, ohmic and Schottky characteristics should be studied on independent devices in addition to a diode device, as was done with CdS nanowires in this work.

References

[1] C. Thelander, T. Martensson, M. T. Björk, B. J. Ohlsson, M. W. Larsson, L. R. Wallenberg, L. Samuelson, *Appl. Phys. Lett.* **2003**, *83*(10), 2052.

[2] P. V. Kamat, *J. Phys. Chem. C* **2008**, *112*(48), 18737–18753.

[3] M. S. Gudiksen, L. J. Lauhon, J. Wang, D. C. Smith, C. M. Lieber, *Nature* **2002**, *415*(6872), 617–620.

[4] Y. Hu, J. Zhou, P. Yeh, Z. Li, T. Wei, Z. L. Wang, *Adv. Mater.* **2010**, *22*(30), 3327–3332.

[5] A. Dutta, A. Medda, R. Bera, K. Sarkar, S. Sain, P. Kumar, A. Patra, *ACS Appl. Nano Mater.* **2020**, *3*(5), 4717–4727.

[6] M. Y. Lu, M. H. Hong, Y. M. Ruan, M. P. Lu, *Chem. Commun.* **2019**, *55*(37), 5351–5354.

[7] S. Gupta, Y. Batra, B. R. Mehta, V. R. Satsangi, *Nanotechnology* **2013**, *24*(25).

[8] K. Tyagi, B. Gahtori, S. Bathula, N. K. Singh, S. Bishnoi, S. Auluck, A. K. Srivastava, A. Dhar, *RSC Adv.* **2016**, *6*(14), 11562–11569.

[9] Z. Hu, S. Liu, H. Qin, J. Zhou, X. Peng, *J. Am. Chem. Soc.* **2020**, *142*(9), 4254–4264.

[10] K. Balasubramanian, Y. Fan, M. Burghard, K. Kern, M. Friedrich, U. Wannek, A. Mews, *Appl. Phys. Lett.* **2004**, *84*(13), 2400–2402.

[11] E. Meyer, H. J. Hug, R. Bennewitz, *Scanning Probe Microscopy*, Advanced Texts in Physics, Springer Berlin Heidelberg, Berlin, Heidelberg, **2004**, p. 2–5, 45–60, 78f, 91.

[12] J. Colchero, A. Gil, A. M. Baró, *Phys. Rev. B - Condens. Matter Mater. Phys.* **2001**, *64*(24).

[13] S. Sadewasser, T. Glatzel, *Kelvin Probe Force Microscopy*, vol. 48 of *Springer Series in Surface Sciences*, Springer Berlin Heidelberg, Berlin, Heidelberg, **2012**, p. 20.

[14] W. Melitz, J. Shen, A. C. Kummel, S. Lee, *Surf. Sci. Rep.* **2011**, *66*(1), 1–27.

[15] V. W. Bergmann, S. A. L. Weber, F. Javier Ramos, M. K. Nazeeruddin, M. Grätzel, D. Li, A. L. Domanski, I. Lieberwirth, S. Ahmad, R. Berger, *Nat. Commun.* **2014**, *5*(1), 5001.

[16] R. Shikler, N. Fried, T. Meoded, Y. Rosenwaks, *Phys. Rev. B - Condens. Matter Mater. Phys.* **2000**, *61*(16), 11041–11046.

[17] S. Schäfer, Phd thesis, University of Hamburg, **2011**.

[18] P. Atkins, J. de Paula, J. Keeler, *Atkins' Physical Chemistry*, 11. ed., Oxford University Press, Oxford, **2018**, p. 641f, 656–659, 669–671, 690, 704.

[19] S. Kitamura, *J. Phys. Soc. Japan* **1960**, *15*(12), 2343–2350.

[20] L. Brillson, *Surf. Sci.* **1994**, *299-300*(C), 909–927.

[21] S. Goßner, *Grundlagen der Elektronik*, 10. ed., Shaker Verlag, Herzogenrath, **2018**, p. 20–46.

[22] S. M. Sze, *Physics of Semiconductor Devices*, 3. ed., Wiley-Interscience, New Jersey, **2007**, p. 136.

[23] C. Hu, *Modern Semiconductor Devices for Integrated Circuits*, 1. ed., Prentice Hall, New Jersey, **2010**, p. 38f, 140.

[24] M. Grundmann, *The Physics of Semiconductors*, Graduate Texts in Physics, 3. ed., Springer International Publishing, Cham, **2016**, p. 234f, 295f, 711–715.

[25] S. Schäfer, Z. Wang, R. Zierold, T. Kipp, A. Mews, *Nano Lett.* **2011**, *11*(7), 2672–2677.

[26] M. Nasilowski, B. Mahler, E. Lhuillier, S. Ithurria, B. Dubertret, *Chem. Rev.* **2016**, *116*(18), 10934–10982.

[27] S. Santos, A. Verdaguer, *Materials (Basel).* **2016**, *9*(3), 182.

[28] F. Gossenberger, T. Roman, K. Forster-Tonigold, A. Groß, *Beilstein J. Nanotechnol.* **2014**, *5*(1), 152–161.

[29] R. K. Swank, *Phys. Rev.* **1967**, *153*(3), 844–849.

[30] M. J. Shearer, M. Y. Li, L. J. Li, S. Jin, R. J. Hamers, *J. Phys. Chem. C* **2018**, *122*(25), 13564–13571.

[31] B. Caglar, A. C. Kizilkaya, J. W. H. Niemantsverdriet, C. J. K.-J. Weststrate, *Catal. Struct. React.* **2018**, *4*(1), 1–11.

[32] A. Verdaguer, C. Weis, G. Oncins, G. Ketteler, H. Bluhm, M. Salmeron, *Langmuir* **2007**, *23*(19), 9699–9703.

[33] H. Sugimura, Y. Ishida, K. Hayashi, O. Takai, N. Nakagiri, *Appl. Phys. Lett.* **2002**, *80*(8), 1459–1461.

[34] M. Wehrmeister, Master thesis, University of Hamburg, **2022**.

[35] Principles of lock-in detection and the state of the art [white paper], *https://www.zhinst.com/europe/en/resources/principles-of-lock-in-detection*, Zurich Instruments (Date Accessed: 23.06.2025).

[36] QI-Mode, *www.bruker.com/de/products-and-solutions/microscopes/bioafm/library-assets/qi-mode-new-perspectives-in-microbiology.html*, Bruker Corporation (Date Accessed: 23.06.2025.

[37] L. Kelvin, *London, Edinburgh, Dublin Philos. Mag. J. Sci.* **1898**, *46*(278), 82–120.

[38] P. A. Tipler, G. Mosca, *Physik*, 7. ed., Springer Berlin Heidelberg, Berlin, Heidelberg, **2015**, p. 772.

[39] H. B. Michaelson, *J. Appl. Phys.* **1977**, *48*(11), 4729–4733.

[40] S. Hudlet, M. Saint Jean, B. Roulet, J. Berger, C. Guthmann, *J. Appl. Phys.* **1995**, *77*(7), 3308–3314.

[41] A. Axt, I. M. Hermes, V. W. Bergmann, N. Tausendpfund, S. A. L. Weber, *Beilstein J. Nanotechnol.* **2018**, *9*(1), 1809–1819.

[42] H. Roder, *Proc. Inst. Radio Eng.* **1931**, *19*(12), 2145–2176.

[43] J. L. Garrett, J. N. Munday, *Nanotechnology* **2016**, *27*(24).

[44] H. Diesinger, D. Deresmes, J. P. Nys, T. Mélin, *Ultramicroscopy* **2008**, *108*(8), 773–781.

[45] Zurich-Instruments, *MFLI User Manual*, 21. ed., Zurich Instruments AG, Zurich.

[46] C. Reuter, R. Frisenda, D. Lin, T. Ko, D. Perez de Lara, A. Castellanos-Gomez, *Small Methods* **2017**, *1*(7), 3–7.

[47] Y. Gu, J. P. Romankiewicz, J. K. David, J. L. Lensch, L. J. Lauhon, E.-S. Kwak, T. W. Odom, *J. Vac. Sci. Technol. B Microelectron. Nanom. Struct. Process. Meas. Phenom.* **2006**, *24*(4), 2172–2177.

[48] L.-C. Liou, B. Nabet, *Appl. Opt.* **1996**, *35*(1), 15.

[49] Y. Gu, J. P. Romankiewicz, J. K. David, J. L. Lensch, L. J. Lauhon, *Nano Lett.* **2006**, *6*(5), 948–952.

[50] R. Graham, D. Yu, *Mod. Phys. Lett. B* **2013**, *27*(25), 1330018.

[51] D. Fu, J. Zou, K. Wang, R. Zhang, D. Yu, J. Wu, *Nano Lett.* **2011**, *11*(9), 3809–3815.

[52] H. Levinson, *Principles of Lithography*, 3. ed., Spie, Washington, **2010**, p. 1–2, 262.

[53] D. Lengle, Phd thesis, University of Hamburg, **2025**.

[54] D. D. Vaughn, S.-I. In, R. E. Schaak, *ACS Nano* **2011**, *5*(11), 8852–8860.

[55] J. Schulz, L. Schindelhauer, C. Ruhmlieb, M. Wehrmeister, T. Tsangas, A. Mews, *Nano Lett.* **2024**, *24*(43), 13624–13630.

[56] T. Tsangas, C. Ruhmlieb, S. Hentschel, H. Noei, A. Stierle, T. Kipp, A. Mews, *Chem. Mater.* **2022**, *34*(3), 1157–1166.

[57] M. Wehrmeister, D. Lengle, C. Höhmann, A. Mews, T. Kipp, *The Internal Electric Fields of Nanowires with Ohmic Contacts in Operando*, Manuscript in preparation.

[58] J. Puthussery, A. Lan, T. H. Kosel, M. Kuno, *ACS Nano* **2008**, *2*(2), 357–367.

[59] J. K. Utterback, A. N. Grennell, M. B. Wilker, O. M. Pearce, J. D. Eaves, G. Dukovic, *Nat. Chem.* **2016**, *8*(11), 1061–1066.

[60] K. E. Shulenberger, M. R. Jilek, S. J. Sherman, B. T. Hohman, G. Dukovic, *Chem. Rev.* **2023**, *123*(7), 3852–3903.

[61] D. Lide, W. M. Haynes, *CRC Handbook of Chemistry and Physics, Section 12*, 97. ed., CRC Press, Boca Raton, **2016**, p. 123.

[62] X. Bai, H. Wei, T. Qiu, Z. Zhang, Y. He, H. Wang, *J. Phys. Chem. C* **2021**, *125*(40), 22204–22213.

[63] J. Kim, J. Kim, S. Yoon, J.-y. Kang, C.-W. Jeon, W. Jo, *J. Phys. Chem. C* **2018**, *122*(6), 3523–3532.

[64] Z. Cui, X. Wang, Y. Ding, M. Li, *Superlattices Microstruct.* **2018**, *114*, 251–258.

[65] W.-t. Wang, Z.-h. Zheng, F. Li, C. Li, P. Fan, J.-t. Luo, B. Li, *J. Alloys Compd.* **2018**, *763*, 960–965.

[66] A. J. Golabek, Master thesis, University of Waterloo, **2023**.

[67] J. Francis, Phd thesis, Oregon State University, **2013**.

[68] H. Wu, X. Lu, X. Han, X. Zhou, „Tin Sulfide: A New Nontoxic Earth-Abundant Thermoelectric Material“ in *Nov. Thermoelectr. Mater. Device Des. Concepts*, Springer International Publishing, Cham, **2019**, p. 47–61.

[69] Gestis-Stoffdatenbank, *www.gestis.dguv.de*, Institut für Arbeitsschutz der Deutschen Gesetzlichen Unfallversicherung (Date Accessed: 21.07.2025).

[70] Safety Data Sheet, *Tin selenide*, ThermoFisher Scientific, Kandel, **2024**.

A Hazardous Substances

In table A.1 all hazardous substances that were used in this work, are displayed along with notes for their safety and disposal.

Table A.1: Table of used hazardous substances.[69]

Substance	GHS Symbols	Hazards	Precautions	Disposal
Aceton	Danger 	225-319-336	210-223-240-305+351+338-403-235	(3)
AZ 726 MIF Developer	Danger 	290-302+312-314-371-373	260-280-308+311-362+364	(4)
AZ ECI 3012 Photoresist	Danger 	226-318-335	210-261-303+361+353-304+340+312-305+351+338-370+378	(2)
Cadmium selenide	Danger 	301+331-312-350-373-410	201-261-273-301+310+330-308+313-403+233	(1)
Cadmium sulfide	Danger 	302-341-350-361-372-410	201-273-301+312+330-308+313-501	(1)
Copper sulfide	Not a hazardous substance (GHS)			(1)
2-Propanol	Danger 	225-319-336	210-223-240-305+351+338-403-235	(3)
Tin selenide[70]	Danger 	373-410-301+331	264-301+310-304+340-311-403+233-260	(1)
Tin sulfide	Not a hazardous substance (GHS)			(1)
Toluene	Danger 	225-304-315-336-361d-373	210-240-301+310+330-302+352-314-403+233	(3)

Disposal:

(1) Container for inorganic residues.

(2) Solve in organic solvent and dispose in container for halogen free organic solvents.

(3) Dispose in container for halogen free organic solvents.
(4) Dilute with water and dispose in container for other bases.

Table A.2 shows carcinogenic and mutagenic chemicals and chemicals toxic to reproduction used in this work with categories 1A and 1B according to the GHS.

Table A.2: Used CMR chemicals with category 1A and 1B (GHS).

CAS-Number	**Name**	**Procedure and used amount**	**Category (GHS)**
1306-24-7	Cadmium selenide	Microscopy, trace amounts	C:1A
1306-23-6	Cadmium sulfide	Microscopy, trace amounts	C:1B

B Additional Information

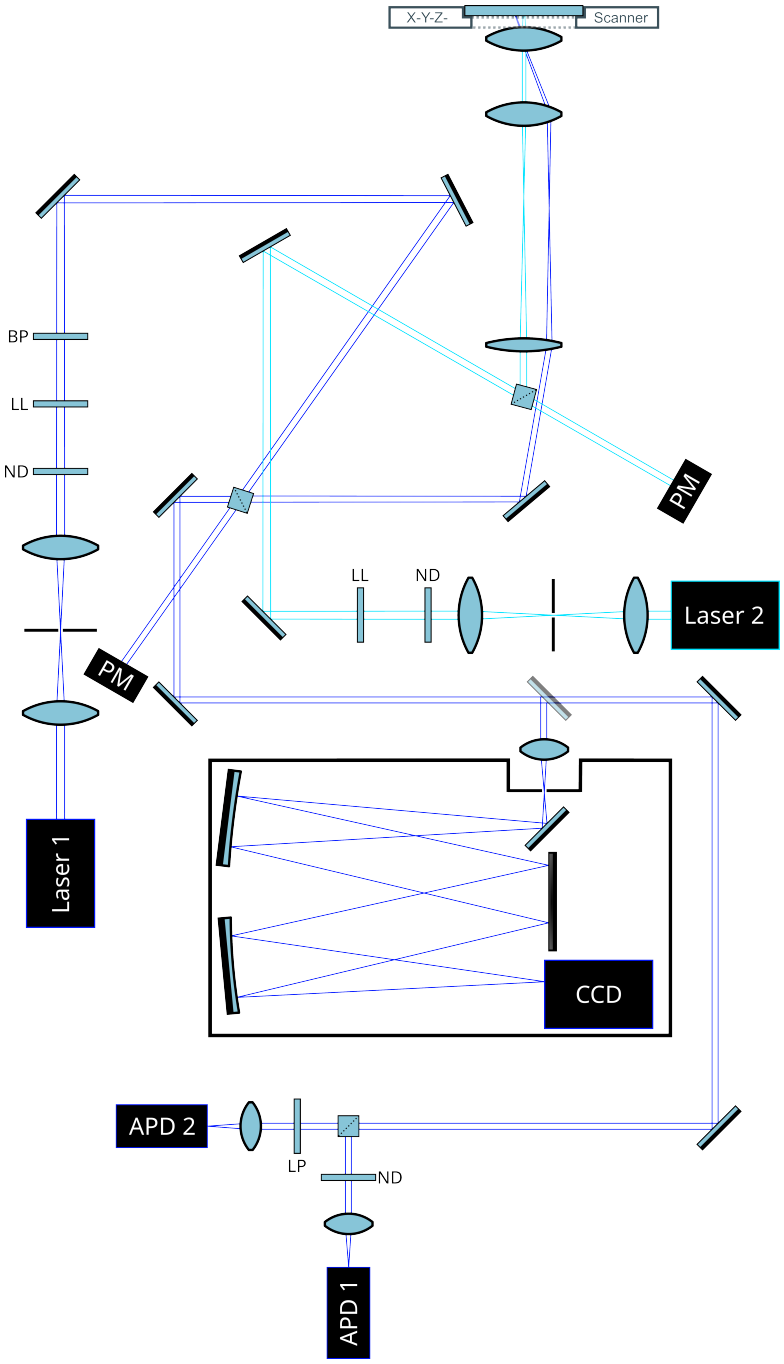

Figure B.1: Sketch of the optical setup as described in section 4.5.

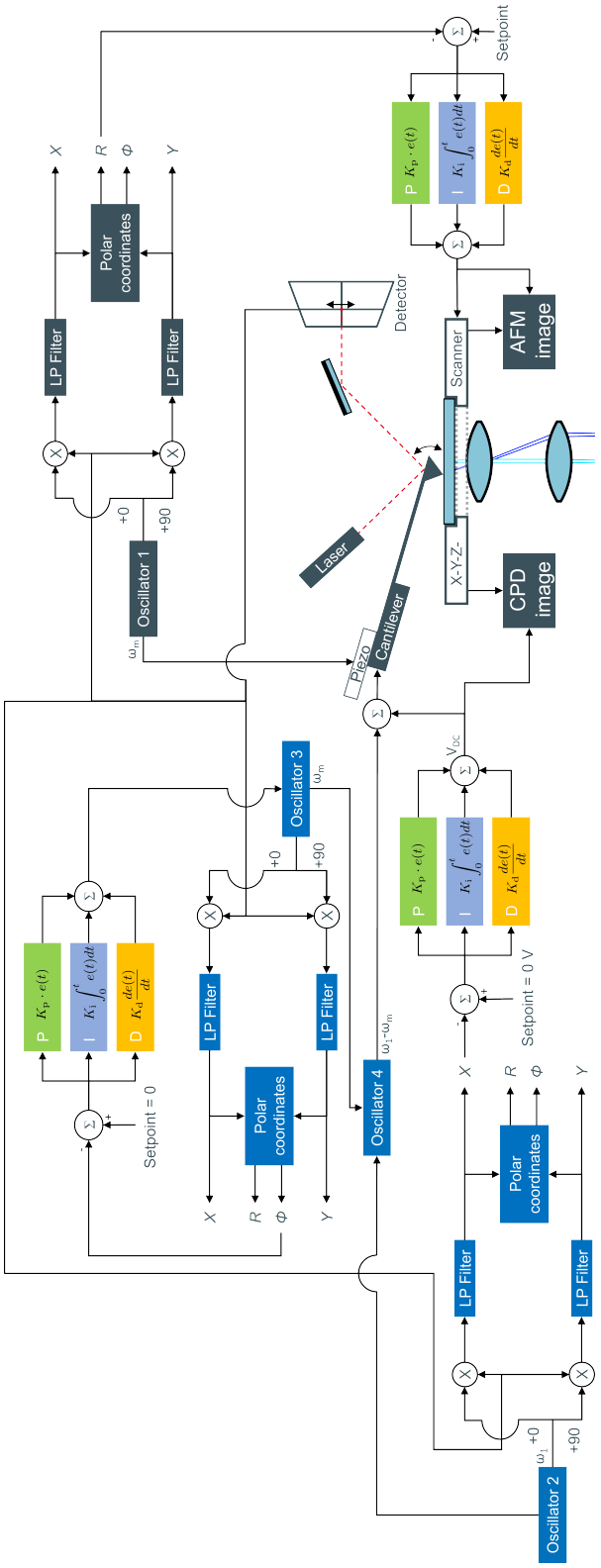

Figure B.2: Detailed sketch of the AFM and KPFM setup described in section 4.6.

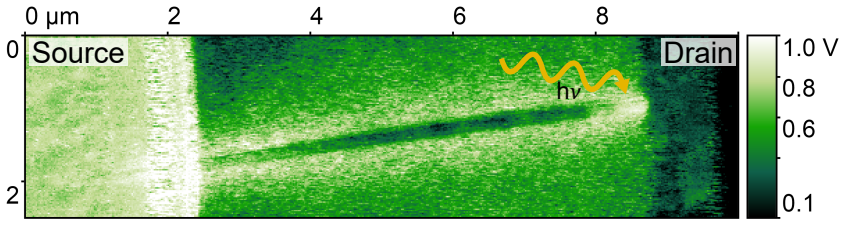

Figure B.3: LI KPFM image of a CdS nanowire diode device, with a Schottky gold source contact on the left with an external bias of +2 V and an ohmic indium drain contact on the right. The yellow arrow indicates the position of the local illumination at the drain contact with a power density 24 W/cm^2.

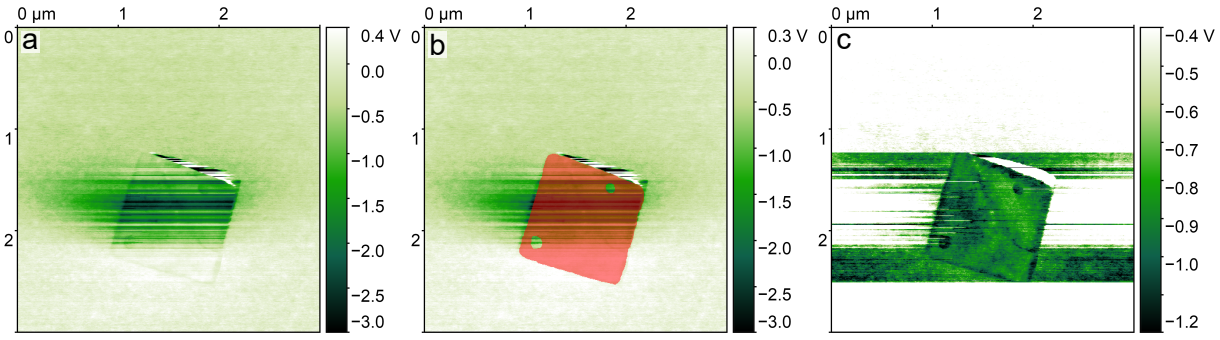

Figure B.4: a) Surface-potential image of a SnSe Nanosheet decorated with AuNPs under illumination before row-alignment. b) The same sheet's surface potential with the applied mask in red. c) The same sheet after row-alignment of the image rows below the mask.

C Publications

Articles

M. Wehrmeister, D. Lengle, C. Höhmann, A. Mews, T. Kipp, The Internal Electric Fields of Nanowires with Ohmic Contacts *in Operando*, Manuscript in Preparation.

R. Kusterer, S. Krohn, **M. Wehrmeister**, C. Strelow, T. Kipp, A. Mews, A closer look at the effects of oxygen on the photoluminescence properties of CdSe/CdS quantum dots, J. Chem. Phys. **2024**, 161.

J. Schulz, L. Schindelhauer, C. Ruhmlieb, **M. Wehrmeister**, T. Tsangas, A. Mews, Controlled Growth of Two-Dimensional SnSe/SnS Core/Crown Heterostructures, Nano Lett. **2024**, 24, 13624–13630.

M. Herber, D. Lengle, S. R. Valandro, **M. Wehrmeister**, E. H. Hill, Bubble Printing of Ti3C2TX MXene for Patterning Conductive and Plasmonic Nanostructures, Nano Lett. **2023**, 23, 6308–6314.

Conference Contributions

11/2024 821. WE-Heraeus-Seminar: Uniting Today's Nanotechnology for Advancing Tomorrow's Semiconductor Physics, Bad Honnef, Germany
Poster: Direct Observation of Charge-Carrier Separation in Contacted Nanowires Under Illumination

02/2024 87. DPG Frühjahrtagung: Sektion Kondensierte Materie (SKM), Berlin, Germany
Talk: Direct Observation of Hole Drift and Diffusion in Contacted CdS Nanowires Under Local Illumination

07/2023 NANAX 10 Nanoscience with Nanocrystals, Vienna, Austria
Poster: Direct Observation of Charge-Carrier Separation in Contacted Nanowires Under Illumination

06/2023 Bunsen-Tagung 2023 – Physical Chemistry of the Energy Transition, Berlin, Germany
Poster: Direct Observation of Charge Carrier Separation in Nanostructures Under Illumination

03/2022 763. WE-Heraeus-Seminar: Optoelectronic Processes at Nanostructured Interfaces, Bad Honnef, Germany
Poster: Kelvin Probe Force Microscopy of Nanostructures

03/2022 Symposium on Quantum Sciences - Osaka University and University of Hamburg, Online
Talk: Kelvin Probe Force Microscopy of Nanostructures

D Acknowledgments

Finally, I would like to thank all those who made this work possible in many different ways. In particular, i want to thank:

- PD Dr. Tobias Kipp for supervising my research and exploring the depths of KPFM with me since the beginning of my master thesis in many discussions, and furthermore for teaching me to have a keen eye on the accuracies of the scientific language.
- Prof. Dr. Alf Mews for giving me the opportunity to begin this project and also supporting my work by providing the necessary equipment and foundations, while also coordinating all the PhD students involved in the production of nanoparticles and samples necessary for this work.
- PD Dr. Tobias Vossmeyer for providing the second assessment of this dissertation.
- Prof. Dr. Carmen Herrmann and Dr. Charlotte Ruhmlieb for being part of the examination committee of my disputation.
- Nicklas Giese for supervising me in my lab course preceding all of this work and introducing me to all the technical aspects of the sample preparation, lithography and contacting of nanostructures, and of course for building the impeccable laser setup.
- The Deutsche Forschungsgemeinschaft for their financial support (project 510528670).
- Dr. Daniel Lengle for the immense work he put into the production of so many samples, reviewing this dissertation and introducing me to the world of fishing together with Carlo Höhmann, and of course the numerous adventurous vacations.
- Carlo Höhmann for being our simulation backbone, giving new insights into the inner workings of semiconductor devices and sparking intense discussions about solid-state physics, and, together with Daniel Lengle, for making the office 247a a most enjoyable place to work.
- Julian Schattschneider and Mareike Dittmar for all the enjoyable post-lunch coffee breaks.
- All of the research group Mews for always making lunch break discussions interesting, work fun and group evenings even more fun.
- My family for supporting me throughout all these years and playing a big role in making me who I am today, and especially my wife Carina for being there for me through all ups and down in my endeavors.

E Eidesstattliche Versicherung

Hiermit versichere ich an Eides statt, die vorliegende Dissertationsschrift selbst verfasst und keine anderen als die angegebenen Quellen und Hilfsmittel benutzt zu haben. Sofern im Zuge der Erstellung der vorliegenden Dissertationsschrift generative Künstliche Intelligenz (gKI) basierte elektronische Hilfsmittel verwendet wurden, versichere ich, dass meine eigene Leistung im Vordergrund stand und dass eine vollständige Dokumentation aller verwendeten Hilfsmittel gemäß der Guten wissenschaftlichen Praxis vorliegt. Ich trage die Verantwortung für eventuell durch die gKI generierte fehlerhafte oder verzerrte Inhalte, fehlerhafte Referenzen, Verstöße gegen das Datenschutz- und Urheberrecht oder Plagiate.

Hamburg den 06.11.2025,